ELECTRON TRANSPORT IN ATOMIC-SCALE DEVICES

RAVI KUMAR TIWARI

NATIONAL UNIVERSITY OF SINGAPORE

2013

ELECTRON TRANSPORT IN ATOMIC-SCALE DEVICES

RAVI KUMAR TIWARI
(*B. Tech., Indian Institute of Technology Kharagpur, India*)

A THESIS SUBMITTED

FOR THE DEGREE OF DOCTOR OF PHILOSOPHY

DEPARTMENT OF CHEMICAL & BIOMOLECULAR ENGINEERING

NATIONAL UNIVERSITY OF SINGAPORE

2013

ACKNOWLEDGEMENTS

First of all I would like to express my deepest gratitude to my supervisor, Dr. Mark Saeys, for giving me the opportunity to work on this exciting project and providing me constant support, timely encouragement, and invaluable guidance throughout my PhD candidature.

Secondly, I would like to thank all my lab mates present and past Hiroyo Kawai, Yeo Yong Kiat, Diana Otalvaro, Xu Jing, Sun Wenjie, Tan Kong Fei, Fan Xuexiang, Chua Yong Ping Gavin, Zhuo Mingkun, Trinh Quang Thang, Cui Luchao, Guo Na for their help and support.

I would also like to thank all my friends Praveen, Prashant, Deepak, Nikhil, Atul, Vishal, Raju, Tarang, Nirmal, Shyam, RP, Krishna, Suresh, Mojtaba, Chakku, to name a few and family members for their continual support and encouragement throughout this exciting journey.

Last but not the least, I would like to thank National University of Singapore for giving me the opportunity to do my PhD here and providing world class infrastructure, faculty members and students all of which has helped me become a better researcher.

TABLE OF CONTENTS

SUMMARY

Advances in nanotechnology have enabled the fabrication of devices in the nanoscale regime. At this scale, material properties are significantly different from the macroscopic scale due to quantum effects. Therefore, in order to design nanoscale devices and understand their properties, it is imperative to utilize the proper simulation toolset which can accurately model these effects. The goal of this thesis is to utilize such simulations to investigate the flow of current through nanoscale structures and develop its understanding from the electronic structure.

In this thesis, current flow in well-defined Scanning Tunnelling Microscope (STM) tunnel junctions are studied first due to its ease of modelling and well-defined structure. Insight obtained from current flow in STM junction is then used to model current flow in industrially important Magnetic Tunnel Junctions (MTJ) that are widely used in Magnetoresistive Random-Access Memory (MRAM). The Elastic Scattering Quantum Chemistry (ESQC) formalism is used for the calculation of the current through the STM tunnel junction, while the non-equilibrium green function (NEGF) method is used to model the MTJ tunnel junction. In both cases, the extended Hückel theory is employed for the description of the system Hamiltonian. To ensure the accuracy of the predicted result, the extended Hückel parameters for each system are fitted to accurate electronic band structures obtained from Density Functional Theory (DFT) calculations. DFT calculations are also used to find the optimized geometry of the studied system.

The theoretical toolsets are first used to study the well-defined but intriguing case of CO adsorbed on a Cu(111) surface [1]. Based on topological considerations, it can be expected that the presence of adsorbed CO between the tip and the surface enhances the current flow between the tip and the Cu(111) surface for a constant tip-surface distance. However, experiments show a decrease in the tunnelling current [2]. We explain this effect by the interaction between the CO and surface states. According to the calculations, CO 5σ states interact strongly with the surface states of Cu(111), and this interaction depletes the density of Cu(111) states near the Fermi level, leading to the decreased current.

Next, a combination of STM image calculation and the thermodynamic stability calculation is used to investigate the surface structure obtained during the experimental thermal stability study of the MoS_2 surface [3], which can be used as a platform for constructing surface dangling bond wires [4]. The calculations show that MoS_2 surface transforms into a S-rich Mo_2S_3 surface above 1300K. The calculations also confirm that the bright spots in the experimental STM image of the reconstructed surface originate from surface S atoms. This behaviour is in sharp contrast to the previous case where the CO molecule appears dark despite being closer to the tip.

Subsequently, the developed theoretical framework is used to study the spin-dependent tunnelling in technologically important Fe|MgO|Fe magnetic tunnel junctions in the presence of biaxial strain [5]. The calculations reproduce both the increase in the conductances and the decrease in the TMR ratio upon the application of biaxial xz-strain. The calculations further show that increase in the parallel conductance upon the application of strain occurs due to a decrease in MgO band gap by 0.3 eV and the barrier thickness by 5%. The anti-parallel conductance, however, is significantly more sensitive to strain because of the change in the

location of Fe(100) minority states at the Fermi level, which move closer to the centre of the Brillouin zone where transmission through the MgO barrier is higher. As a result, the conductance for both the minority channel and anti-parallel configuration increases faster than for the majority electrons, leading to the decrease in the TMR ratio.

Finally, the band gap variation in thin MgO films observed during barrier thickness-dependent TMR studies of Fe|MgO|Fe tunnel junctions is investigated in more detail. DFT calculations reveal that the Mg(001) band gap decreases with thickness below 5 ML, consistent with experimental observations [6]. The decrease in band gap with decreasing film thickness arises from a decrease in the Madelung potential. This is compensated by a decrease in the charge transfer from the Mg to O ions, which slightly increases the band gap. A simple electrostatic model, which accounts for both charge transfer and changes in the local Madelung potential, is able to reproduce the trend observed in the DFT calculation.

In summary, tunnelling current at atomic scales for various scientifically and technologically important systems such as STM and MTJ is studied within a theoretical framework in this thesis. The ability to correctly predict and explain experimental observations makes them a very valuable toolset to study tunnelling current at atomic scales, which is required to design next-generation atomic scale electronic devices.

References

[1] R. K. Tiwari, D. M. Otálvaro, C. Joachim, and M. Saeys, *Surf. Sci.* **603**, 3286 (2009).

[2] L. Bartels, G. Meyer, and K.-H. Rieder, *Appl. Phys. Lett.* **71**, 213 (1997).

[3] R. K. Tiwari, J. Yang, M. Saeys, and C. Joachim, *Surf. Sci.* **602**, 2628 (2008).

[4] K. Yong, D. Otalvaro, I. Duchemin, M. Saeys, and C. Joachim, *Phys. Rev. B* **77**, 205429 (2008).

[5] A. M. Sahadevan, R. K. Tiwari, G. Kalon, C. S. Bhatia, M. Saeys, and H. Yang, *Appl. Phys. Lett.* **101**, 042407 (2012).

[6] M. Klaua, D. Ullmann, J. Barthel, W. Wulfhekel, J. Kirschner, R. Urban, T. Monchesky, A. Enders, J. Cochran, and B. Heinrich, *Phys. Rev. B* **64**, 134411 (2001).

SYMBOLS AND ABBREVIATIONS

Symbols

A	Spectral function
α	Decay constant
C_M	Madelung constant
χ	Polarizability
e	Value of electronic charge
ϵ	Dielectric function
ϵ_{xc}	Exchange-correlation energy per electron
E_f	Fermi energy
E_{xc}	Exchange-correlation energy
f_0	Fermi function
G_0	Green function of non-interacting particles
G	Green function of interacting particles
$\hbar$	Reduced Planck's constant
H	Hamiltonian matrix
$\widehat{H}$	Hamiltonian operator
I	Current
k	Momentum vector
μ	Chemical potential
m	Mass
ν	Poissons ratio
n	Band index
P	Propagator matrix

p_{s_2}	Partial pressure of S_2
ψ	Wave function
Q	Charge
ρ	Electron density
R_{ij}	Reflection probability
$\vec{\boldsymbol{r}}$	Position vector
Σ	Self energy
s_n	Atomic orbitals
S	Overlap matrix
τ	Interaction matrix
T_{ij}	Transmission probability of an electron from channel i to channel j
T	Kinetic energy
$V(x)$	Barrier potential
V_{xc}	exchange-correlation potential
V_H	Hartree energy electron electron interaction
V_0	Barrier height
W	Screened Coulomb potential
$Y_l^m(\theta, \varphi)$	Spherical harmonics
ζ	Orbital exponent

Abbreviations

AP	Anti-parallel
ARPES	Angle resolved photo electron spectroscopy
BE	Binding energy
CPP	Current perpendicular-to-plane

DFT	Density functional theory
DLC	Diamond like carbon
DOS	Density of states
EHMO	Extended Hückel molecular orbital
EHT	Extended Hückel theory
ESQC	Elastic scattering quantum chemistry
FCVA	Filtered cathodic vacuum arc
FM	Ferro-magnetic
GMR	Giant magneto-resistance
GGA	Generalized Gradient Approximation
HFA	Hartree-Fock approximation
LCAO	Linear combination of atomic orbitals
LDA	Local density approximation
LDOS	Local density of states
LMC	Local mechanical stress control
MRAM	Magnetoresistive random-access-memory
NEGF	Non-equilibrium Green’s function
PAW	Projector-augmented-wave
PBE	Perdew–Burke–Enzerhoff
QP	Quasi-particle
RPA	Random phase approximation
SEM	Scanning electron microscope
STS	Scanning tunnelling spectroscopy
STT-RAM	spin transfer torque based random access memory
TEM	Transmission electron microscope
TRIM	Transport of ions in matter

UHV	Ultra high vacuum
VASP	Vienna ab initio simulation package
VOIP	Valence orbital ionization potentials
WKB	Wenzel-Kramer-Brillouin
XPS	X-ray photoelectron spectroscopy
XRD	X-ray diffraction

LIST OF TABLES

LIST OF FIGURES

PUBLICATIONS

- **Ravi K. Tiwari**, Jianshu Yang, Mark Saeys and Christian Joachim, "Surface reconstruction of MoS_2 to Mo_2S_3", *Surface Science* 602, 2628 (2008)

- **Ravi K. Tiwari**, Diana M. Otalvaro, Christian Joachim and Mark Saeys, "Origin of the contrast inversion in the STM image of CO on Cu(111)", *Surface Science* 603, 3286 (2009)

- Ajeesh M. Sahadevan, **Ravi K. Tiwari**, Kalon Gopinadhan, Charanjit S. Bhatia, Mark Saeys, and Hyunsoo Yang, "Biaxial strain effect of spin dependent tunneling in MgO magnetic tunnel junctions", *Applied Physics Letters* **101**, 042407 (2012)

- **Ravi K. Tiwari**, and Mark Saeys, "On the origin of the decreased band gap in ultrathin MgO films ", Ready for submission.

TALKS

- Strain Effect in Mgo Based Magnetic Tunnel Junctions, *ICYRAM , Singapore,* July 1-6 (2012) (**Best poster award**)

- A Theoretical and Experimental STM Study of the Surface Reconstruction of MoS_2 to Mo_2S_3 *SingSPM, Singapore*, May 8-9 (2008) (**Invited speaker**)

- A theoretical study of atomic wires and atomic junctions created on a Molybdenum disulfide surface", *AIChE annual general meeting, Philadelphia,* USA, Nov 16-21 (2008)

- Single dopant transistor, *VIP atom technology seminar (Phase II) open seminar, Singapore*, Sep 2008

CHAPTER 1

Introduction

1.1 Nanotechnology and its scope

Nanotechnology has enabled the deliberate and controlled manipulation, measurement, modeling, and production at nanoscale, resulting in materials and devices with fundamentally new properties and functions [1]. As the name suggests, the nanoscale typically indicates length scales of a few nanometers where materials can no longer be considered to be continuous, rather it has to considered as composed of individual atoms. As a result, various properties exhibited by nano-materials are size-dependent and they differ considerably from their bulk counterpart. Two factors are responsible for the appearance of new properties: first, at this scale, quantum phenomena starts to appear and second, the surface properties start to play an increasingly bigger role as the size of the system reduces. These novel properties exhibited by nanomaterials are finding wider application in a variety of systems. For example, electrical transport properties are increasingly being utilized in microelectronics, communication industries as well as data storage devices, and have led to smaller device sizes with improved functionality at reduced cost [2].

As the properties exhibited at the nanoscale are not directly related to bulk properties, it becomes very vital to utilize the proper theoretical tool sets to understand them. This thesis mainly deals with the calculation of current flow at the nanoscale and explains the observed behaviour from the knowledge of the electronic structure.

In this thesis two different systems have been chosen to study tunnelling current. First, the theoretical tools are employed to study current flow in a well-defined system as represented by the scanning tunnelling microscope (STM). The developed theoretical framework is then employed to study current flow in industrially important multilayers such as magnetic tunnel junctions (MTJ).

1.2 Key driver of nanotechnology: Scanning tunnelling microscope

One of the key drivers of nanotechnology is the scanning tunnelling microscope (STM). STM not only makes it possible to observe atoms and molecules but also to manipulate them in a precise and controlled way. STM consists of an atomically sharp tip whose movement is controlled by piezoelectric controllers, Figure 1.1(a). Application of a bias voltage results in a tunnelling current between the tip and the surface. In order to image a surface, the tip is scanned over the surface while maintaining a constant distance between the tip and the surface. The tunnelling current decays exponentially with distance for a given tip and a surface. As a result, a slight variation in the surface structure leads to a large change in the tunnelling current. As the tip scans over the surface, the tunnelling current is recorded. The image of the surface is then derived by plotting the variation of the tunnelling current as a function of the tip location. As is clear from the above discussion, the STM image is a plot of the surface of constant current. The exact value of the tunnelling current depends on the interaction between the tip and the surface electronic states. As a result, in many cases, the STM images are not the actual topographical feature of the surface. Hence, it requires a complete understanding of the electronic interaction between the tip and the surface to correctly interpret STM images.

The STM is also used to manipulate individual atoms and molecules on a surface in a controlled way. In order to manipulate atoms, the tip is brought sufficiently close to the adsorbed atom or molecule. At close distance, a weak bond is formed between the tip and the adsorbed atom. The atom is then positioned at the desired location by moving the tip. Manipulation of atoms and molecules has resulted in many interesting quantum structures showing novel phenomena. For example, the quantum corrals made by confining surface state electrons by individually positioning iron adatoms over Cu(111) surface show a standing electron wave pattern [3] .

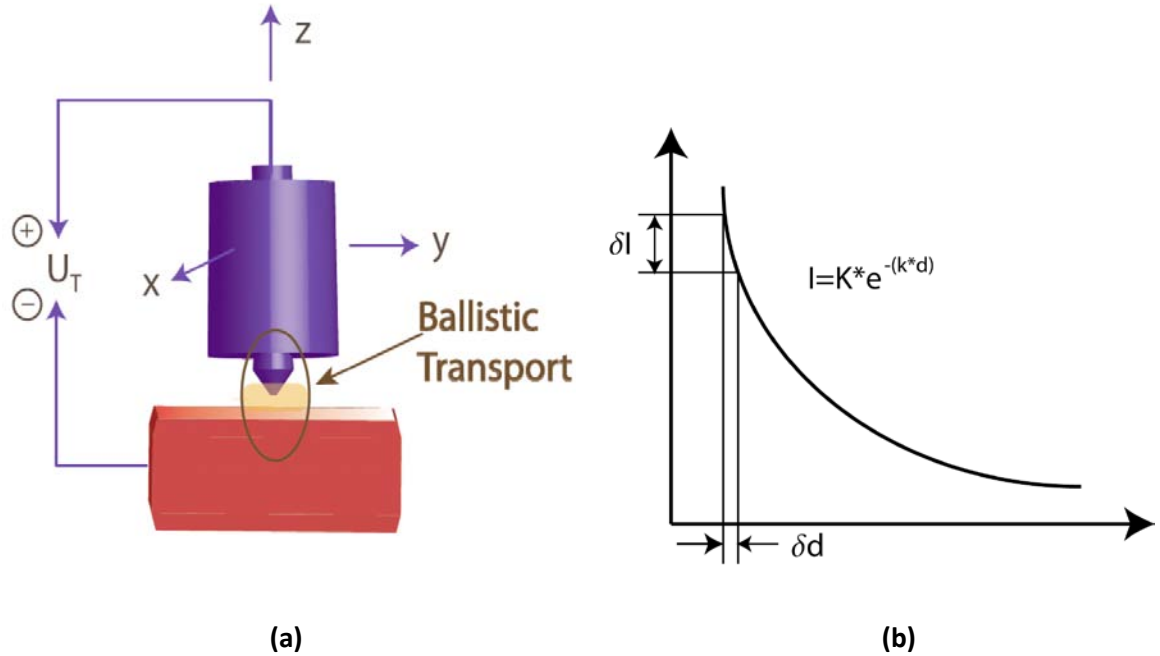

Figure 1.1: (a) Schematic diagram of a typical STM set-up. To form the image of the surface, the tip is scanned over the surface while maintaining constant value of the current. (b) The variation of the tunnelling current I with the tip surface distance d. The tunnelling current decays exponentially when the tip surface distance is increased.

1.3 Large-scale application of tunnelling current: Magnetic Tunnel Junction

Bulk tunnelling currents also finds important application in an industrially important device, the magnetic tunnel junction (MTJ). A MTJ consists of a thin insulating spacer layer

sandwiched between two ferromagnetic electrodes, Figure 1.2. The application of a bias voltage across the barrier leads to a finite tunnelling current through the junction. When the thickness of the insulating space is smaller than the spin relaxation length of the electrons, then the spin of the electrons is conserved during the transport process. This makes it possible to control the current flow by changing the relative magnetization direction of the ferromagnetic electrodes.

The performance of a MTJ is measured by a quantity called the tunnelling magneto-resistance (TMR) ratio, which is defined as

$$TMR = \frac{\left(I_{parallel} - I_{anti-parallel}\right)}{I_{anti-parallel}} \qquad 1.1$$

where $I_{parallel}$ and $I_{anti-parallel}$ are the current for parallel and anti-parallel configuration of electrode magnetization. Generally, the current flow in a MTJ is maximum (minimum) when the magnetization directions of the two electrodes are parallel (anti-parallel), though negative TMR ratios have also been reported [4].

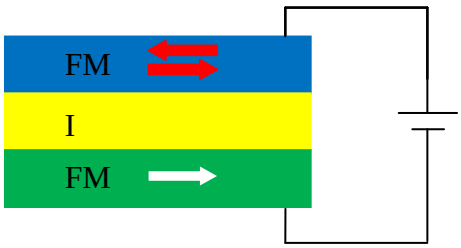

Figure 1.2: Schematic diagram of a magnetic tunnel junction. A thin insulating layer (I) is sandwiched between two ferromagnetic electrodes (FM). In this diagram the magnetization of the bottom electrode is fixed, while the magnetization of the top electrode is free to rotate under the influence of an external magnetic field.

The origin of the tunnelling magnetoresistance can be understood by noting that typically there are two types of electrons in a magnetic material: majority (spin-up) and minority (spin-down). At a given energy the current due to an electron with a particular spin direction is

proportional to its number at that energy which can be deduced from the density of states (DOS). The DOS, n(E), represents the number of states which have energy in the range (E, E+dE). In a ferromagnetic material, the DOS of majority and minority spins are shifted in energy relative to each other to minimize the Coulomb repulsion under the Pauli Exclusion Principle.

In the two current model, it is assumed that the electrons with different spins do not interact with each other [5-6]. As a result, we can find the total current by summing up the contribution due to each spin. Figure 1.3 depicts the current flow mechanism under parallel and anti-parallel magnetization. The left hand side of the figure show the magnetization orientation of the electrodes under parallel (top) and anti-parallel (bottom) magnetization while the right hand side show corresponding density of states (DOS). For the typical length scale encountered in a MTJ the spin of the electrons are conserved throughout the transport process. This means that when the magnetization is parallel, the up (down) spin electrons go to the empty up (down) spin states of the other electrode, while for the anti-parallel magnetization, the up (down) spin electrons go to the empty down (up) spin of the other electrode.

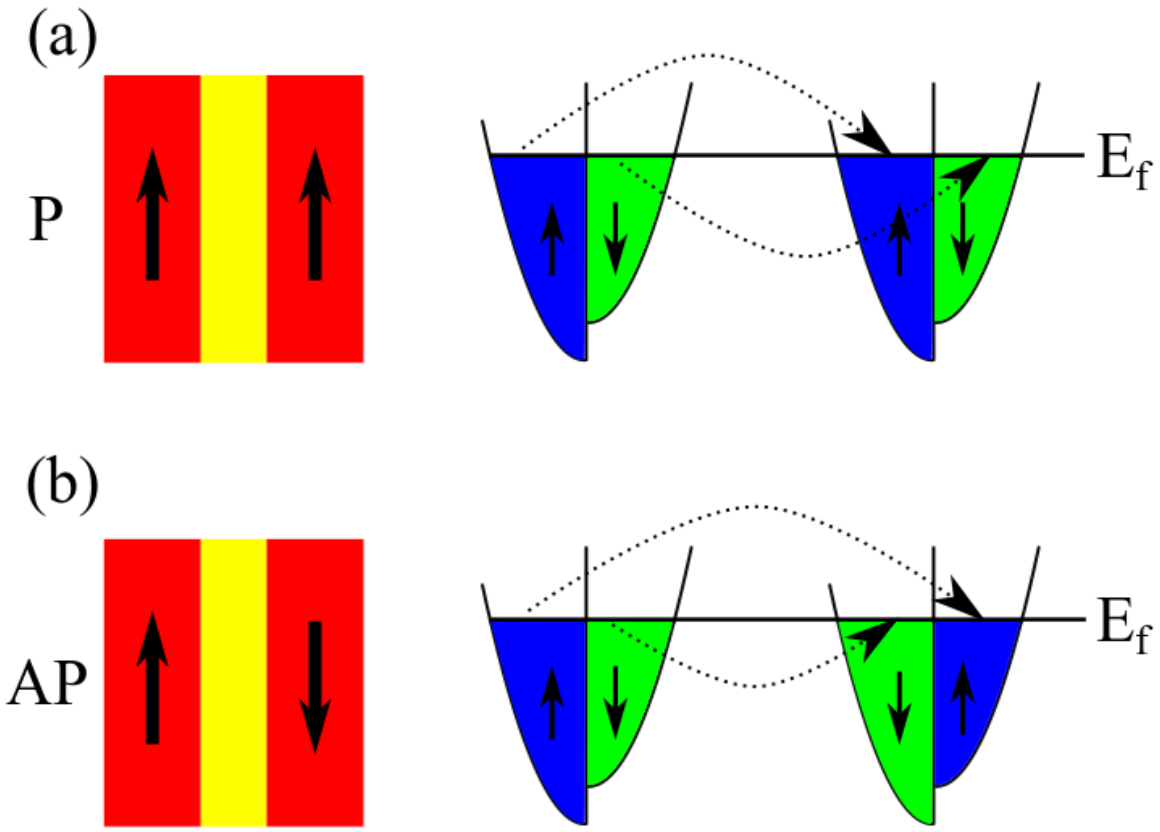

Figure 1.3: Schematic diagram of a) orientation of the magnetization for the parallel configuration and the corresponding DOS for the left and the right electrode b) orientation of the magnetization for the anti-parallel configuration and the corresponding DOS for the left and the right electrode. The dotted arrows on the figure on the right show the origin of electrons of a given state and the state they are accepted into after traversing the barrier.

The extreme sensitivity of the MTJ current to the magnetic field, because of high magneto-resistance ratio, has resulted in their application in a new generation of read-out head [7]. With the increased information density of the hard-disks, the magnetic area that stores the information in the form of differently magnetized areas also shrinks. As a result, the magnetic field of each byte becomes weaker and harder to read therefore a higher sensitivity is required. Additionally, the application of MTJs in MRAMs makes it possible to both read and write information resulting in the creation of a fast and easily accessible computer memory. As a result, these universal memories are expected to replace the traditional RAM and the hard disk.

1.4 Ballistic conductance

In a STM as well as in a MTJ, the typical length scale an electron traverses between its injection and detection is of the order of a few nanometres. Classical transport theory, which deals with macroscopic materials whose dimensions are much larger than the mean free path of electrons, is inadequate to describe transport properties at this scale. In macroscopic materials, electrons experience a large number of inelastic scattering events during the transport. This regime is generally referred to as the diffusive regime [8]. In this regime, due to the large number of scattering events, electronic waves are randomized and only their amplitude determines the magnitude of the current. Since the amplitude of the electronic wave function is related to the number of electrons, transport in the diffusive region is determined solely by the number of electrons and their scattering events.

When the dimension of the material becomes comparable to the mean free path of electrons, electrons do not experience inelastic scattering. Transport in this regime is termed ballistic transport [8]. In this regime, it is essential that the wave nature of the electrons is taken into account for the correct treatment of its transport properties. The Landauer-Büttiker formalism, which is usually employed for ballistic transport, does that by treating electron transport as a scattering event at the interfaces. The current is then calculated from the knowledge of the transmission probability across the interfaces. The transmission probability appearing in the Landauer-Büttiker method is generally calculated from the transfer matrix method [9] or the green function method [10].

Figure 1.4 illustrates the scheme that is used to calculate the ballistic tunnelling current in a STM. For the modelling purpose, the STM is divided into two parts: a periodic part which consists of the left and the right electrodes, and a defect part which consists of the surface, the interface, the adsorbed molecule, the vacuum and the tip. The electrons propagate in the periodic part without scattering. When the electrons encounter the defect, a part is reflected while the other are transmitted across the defect. The transmission probability is defined as the ratio of the square of the amplitude of the transmitted wave (C) to the square of the amplitude of the incoming wave (A).

$$T(E) = C^2/A^2 \qquad 1.2$$

The model to describe current flow in a MTJ is very similar to the STM model. In this case, too, the left and the right electrodes are represented by semi-infinite periodic parts. The only difference is that now the defect part is insulating barrier material instead of the tip and the adsorbed molecule separated by the vacuum as in the case of the STM.

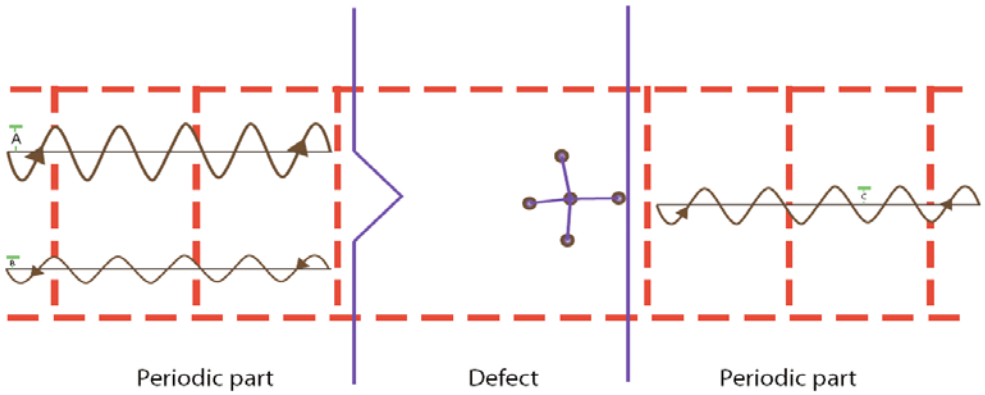

Figure 1.4: Schematic diagram of an electronic wave scattered by a defect. At the interface, a part of the incoming wave with amplitude A is reflected with amplitude B while the rest is transmitted with amplitude C.

1.5 Key challenges addressed in this thesis

As discussed in the previous sections, all the theoretical tools to study quantum transport at the nano-scale are quite well established. However, what Paul Dirac said years ago, "The fundamental laws necessary for the mathematical treatment of a large part of physics and the whole of chemistry are thus completely known, and the difficulty lies only in the fact that application of these laws leads to equations that are too complex to be solved", remains true even in the age of supercomputers. Over the years, various realistic assumptions and approximations have been proposed which have been implemented in various computer codes that solve these equations numerically. Still, modeling the sheer complexity of the experimental set up and solving it exactly remains out of reach of even the most advanced supercomputers. Thus, to understand experimental observations, it becomes necessary that we build a simplified model that is able to capture all the essential physics, choose an appropriate level of theory and choose the parameters that are able to describe the experimental condition faithfully. Finally, the ultimate utility of the simulations lies not in reproducing the experimental results but to provide insight into factors responsible for the observed experimental behaviour and based on that insight propose experimental conditions that will lead to improved performance.

Above are the key general challenges that the conducted work addresses. To address the challenges, first a thorough knowledge of key theories, their applicability and their limitations was developed. Also a deeper knowledge of the experiments was acquired with consultation with the experimentalists that was the key to modelling the experimental system.

1.6 Specific challenges addressed in this thesis

The specific challenge was to first acquire proficiency in the simulation tools and techniques applicable for the current flow at the nano-scale and then application of those tools to provide unique insights into experimental observations.

The modeling of current flow at the nano-scale becomes complex mainly due to two reasons 1) the wave nature of electrons comes into play therefore full quantum mechanical treatment is needed to model their behaviour 2) At such a small scale every atom matters and the detailed knowledge of their position becomes crucial to properly model the system. As most of the time information, about the system geometry is inaccessible experimentally, state-of-the-art ab-initio calculations are required to arrive at optimized system geometries.

The modeling approach was used to tackle two major systems: 1) STM and 2) MTJ. A STM provides one of the most powerful yet a very simple set-up to observe current flow through molecules, and surfaces that makes it an ideal system to benchmark theoretical predictions. From experiments alone, however, it is not always easy to interpret the observed image even in a simple STM set-up. For example, questions like what atoms appear bright? Is the dark spot really a hollow site or some adsorbed atom or molecule? Does the experimental observation represent topology or the electronic structure of the system? In the first part of the thesis, the challenge was to benchmark the calculations against the experimental observation and also to provide deeper insight into the mechanism leading to the experimental observation. The developed insights like role of the electronic structure,

adsorption geometry, interfaces would prove very valuable in formulating design rules for the nano-devices.

Next, the acquired expertise was utilized to gain insight into more complex system that has tremendous industrial application, a MTJ. The highly desirable quality of high TMR ratio of a MTJ is somewhat offset by its high resistance. To overcome this limitation, our collaborators applied strain to the device which, indeed, resulted in the lowering of its resistance but at the expense of the lowered TMR ratio. In this case, the challenge was to find from the theoretical consideration reason behind the observed effect.

1.7 Intellectual contribution of this thesis

The intellectual contribution of this thesis lies in the use of theoretical calculations to provide deeper insights into a diverse range of experimental observations for which no intuitive explanations were available. In fact, in this study we chose mostly counter-intuitive and/or hard-to-interpret experimental observations to test the limits of the theoretical modeling. Below we provide a brief discussion of the systems that we studied, the insights and the wider implication of the studies.

1.7.1 Interpretation of reduced current flow upon CO adsorption on Cu(111) in STM tunnel junction

Based on topological considerations, it would be expected that the presence of a CO molecule in the STM tunnel junction would enhance the current flow between the tip and the surface. This is indeed the case for CO adsorbed on Pt(111) [11].

Surprisingly, CO adsorbed on Cu(111) reduces the tunnelling current for a range of bias voltages [12]. Intrigued by this counter-intuitive observation, we simulated this system using an accurate description of the Cu(111) electronic structure, and its interaction with adsorbed CO and the tip. Our simulations show that it is the destruction of the surface state by its interaction with CO molecular orbitals that is responsible for the reduced current.

1.7.2 Elucidation of the unknown surface structure obtained during thermal annealing of MoS_2

Recently, MoS_2 has received a lot of attention as promising substrate for creating various nano-scale devices. In fact, individual S atoms have been extracted from MoS_2 surface by the application of pulse voltage [13]. Additionally, Yang et al. [14] showed theoretically that a line of S vacancies on MoS_2 acts as a conducting channel. In one of the earliest attempts, our collaborators used thermal treatment to fabricate nano-wires on MoS_2 surface by creating S vacancies. Unfortunately, the thermal treatment led to a major reconstruction of the MoS_2 surface.

From the Mo-S phase diagram, we determined that the experimental conditions led to the reconstruction of MoS_2 to Mo_2S_3. Furthermore, the free energy calculation for a range of possible Mo_2S_3 surface chemical compositions showed that S-rich surface has the highest stability under the STM conditions. STM image calculations for the S-rich Mo_2S_3 surface showed a good agreement with the experimental image of the reconstructed surface, confirming that the observed structure is indeed the S-rich Mo_2S_3 surface. Incidentally, in this case S atoms which are closer to the tip appear bright while Mo atoms appear dark despite contributing most of the states at the Fermi level. In contrast to the previous study, topology becomes the deciding factor in this case.

1.7.3 Observation of a reduced TMR ratio but a higher current in a biaxially strained MTJ

The higher TMR ratio of a MTJ consisting of Fe|MgO|Fe is somewhat offset by its higher resistance. Our collaborators, therefore, used strain engineering to decrease the resistance of Fe|MgO|Fe tunnel junction. True to their expectations, the resistance decreased but the strain also decreased the TMR ratio.

To understand the factors leading to this behaviour, we modeled this system using the non-equilibrium Green's function (NEGF) formalism coupled with extended Huckel theory (EHT). Our simulations show that the conductance increases due to the reduction in the MgO barrier thickness as well as barrier height. However, the relative increase in conductance for minority channels is much more pronounced because minority states move towards the centre of the Brillouin zone where the conductance inside MgO barrier is higher.

1.7.4 Observation of anomalous increase in the band gap with thickness in thin MgO

During our previous study, we observed a counter-intuitive phenomenon of an increase of MgO bandgap with thickness for very thin MgO films. Since the bandgap is one of the dominant factors deciding the performance of a MTJ, we investigated this phenomenon in detail.

We employed state-of-the-art HSE03+G_0W_0 calculations that accurately predict the MgO bandgap. Our calculations show that the band gap increases from 4.52 eV to 5.69 eV when the thickness of the MgO films is increased from 1 ML to 5 ML. The increase in the band gap arises from changes in the charge transfer from Mg to O ions, and more importantly, from changes in the Madelung potential at the site of ions when the thickness of the film increases. These two factors oppositely affect the band gap. However, the effect of the Madelung potential dominates and leads to an increase in the bandgap with thickness.

1.7.5 Wider implications

The insight obtained from the study of CO on Cu(111) and of the thickness-dependent MgO bandgap could have wider implication in the design of nano-scale devices. During the creation of nano-scale devices many unwanted states, i.e., surface states, edge states, might appear or their properties might change. These might influence the IV characteristics of devices in unforeseen ways. Additionally, the different components of the device might interact in unexpected ways leading to further complications in the device IV characteristics. Thus the role of the simulation becomes very important to understand and design the nano-scale devices.

The study of the MoS_2 phase transformation and of strained MTJs show the importance of theoretical modeling in providing understanding of the experimental observation at the nano-scale.

References

[1] C. P. Poole and F. J. Owens, *Introduction to Nanotechnology* (Wiley-IEEE, 2003), p. 388.

[2] P. S. Peercy, *Nature* **406**, 1023 (2000).

[3] M. F. Crommie, C. P. Lutz, and D. M. Eigler, *Science* **262**, 218 (1993).

[4] H. Yang, S.-H. Yang, D.-C. Qi, A. Rusydi, H. Kawai, M. Saeys, T. Leo, D. Smith, and S. Parkin, *Phys. Rev. Lett.* **106**, 167201 (2011).

[5] N. F. Mott, *Adv. Phys.* **13**, 325 (1964).

[6] J.P. Velev, P.A. Dowben, E.Y. Tsymbal, S.J. Jenkins, and A.N. Caruso, *Surf. Sci. Rep.* **63**, 400 (2008).

[7] A. Chung, J. Deen, J.-S. Lee, and M. Meyyappan, *Nanotechnol.* **21**, 412001 (2010).

[8] T. Heinzel, *Mesoscopic Electronics in Solid State Nanostructures* (Wiley-VCH, 2007), p. 395.

[9] P. Sautet and C. Joachim, *Phys. Rev. B* **38**, 12238 (1988).

[10] J. Cerdá, M. A. Van Hove, P. Sautet, and M. Salmeron, *Phys. Rev. B* **56**, 15885 (1997).

[11] J. A. Stroscio and D. M. Eigler, *Science* **254**, 1319 (1991).

[12] L. Bartels, G. Meyer, and K.-H. Rieder, *Appl. Phys. Lett.* **71**, 213 (1997).

[13] T. Shintani S. Hosaka, S. Hosoki, T. Hasegawa, H. Koyanagi and M. Miyamoto, *J. Vac. Sci. Technol. B* **13**, 2813 (1995).

[14] K. Yong, D. Otalvaro, I. Duchemin, M. Saeys, and C. Joachim, *Phys. Rev. B* **77**, 205429 (2008).

CHAPTER 2

Modeling ballistic electron transport

2.1 Introduction

The development of Landauer formula, which links electron transmission probability to current flow, is one of the most important theoretical achievements in the field of quantum transport. By relating the current to the transmission probability, the Landauer formula provides a conceptual framework to study ballistic conductance in atom scale structures that greatly simplifies computations [1]. As a result, the Landauer formula is increasingly being applied to study current flow in a variety of atom scale devices. For example, current flow in Scanning Tunnelling Microscope (STM), Magnetic Tunnel Junction (MTJ) as well as Giant Magneto-Resistance (GMR) devices have been studied with the Landauer formula [2–5].

In this chapter the methodologies used for the calculations in the thesis are described in detail. First, the motion of a quantum particle in the presence of a square barrier is described to illustrate the tunnelling behaviour and the concept of transmission probability. Thereafter, the Landauer formula for current calculations is described in detail. Subsequently, the transfer matrix technique [6] and the green function [2] is described which are used to calculate the transmission probability for realistic systems. Next, the extended Hückel method which is used in the construction of the Hamiltonian matrix is illustrated. The extended Hückel parameters for the description of the constituent's atoms are calculated by fitting it to accurate bandstructure obtained from ab-initio DFT calculation. After that a brief description of DFT and various approximations used in its solution is provided. To avoid the

underestimation of bandgap associated with DFT calculations [7], many body perturbative GW theory is used for the bandgap calculation of semi-conductors and insulators. In the final section a brief description of the GW theory is given.

2.2 Quantum Mechanical Tunnelling

In classical mechanics, a particle can cross a potential barrier only when its total energy is greater than the height of the potential barrier. However, quantum particles have finite probability of crossing a potential barrier even when their total energy is less than the height of the potential barrier. This phenomenon of particles overcoming a classically insurmountable barrier is referred to as quantum mechanical tunnelling. The tunnelling behaviour of electrons leads to the tunnelling current which forms the basis of operation for various atom scale devices like STM and MTJ. In STM, the image of a surface is formed from the tunnelling current between the STM tip and the surface when the tip is scanned over the surface. In a TMR device, the change in tunnelling current when the relative magnetization of electrodes is reversed forms the basis of its operation.

Because of its technological importance, various methods have been proposed to calculate tunnelling probability. The transfer matrix technique [7] and the green function technique [2] are two widely used methods which have been employed to study tunnelling in various systems. In this thesis, the transfer matrix technique is employed for STM image calculations for CO/Cu(111) and for Mo_2S_3 surface, while the green function is employed for the calculation of tunnelling current in MTJ.

2.3 Tunnelling probability through a square barrier

In this section the analytical solution of a quantum mechanical particle, when it encounters a rectangular potential barrier is obtained by solving the Schrodinger equation of the system. The particle wave with unity amplitude encounters the potential barrier of height V_0 and width a at $x = 0$ as shown in Figure 2.1. As a result, a part of the incoming wave is reflected with amplitude r, while the rest is transmitted with amplitude t. The transmission probability for the particle, the ratio of the square of the amplitude of the transmitted wave to the incident wave, is calculated by solving the Schrodinger equation of the system

$$\left[-\frac{\hbar}{2m}\frac{d^2}{dx^2} + V(x)\right]\Psi(x) = E\Psi(x) \qquad 2.1$$

Where $\hbar$ is reduced Planck's constant, m is mass, E is energy of the particle and $V(x)$ is the barrier potential which is V_0 for $0 \leq x \leq a$ and 0 for all other values of x. Since the potential within a given region remains constant, the wave function in each region is expressed as free particle wave

$$\begin{aligned} \psi_L(x) &= e^{ik_0 x} + re^{-ik_0 x}, x < 0 \\ \psi_c(x) &= B_r e^{ik_1 x} + B_l e^{-k_1 x}, 0 < x < a, \\ \psi_R(x) &= te^{ik_0 x}, x > a \end{aligned} \qquad 2.2$$

Where B_l and B_r represent the transmitted and the reflected amplitude at the left barrier. The transmission probability, when the energy is less than the barrier height, $E < V_0$ is given by

$$T = |t|^2 = \frac{1}{1 + \frac{V_0^2 Sinh^2(k_1 a)}{4E(V_0 - E)}} \qquad 2.4$$

Thus it is clear from the above expression that there is a finite transmission probability when the particle energy is less than the height of the potential barrier. The transmission probability for both the quantum mechanical and the classical particles are plotted in Figure 2.2. For classical particles the probability is zero (one) when the barrier height is more (less) than the particle energy. However, in the quantum case there is a finite probability for the particle transmission, even when the particle energy is less than the barrier height. Interestingly when the particle energy is more than the barrier height the transmission probability becomes 1 only for certain particle energies called the resonance energies.

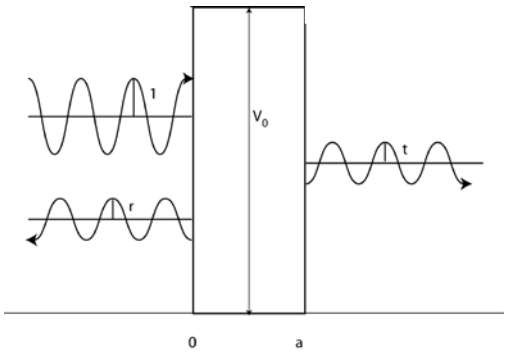

Figure 2.1 : A particle wave of unit amplitude encounters a potential barrier at $X = 0$ with height V_0 and width a. A part of it is reflected with amplitude r while the rest is transmitted with amplitude t.

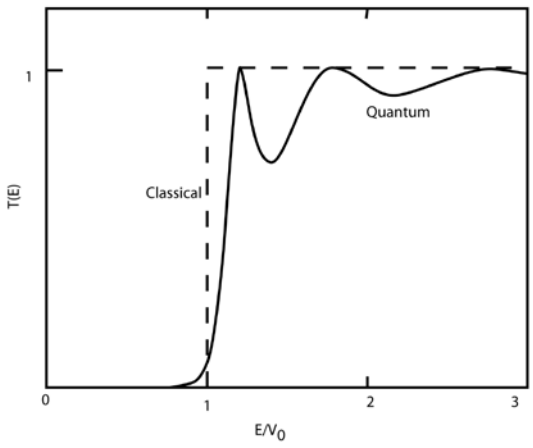

Figure 2.2 : Transmission probability for a finite potential barrier for $\sqrt{2mV_0a/\hbar} = 7$. Classical results have been shown by dashed line and quantum mechanical results have been shown by solid line.

2.4 Landauer formula for current calculation

The origin of the Landauer formula can be understood by considering current flow between two reservoirs connected by a thin wire through two leads at their ends as shown in Figure 2.3. When a small bias voltage (V) is applied then the Fermi level of the reservoirs shifts such that $E_{f1} - E_{f2} = eV$.

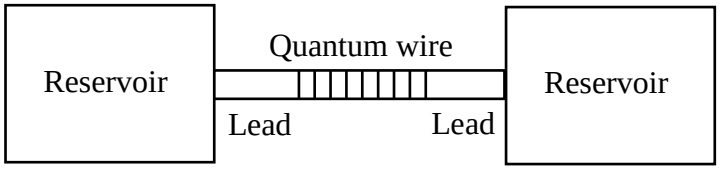

Figure 2.3. Schematic diagram of 1D system used in the derivation of the Landauer formula showing a quantum wire connecting two reservoirs through two leads.

As a result of the potential imbalance, a current flow is established through the wire whose magnitude is proportional to the number of electron in the given energy window (eV) multiplied by their respective velocity(v). For small bias the number of electrons participating in the current flow is given by density of states times the difference in the Fermi levels of the two reservoirs. For such case, the expression for the current becomes

$$I = e[n_{1D}(E)eV]v(E) \qquad 2.5$$

The velocity $v(E)$ appearing in the above equation can be calculated from the knowledge of the electronic structure of the leads. For that electronic wave packets, which are formed from

the superposition of the waves with nearly identical wave vectors, are considered as given below

$$\psi(x,t) \propto \int_{k-\frac{\Delta k}{2}}^{k+\frac{\Delta k}{2}} c(k) e^{i[kx-\omega t]}\, dk \qquad 2.6$$

Such electronic wave packets travel with group velocity v_g given by

$$v_g = \frac{\partial \omega}{\partial k} \qquad 2.7$$

For the 1d case the group velocity is given by

$$v_g = \frac{2}{\pi \hbar n_{1D}} \qquad 2.8$$

Putting the above value of the group velocity in equation 2.5 we get the expression for the current

$$I = \frac{2e^2}{h} V \qquad 2.9$$

In the above expression it is assumed that the wire does not provide any resistance and all the electrons coming from the left reservoir are transmitted to the right reservoir. In practice, however a part of the electrons are reflected at the interface. To account for that in the current calculation the current value in the above equation is multiplied by the transmission coefficient $T(E)$ and the current for such case is given by

$$I = \frac{2e^2}{h} T(E) V \qquad 2.10$$

The current, when the leads have more than one channel as shown in Figure 2.4, can be calculated by summing up the contribution due to each of those channels. It is important to note that a given channel (j) on the right receives an electron from a channel i on the left with a probability T_{ij}. The total current for this case is given by summing up contribution due to each channel j on the left which in turn receives contribution from every channel i on the right resulting in the double summation as given below.

$$I = \frac{2e^2}{h} \sum_{i,j} T_{ij}(E_F)\, V \qquad 2.11$$

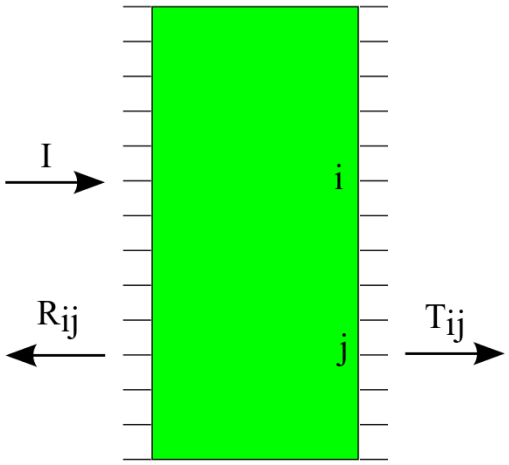

Figure 2.4: A multichannel system S. A unit current in channel i is transmitted into j with probability T_{ij} and reflected into channel j with probability R_{ij}. Both indices i and j run from 1 to N.

When a finite bias voltage is applied then the energy levels shifts as shown in Figure 2.5. To account for that the current I is calculated by integrating in the applied bias range. This gives

$$I(V) = \frac{e}{h} \int_0^{-eV} \sum_{ij} T_{ij}\big(E + E_f\big) dE$$

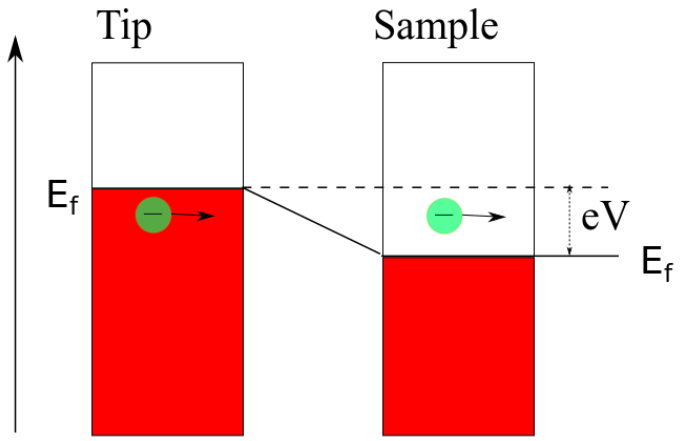

Figure 2.5: Shift in the chemical potential of the left and the right lead channels upon the application of a bias voltage V.

In the next two sections methods for the calculation of the transmission probability appearing in the Landauer formula is described in detail.

2.5 Green function approach for the transmission probability

The Green function for a system with Schrodinger equation $H|\psi\rangle = E|\psi\rangle$ is given by

$$(E - H + i\eta)G(E) = I \qquad 2.12$$

where $G(E)$ is the Green function of the system and η is an infinitesimally small number. For a given system, two Green functions exists depending on whether a positive or negative value of η is used in the calculation of the Green function. For positive η, the Green function is termed the retarded Green function (G), while for negative η, the Green function is termed as the advanced Green function $(G^{\dagger})$.

Knowledge of the Green function for a given system allows us to find its response under a constant perturbation $|v\rangle$.

$$H|\psi\rangle = E|\psi\rangle + |v\rangle \tag{2.13}$$

The response to perturbation $|v\rangle$ is

$$\begin{aligned}(E - H)|\psi\rangle = -|v\rangle \rightarrow \\ |\psi\rangle = -G(E)|v\rangle\end{aligned} \tag{2.14}$$

Thus, from the above equation it is evident that the wave function of a given system under the influence of a perturbation $|v\rangle$ is given by the Green function of the unperturbed system $G(E)$ multiplied by the perturbation $|v\rangle$. It is also possible to calculate the wave function of an unperturbed system ($|\psi\rangle$) from the knowledge of the advanced and the retarded green function under any perturbation $|v\rangle$.

$$|\psi\rangle = A|v\rangle \tag{2.15}$$

where A is called the spectral function and is defined as

$$A = i(G - G^{\dagger}) \tag{2.16}$$

This becomes evident, when we consider the two solutions of the Schrodinger equation, $|\psi^R\rangle$ and $|\psi^A\rangle$, obtained from the advanced and the retarded Green function upon the application of a perturbation $|v\rangle$.

$$|\psi^R\rangle = -G|v\rangle \tag{2.17}$$

$$|\psi^A\rangle = -G^{\dagger}|v\rangle \tag{2.18}$$

By operating $A|v\rangle$ on the Hamiltonian $(E-H)$ we find

$$(E-H)A|v\rangle = (E-H)(G-G^{\dagger})|v\rangle = (I-I)|v\rangle = 0 \qquad 2.19$$

The real advantage of the Green function method lies in the study of large systems. Such systems can be studied by dividing them into smaller subsystems resulting in large saving in the computational cost. For example, to study the current flow in a STM tunnel junction or a MTJ, the system is divided into three subsystems: the left periodic part, the defect part, and the right periodic part. The current is then determined from the modified Green function of the defect. The modified Green function takes into account the effect due to the presence of the left and the right periodic part. The origin of the modified green function can be understood by considering the Green function of the whole system.

$$\begin{pmatrix} E-H_1 & -\tau_1 & 0 \\ -\tau_1^{\dagger} & E-H_d & -\tau_2^{\dagger} \\ 0 & -\tau_2 & E-H_2 \end{pmatrix} \begin{pmatrix} G_1 & G_{1d} & G_{12} \\ G_{da} & G_d & G_{d2} \\ G_{21} & G_{2d} & G_2 \end{pmatrix} = \begin{pmatrix} I & 0 & 0 \\ 0 & I & 0 \\ 0 & 0 & I \end{pmatrix} \qquad 2.20$$

where G denotes the full Green's function and G_{ij} denotes the Green's function of its sub-matrices, H_1, H_2 and H_d represents the Hamiltonian of the left periodic part, right periodic part, and the defect, while τ_1 and τ_2 represent the interaction between the left periodic part and the defect, and right periodic part and the defect, respectively.

To find the Green function of the defect, the three equations in the second column are selected

$$(E-H_1)G_{1d} - \tau_1 G_d = 0 \qquad 2.21$$

$$-\tau_1^\dagger G_{1d} + (E - H_d)G_d - \tau_2^\dagger G_{2d} = I \quad 2.22$$

$$(E - H_2)G_{2d} - \tau_2 G_d = 0 \quad 2.23$$

From equation 2.21 and 2.23 G_{1d} and G_{2d} are calculated to have the following form

$$G_{1d} = g_1\tau_1 G_d \quad 2.24$$

$$G_{2d} = g_2\tau_2 G_d \quad 2.25$$

where g_i's are the green function of the isolated contacts, e.g., $(E - H_i)g_i = I$. Substituting the value of G_{1d} and G_{2d} in equation 2.22 and solving for G_d we obtain

$$G_d = (E - H_d - \Sigma_1 - \Sigma_2)^{-1} \quad 2.26$$

where $\Sigma_1 = \tau_1^\dagger g_1 \tau_1$ and $\Sigma_2 = \tau_2^\dagger g_2 \tau_2$ are called the self energies, which take into account the effect of the left and the right periodic part on the defect green function.

The self energies Σ_i appearing in the above equation can be expressed as a sum of real and imaginary part. For Σ_1 the values are given by

$$\Sigma_{H1}(E) = \frac{1}{2}\,[\Sigma_1(E) + \Sigma_1^\dagger(E)] \quad 2.27$$

$$\Gamma_1(E) = \; i[\Sigma_1(E) - \Sigma_1^\dagger(E)] \quad 2.28$$

Physically, Σ_H and Γ_1 represents the correction to the Hamiltonian (shift in the energy level) and the broadening of the levels due to the presence of contacts.

Once the value of A_i and Γ_i are known, the transmission probability is calculated from the relation [10]

$$T(E) = Trace(\Gamma_1 A_2) = Trace(\Gamma_2 A_1) \qquad 2.29$$

2.6 Transfer Matrix Technique for the transmission probability

The transmission probability can also be calculated using the Elastic Scattering Quantum Chemistry (ESQC) approach developed by Sautet and Joachim [6], which incorporates the transfer matrix technique [11]. To apply this technique, the barrier is assumed to form a defect in otherwise periodic system. When travelling waves encounter this defect, a part of the wave is reflected back while the rest is transmitted to the other side. This is shown schematically in Figure 2.6, where the amplitude of the incoming waves is modified due to reflection and transmission when they come out of the defect.

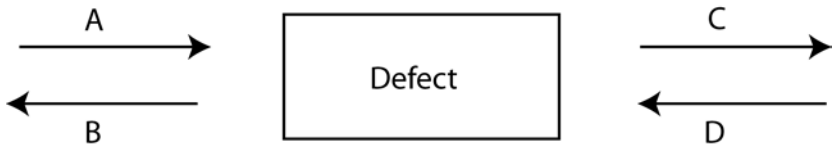

Figure 2.6: Schematic diagram showing the amplitude of the incoming (A, D) and outgoing (B, C) wave when waves traveling in a periodic lattice encounter a defect.

The relationship between the left and the right wave amplitudes is given by the transfer matrix, T(E):

$$\begin{bmatrix} C \\ D \end{bmatrix} = T(E) \begin{bmatrix} A \\ B \end{bmatrix} \qquad 2.30$$

where A, B, C, and D are the amplitudes of the various waves as shown in the Figure 2.6. Symmetry considerations dictate that the transfer matrix has the following form:

$$T(E) = \begin{bmatrix} F(E) & G^*(E) \\ G(E) & F^*(E) \end{bmatrix} \quad 2.31$$

The transmission probability, $t(E)$, for this system is calculated to have the following form:

$$t(E) = \frac{|C|^2}{|A|^2} \quad 2.32$$

2.6.1 A simplified case – one atomic orbital per cell

A model for a simple 1-D wire is shown in Figure 2.7 as an example. In the figure, e and ω are the energy levels of the periodic and the defect part, respectively. h, α and β are the coupling between the periodic parts, between the periodic part on the left and the defect, and between the defect and the periodic part on the right, respectively.

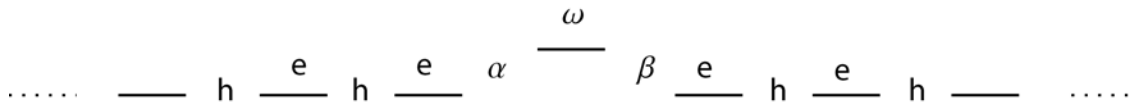

Figure 2.7: Tight binding model of 1-D linear periodic chain with defect embedded in it. The energy level of defect, and periodic part is ω and e, respectively. The coupling constant between the defect, and the left and right periodic part is α and β respectively while for coupling between atoms of the periodic part its value is h.

The wavefunction of the entire system ($|\Psi(E)\rangle$) is represented by a linear combination of the atomic orbitals ($|s_n\rangle$) of the constituent atoms.

$$|\Psi(E)\rangle = \sum_n C_n(E)|s_n\rangle \qquad 2.33$$

In the transfer matrix technique, the coefficients on the consecutive cell are calculated from the knowledge of the propagator matrix, P(E). For example, vector R_n

$$R_n \equiv \begin{bmatrix} C_n \\ C_{n-1} \end{bmatrix} \qquad 2.34$$

is related to vector R_{n+1}

$$\begin{gathered} R_{n+1} = PR_n;\ n \neq -1, 0, 1 \\ R_2 = P_0 R_{-1} \end{gathered} \qquad 2.35$$

where P is the elementary propagator along the chain, and P_0 is the propagator through the defect. The propagators are calculated by solving the Schrodinger equation of the system and for this sample 1D case in Figure 2.7 their values are given by

$$P = \begin{bmatrix} \frac{E-e}{h} & -1 \\ 1 & 0 \end{bmatrix} \qquad 2.36$$

$$P_0 = \begin{bmatrix} \frac{E-\epsilon_2}{h} & \left(-\frac{\Gamma}{h}\right) \\ 1 & 0 \end{bmatrix} \begin{bmatrix} \frac{E-\epsilon_1}{\Gamma} & \left(-\frac{\mathrm{h}}{\Gamma}\right) \\ 1 & 0 \end{bmatrix} \qquad 2.37$$

where $\epsilon_1 = \mathrm{e} + \frac{\alpha^2}{(\mathrm{E}-\omega)}$, $\epsilon_2 = e + \frac{\beta^2}{E-\omega^2}$ and $\Gamma = \frac{\alpha\beta}{E-\omega}$ .The coefficients $C_{-n}, C_{-(n-1)}$ on the far left of the defect are related by the coefficient C_{n-1}, C_n on the far right by the relation

$$R_n = P^{n-2} P_0 P^{n-2} R_{-(n-1)} \qquad 2.38$$

In order to define the transfer matrix of the system, the coefficients on the far left and the far right are expressed in terms of the amplitude of the incoming and the outgoing wave at the left and the right side of the defect. This is achieved by the application of the Bloch theorem in the left and the right periodic part assuming the contact to be perfect. The required relationships are given by

$$\begin{aligned} C_n &= Ae^{in\theta} + Be^{-in\theta} \qquad for\ large\ negative\ n \\ C_n &= Ce^{in\theta} + De^{-in\theta} \qquad for\ large\ positive\ n \end{aligned} \qquad 2.39$$

Using matrix notation, the above equations are written as

$$\begin{bmatrix} C_{-n-1} \\ C_{-n} \end{bmatrix} = \begin{bmatrix} e^{-i(n-1)\theta} & e^{i(n-1)\theta} \\ e^{-in\theta} & e^{in\theta} \end{bmatrix} \begin{bmatrix} A \\ B \end{bmatrix} \qquad 2.40$$

$$\begin{bmatrix} C_n \\ C_{n-1} \end{bmatrix} = \begin{bmatrix} e^{in\theta} & e^{-in\theta} \\ e^{i(n-1)\theta} & e^{-i(n-1)\theta} \end{bmatrix} \begin{bmatrix} C \\ D \end{bmatrix} \qquad 2.41$$

By defining $U_{n,n-1}$

$$U_{n,n-1} = \begin{bmatrix} e^{in\theta} & e^{-in\theta} \\ e^{i(n-1)\theta} & e^{-i(n-1)\theta} \end{bmatrix} \qquad 2.42$$

the above equations can be written compactly as

$$\begin{aligned} R_{-(n-1)} &= U_{(-(n-1),-n)} \begin{bmatrix} A \\ B \end{bmatrix} \\ R_n &= U_{(n,n-1)} \begin{bmatrix} C \\ D \end{bmatrix} \end{aligned} \qquad 2.43$$

The transfer matrix, the relationship between the vectors $\begin{bmatrix} C \\ D \end{bmatrix}$ and $\begin{bmatrix} A \\ B \end{bmatrix}$, is then obtained by substituting the value of R_n and $R_{-(n-1)}$ from equation 2.43 in equation 2.38. After some algebraic simplifications, the expression for the transfer matrix becomes

$$T(E) = U_{2,1}^{-1} P_0 U_{-1,-2} \qquad 2.44$$

$$\psi_n = \begin{bmatrix} C_{n1} \\ \vdots \\ C_{nN} \end{bmatrix} \qquad 2.48$$

As mentioned before the final form of the transmission matrix is

$$T(E) = \begin{bmatrix} F(E) & G^*(E) \\ G(E) & F^*(E) \end{bmatrix} \qquad 2.45$$

Which gives the value of transmission probability to be

$$t = \frac{1}{|F|^2} \qquad 2.46$$

2.6.2 The general case – several orbital per cell

In the general case, a cell A located at the n^{th} site of the periodic part is described by N atomic orbital, $\{|s_{ni}\rangle, i = 1, N\}$ while the defect cell B is described by N_0 atomic orbitals, $\{|s_{0i}\rangle, i = 1, N_0\}$.

The wave function for the above system in the tight binding approximation is given by

$$|\psi\rangle = \sum_{\substack{n=-\infty \\ n\neq 0}}^{+\infty} \sum_{i=1}^{N} C_{ni}|s_{ni}\rangle + \sum_{i=1}^{N_0} C_{0i}|s_{0i}\rangle \qquad 2.47$$

The propagator P in this case, too, relates the coefficients on the adjacent cells, more specifically it relates R_n to R_{n+1} where $R_n = \begin{bmatrix} \psi_n \\ \psi_{n-1} \end{bmatrix}$ and ψ's are column vectors of coefficients of a given cell

$$\psi_0 = \begin{bmatrix} C_{01} \\ \vdots \\ C_{0N0} \end{bmatrix} \quad 2.49$$

R_n for different values of n are related by propagator P through the relation given below

$$R_{n+1} = PR_n \; for \; |n| > 0 \quad 2.50$$

$$R_2 = P_0 R_{-1} \quad 2.51$$

From the above two equations R_N on the far left is found to be related to $R_{-(N-1)}$ on the far right by

$$R_N = P^{N-2} P_0 P^{N-2} R_{-(N-1)} \quad 2.52$$

In order to find the propagative channels, the channels that facilitates the electron on the far left of the barrier to travel to the far right of the barrier, the above equation is converted into eigenbasis of P

$$V_N = D^{2N-3} V_{-(N-1)} \quad 2.53$$

Where $D = U^{-1}PU$ is the diagonal form of P and $V_N = U^{-1}R_N$. The boundary condition on the vector of coefficients R_N dictates that its norm $\|R_N\|$ should remain bounded. This is achieved by grouping the eigenvalues of P in pairs of the form $\left(\lambda, \frac{1}{\lambda}\right)$ and choosing the

similarity matrix U such that first $2N_0$ elements of D are eigenvalues of P of moduli 1. Since only the first $2N_0$ elements satisfy the criteria for the propagative channel, the corresponding vector of coefficient V_n has the form

$$V_n = \begin{bmatrix} x_n \\ y_n \\ 0 \\ 0 \end{bmatrix} \tag{2.54}$$

Similar to the case of 1 orbital per cell, the coefficients of the far left and the far right are expressed in terms of the amplitude of the incoming and the outgoing wave at the left and the right side of the defect using Bloch theorem. Unlike the previous case, the amplitudes A, B, C and D are are column vectors whose i^{th} elements is related to the i^{th} element of the x_n and y_n by

$$\left(x_{-(N-1)}\right)_i = A_i e^{-iN\theta_i} \tag{2.55}$$

$$\left(y_{-(N-1)}\right)_i = B_i e^{+iN\theta_i} \tag{2.56}$$

$$(x_N)_i = C_i e^{-iN\theta_i} \tag{2.57}$$

$$(y_N)_i = D_i e^{-iN\theta_i} \tag{2.58}$$

The transfer matrix T is obtained by substituting the value of x and y in terms of A and B. For this case, too, the transfer matrix T is found to have the same form as 1 orbital per cell case.

$$T = \begin{bmatrix} F & G^* \\ G & F^* \end{bmatrix} \tag{2.59}$$

The transmission coefficient is then calculated to have the value

$$t = Tr(\tau\tau^+) \tag{2.60}$$

Where

$$\tau = F^{*-1}G^{*} \qquad 2.61$$

2.7 Extended Hückel Theory

2.7.1 Introduction

One of the powerful method to solve the Schrödinger equation

$$E\Phi(\vec{\boldsymbol{r}}) = \hat{H}\Phi(\vec{\boldsymbol{r}}) \qquad 2.62$$

is through the use of basis functions. In this method, the unknown wave function $\Phi(\vec{\boldsymbol{r}})$ is expressed as a sum of known functions $u_m(\vec{\boldsymbol{r}})$ with unknown coefficients ϕ_m as given below

$$\Phi(\vec{\boldsymbol{r}}) = \sum_{\mathrm{m}=1}^{\mathrm{M}} \phi_{\mathrm{m}} \mathrm{u}_{\mathrm{m}}(\vec{\boldsymbol{r}}) \qquad 2.63$$

The use of basis function allows us to turn Schrödinger equation into a linear equation. This is achieved by first substituting the value of $\Phi(\vec{\boldsymbol{r}})$ into the Schrödinger equation to give

$$E\sum_{m} \phi_m u_m(\vec{\boldsymbol{r}}) = \sum_{m} \phi_m \hat{H} u_m(\vec{\boldsymbol{r}}) \qquad 2.64$$

Multiplying both sides of the above equation by $u_n^*(\vec{\boldsymbol{r}})$ and integrating over all $\vec{\boldsymbol{r}}$ gives

$$E\sum_{m} S_{nm}\phi_m = \sum_{m} H_{nm}\phi_m \qquad 2.65$$

For each n the above equation gives a distinct linear equation. All such equations can be written compactly by using matrix notation

$$E[S]\{\phi\} = [H]\{\phi\} \qquad 2.66$$

Where $\{\phi\}$ is a column vector consisting of unknown coefficients

$$\{\phi\} = \begin{Bmatrix} \phi_1 \\ \vdots \\ \phi_M \end{Bmatrix} \qquad 2.67$$

and $[H]$ and $[S]$ are known as Hamiltonian and Overlap matrix whose nm^{th} elements are given by

$$S_{nm} = \int d\vec{\boldsymbol{r}} u_n^*(\vec{\boldsymbol{r}}) u_m(\vec{\boldsymbol{r}}) \qquad 2.68$$

And

$$H_{nm} = \int d\vec{\boldsymbol{r}} u_n^*(\vec{\boldsymbol{r}}) \hat{H} u_m(\vec{\boldsymbol{r}}) \qquad 2.69$$

In this method, the most time consuming part is the determination of the Hamiltonian and overlap matrix elements. The empirical methods avoid this time consuming step by determining the matrix elements from empirical rules as opposed to ab-initio calculations where they are calculated using equation 2.70

One of the widely used Semi-empirical method and also used in this thesis is the Extended Hückel Theory (EHT) [12]. In the EHT the elements of the Hamiltonian matrix are determined empirically as described below. The diagonal elements (H_{ii}) are set equal to the valence orbital ionization potentials (VOIP). The off-diagonal elements are approximated by the Wolfsberg-Helmholz formula [13].

$$H_{nm} = \frac{1}{2} K S_{nm} (H_{nn} + H_{mm}) \qquad 2.70$$

Where K is a constant whose value is usually taken to be 1.75, S_{nm} is overlap between atomic orbital n and m, and H_{nm} is the nm^{th} element of the Hamiltonian matrix.

The overlap matrix elements on the other hand are calculated exactly using equation 2.68. The basis function appearing in the above equation are taken to be Slater type atomic orbitals which are given by

$$S_{nlm}^{\zeta}(r,\theta,\varphi) = Nr^{n-1}e^{-\zeta r}Y_l^m(\theta,\varphi) \qquad 2.71$$

Where N is the normalization constant, n is principal quantum number of the orbital, ζ is the orbital exponent that determines the diffuseness of a given orbital, and $Y_l^m(\theta,\varphi)$ are the spherical harmonics that represent the angular part of the orbital.

2.7.2 Optimization of EHT parameters

The treatment of systems with large unit cells such as encountered in STM image calculations poses a big challenge because of their high computational needs. As a result, such systems are often studied using semi-empirical methods. Over the years, EHT has become the method of choice to treat such systems because of the several advantages it offers:

i) Simplicity and chemical insight

ii) Natural scaling laws for the interaction between atomic orbitals

For the application of this theory, it is, however, important that the chosen parameters are able to describe the electronic properties of the system under study. Generally this condition is fulfilled by deriving parameters from a fit to an accurate electronic bandstructure obtained either from ab-initio calculations or experiment.

In this thesis, we used the parameterization scheme developed by Cerda et al. [12] because of the several advantages it offers

i) Systematic way to search for the optimal value of the parameters

ii) Limited number of parameters that requires fitting without comprising the accuracy

iii) Transferability of the parameters across different geometries and different chemical environments

In the parameterization scheme by Cerda et al. [12] the value of K appearing in equation 2.70, when atomic orbitals α and β are centred on two different atoms i and j is given by

$$K_{\alpha i,\beta j} = K_{EHT} \times (E_{\alpha i} + E_{\beta j})/2 \qquad 2.72$$

In the above formula the strength of the Hamiltonian matrix element is weighted by the mean value of the on-site energy, a shift in on-site energy of the atoms does not result in an equivalent shift in the energy of the EHT-bands. Therefore, to avoid any ambiguity in the energy scale, the Fermi level of the metals have been fixed to -10 eV while for semi-conductors this has been fixed to -13 eV. Additionally, the value of the constant K has been chosen to be 2.3 as it consistently provides a better fit for all elements.

The parameter optimization is carried out by searching for the variables which minimize the root mean square deviation between the EHT band and the accurate band using the conjugate gradient method. For cases where there is a lack of good initial set of parameters, the algorithm utilizes simulated annealing optimization techniques.

As noted above basis function appearing in EHT are Slater-type orbitals. In this thesis a minimal Slater spd orbital basis set where each orbital is represented by a double ζ Slater atomic orbital has been employed. As a result we have 12 unknown variables per element, 3 onsite energy [E_s, E_p and E_d], 2 orbital exponents [$\zeta_1 and\ \zeta_2$] and the coefficient of the former (c_1) per l quantum number. The coefficient of the latter is determined by imposing the normalization condition on the wavefunction.

$$1 = \int_0^\infty c_1 \psi_{\zeta 1} d\tau \ + \int_0^\infty c_2 \psi_{\zeta 2} d\tau \qquad 2.73$$

In the Cerda parameterization scheme, it is found that a very good description of s and p orbitals of the transition metals is found by simply setting ζ_2 to a large value, i.e. $\zeta_2 > 20$. Since such a large value of the orbital coefficient leads to highly localized orbitals, these values are omitted. However, their implicit presence cause the coefficient $c_1$to assume values smaller than 1 because of the normalization condition.

2.8 Density Functional theory

2.8.1 Introduction

The Hamiltonian of a system with N electrons, in atomic units, is given by

$$\hat{H} = \sum_{i=1}^{N} [-\frac{1}{2}\nabla_i^2 + v(\vec{\boldsymbol{r}}_i)] + \frac{1}{2}\sum_i \sum_{i \neq j} \frac{1}{|\vec{\boldsymbol{r}}_i - \vec{\boldsymbol{r}}_j|} + V_{nn} \qquad 2.74$$

where $v(\vec{\boldsymbol{r}}_i)$ is the external potential arising from the interaction between electrons and nuclei and V_{nn} is the electrostatic potential among nuclei. The computation of the eigenfunctions of $\hat{H}$, a function of 3N arguments, presents a major obstacle in the study of large systems. Kohn-Sham [14-16] proved that the ground state properties can be calculated by solving self-consistently, one electron Schrodinger equation containing N orbitals $\psi(r_i)$, a function of only 3 variables

$$\left[-\frac{1}{2}\nabla^2 + v(\vec{\boldsymbol{r}}) + \int \frac{n(\vec{\boldsymbol{r}}')}{|\vec{\boldsymbol{r}}' - \vec{\boldsymbol{r}}|} d\vec{\boldsymbol{r}}' + \frac{\delta E_{xc}}{\delta n(\vec{\boldsymbol{r}})}\right] \psi_\alpha(\vec{\boldsymbol{r}}) = \epsilon_\alpha \psi_\alpha(\vec{\boldsymbol{r}}) \qquad 2.75$$

Where E_{xc} is the exchange-correlation energy that accounts for the exchange and the correlation energy missed in the one electron picture.

2.8.2 Overview of the approximations

Even with this simplification, the solution of the Kohn-Sham equation remains formidable. Further simplification is achieved by approximating exchange-correlation functional, using pseudopotential theory to model ion-electron interactions and special k-point integration schemes to obtain the expectation values of the desired properties. A brief discussion of all the issues is provided below

2.8.2.1 Exchange-correlation functional

The density functional theory derives its usefulness from the fact that simple approximations for the functional E_{xc} provide a good description of real systems. Also, the possibility of further refinement opens the door to reach the higher level of accuracy. The general expression for E_{xc} is given by

$$E_{xc} = \int n(\vec{\boldsymbol{r}})\epsilon_{xc}(n, \vec{\boldsymbol{r}})d\vec{\boldsymbol{r}} \qquad 2.76$$

where ϵ_{xc} is exchange-correlation energy per electron.

There exists a hierarchy of approximations for ϵ_{xc} that employ increasingly realistic approximation. At the lowest level is the local density approximation (LDA) which uses only the local electron density to construct this functional. The next level is called the generalized gradient approximation (GGA) and uses the density gradient in addition to the local electron density. Even more sophisticated functionals are constructed using the Kohn-Sham orbital ψ_α in the vicinity of volume element $d\vec{\boldsymbol{r}}$. In general, each additional term leads to additional constraints being satisfied and hence better description of the system. One such constraint arises because of the electron number conservation, the Pauli exclusion principle and Coulomb repulsion whereby each electron finds itself surrounded by a hole whose density satisfy the following sum rule

$$\int n_{xc}(\vec{\boldsymbol{r}}, \vec{\boldsymbol{r}}')d\vec{\boldsymbol{r}}' = -1 \qquad 2.77$$

a) Local density approximation

In the local density approximation [14], the exchange energy is given by

$$E_{xc} = \int n(\vec{\boldsymbol{r}})\epsilon_{xc}^{unif}(n, \vec{\boldsymbol{r}})d\vec{\boldsymbol{r}} \qquad 2.78$$

where ϵ_{xc}^{unif} is the exchange correlation energy per particle of an electron gas with uniform spin density $n(\vec{\boldsymbol{r}})$ which is known accurately. For solid and solid surfaces LDA works surprisingly well. Confirming that actual electron density in such systems is very well described by uniform electron gas. Interestingly, LDA works better as a whole then when it is used to estimate E_x and E_C, separately. The opposite nature of the non locality of the exchange and the correlation energy leads to cancellation of the errors when they are approximated in similar fashion [17].

The application of LDA to atoms and molecules leads to reasonable molecular geometries and the vibrational frequencies but their atomization energy is grossly overestimated [18].

b) Generalized Gradient Approximation

In the generalized gradient approximation (GGA), the exchange energy is given by

$$E_{xc} = \int n(\vec{\boldsymbol{r}})\epsilon_{xc}^{unif}(n, \vec{\boldsymbol{r}}, \nabla n(\vec{\boldsymbol{r}}))d\vec{\boldsymbol{r}} \qquad 2.79$$

There are quite a few different types of GGA which differ in how they employ the charge density and the gradient to construct the functional.

The second-order gradient correction approximation (GE2) [14] results from incorporating the leading correction in LDA in systems where the spin density varies slowly in space.

For realistic densities, application of GE2 leads to serious overcorrection to LDA. For instance, the negative correlational energies of atoms in LDA become improperly positive [19]. The worse performance of GE2 compared to LDA for realistic densities arises as it violates the sum rule [20].

The PBE GGA functional [21] form satisfies the sum rule as well as the negative definite exchange hole condition. As a result PBE functional provides an accurate description of the binding energies compared to the LDA energies.

2.8.2.2 Pseudopotential theory

Pseudopotential theory [22] allows us to substitute the strong electron ion potential with a much weaker potential, known as the pseudopotential that reproduces all the major features of a valence electron in a solid. Since, in a weaker potential, wave function oscillation is reduced, a relatively small set of plane waves are needed in the expansion of the wave function which simplifies the solution of the Schrodinger equation considerably. One of the biggest drawbacks of the pseudopotential method is that all the information about the wavefunction is lost in the vicinity of the nuclei. The Projector augmented-wave (PAW) [23] method avoids this without being computationally intensive. It does that by transforming the physical wave function $\psi(\vec{r})$, into a smooth auxiliary wave function $\widetilde{\psi}(\vec{r})$, that is easily represented in a plane wave expansion

$$\tilde{\psi}(\vec{r}) = \tilde{u}\psi(\vec{r}) \qquad 2.80$$

The Schrodinger equation is then solved in the transformed space and the properties of the system are obtained by appropriately transforming the values obtained in the transformed space.

PAW calculations improve magnetization energies. They also lead to better description of alkali, alkaline earth and early transition metal geometry description [24].

2.8.2.3 K-point integration scheme

The translational symmetry gives rise to a quantum number $\vec{k}$, known as the crystal momentum. The expectation values of one-particle properties are calculated from the integral of the matrix elements in the Brillouin zone. For the Brillouin zone integration two different methods have been proposed in the literature.

i) Special point scheme: These methods are applicable to only insulators and semi-conductors. In this method, Brillouin zone integration is obtained from the weighted sum over the selected k-points. The most widely used special k-point sets are due to Monkhorst and Pack [25] who proposed an equi-spaced grid of k-points.

ii) Tetrahedron method [26-27]: This is more general scheme that is applicable for both insulators as well as metals. In addition to that, this method also provides better spectral function. In this scheme, the reciprocal space is divided into tetrahedral. Inside the tetrahedral, the band energies and the matrix elements are linearized in $\vec{k}$.

Because of the linearization, this method allows analytical integration of the Brillouin zone.

2.9 GW calculation

The Hamiltonian of a many electron system is given by

$$H = \sum_i \left[-\frac{1}{2} \nabla^2(\vec{\boldsymbol{r}}_i) + V(\vec{\boldsymbol{r}}_i) \right] + \frac{1}{2} \sum_{i \neq j} \frac{1}{|\vec{\boldsymbol{r}}_i - \vec{\boldsymbol{r}}_j|} \qquad 2.81$$

Where $V(\vec{\boldsymbol{r}}_i)$is the external potential due to the presence of the nuclei and second summation gives the value of the electron-electron interaction. Over the years various approximations have been used to describe the electron-electron interaction. In the Hartree approximation the non-local electron-electron coulomb interaction is replaced by an average Coulomb interaction. Although this approximation results in reasonable description of a system, in many cases the calculated results deviate quite significantly from the experimentally determined value. Hartree-Fock Approximation (HFA), which also includes non-local exchange energy that accounts for the Pauli Exclusion Principle resulted in better description of the system. HFA works quite well for the atoms. However, the band gap of solids is overestimated within this formalism as the electron correlation or screening effect is not taken into account.

Further improvement in the description of solids came about from the formulation of Density Functional Theory (DFT). In DFT the system of interacting electrons is mapped onto a system of non-interacting electrons moving in an average potential due to all other electrons.

The effect of exchange and correlation is included by the addition of an extra term called exchange-correlation potential V_{xc}.

$$(T + V_{ext} + V_H)\psi_{nk}(\vec{r}) + V_{xc}(\vec{r})\psi_{nk}(\vec{r}) = \varepsilon_{nk}^{DFT}\psi_{nk}(\vec{r}) \qquad 2.82$$

Where T is the kinetic energy, V_{ext} is the external potential due to the presence of nuclei, V_H is the Hartree energy that describes electron-electron interaction, V_{xc} is the exchange-correlation potential that accounts for the many body interaction which is missed in one-electron equation, and ψ_{nk} is the wave function of an electron with band index n and momentum vector k. In principal, this formalism provides an exact solution for the ground state properties and has been quite successful in predicting many ground state properties. However, properties like band gap is underestimated. For example, DFT band gap for Si calculated with LDA functional is 0.6 eV which is much smaller compared to the experimentally measured band gap of 1.25 eV.

There have been a number of explanations given in the literature. According to Par and Yang [28] there is no simple physical meaning attached to Kohn-Sham orbital energies except for the highest occupied orbital energy that equals the negative of the ionization potential. Dreizler and Gross on the other hand state that the Kohn-Sham band gap is indeed exact for a non-interacting system [29]. For an interacting system, the correct band gap is obtained by adding the discontinuity in the exchange-correlation potential to the Kohn-Sham band gap. Williams and Von Barth [30] argue that it is the local nature of the functional that leads to incomplete cancellation of the self-interaction energy that is responsible for the underestimation of the band gap.

Many body perturbative theory corrects for this behaviour by considering a system of Quasi Particles (QP) that interact via non-local and energy dependent self-energy Σ. In this formalism the wave function and the energies are obtained from the equation given below

$$(T + V_{ext} + V_H)\psi_{nk}(\vec{\boldsymbol{r}}) + \int d^3\vec{\boldsymbol{r}}' \sum(\vec{\boldsymbol{r}}, \vec{\boldsymbol{r}}'; E_{nk})\psi_{nk}(\vec{\boldsymbol{r}}') = \varepsilon_{nk}^{QP}\psi_{nk}(\vec{\boldsymbol{r}}) \quad 2.83$$

The above equation is the same as the DFT equation except for the fact that local exchange correlation potential V_{xc} has been replaced by the non-local and the energy dependent self-enegy Σ.

The self energy Σ accounts for the many body effect by incorporating the effect of the exchange and the correlation. One of the most widely used expression for the self energy known as GW approximation was derived by Hedin that considers only the first term in the expansion of the self-energy arising from a many-body perturbation theory [31]. In the GW approximation by Hedin the self energy is given by

$$\Sigma(1,2) = iG(1,2)W(1,2) \quad 2.84$$

where Σ, G and W represent the self energy, the green function and the screened Coulomb potential of the system while 1 and 2 are abbreviated notation for $(\vec{\boldsymbol{r}}_1, t_1)$ and $(\vec{\boldsymbol{r}}_2, t_2)$, respectively. The green function of the system describes the propagation of the particle while the screened Coulomb potential describes how the bare interaction is modified in the presence of other electrons. In the later paragraphs we describe in detail the meaning as well

as the method to obtain Green function and the screened Coulomb potential. Here we describe how these calculations are carried out.

The calculations within GW approximations are carried within two steps. In the first step DFT calculations are carried out to obtain DFT orbitals and eigenvalues. These are then used a first guess to obtain green function and the screened interaction. In the second step, Dyson equation (see equation 2.66) is used to calculate the green function of the system. In principle, this process of obtaining new green function from the old green function should be continued till self-consistency is achieved. In practice, however, due to large computational cost involved the calculations are often terminated before the full self-consistency is achieved. For example, the calculations where one stops after the first iteration is termed as G_0W_0. The other calculation which employ fully self-consistent green function and screened interaction obtained after the first iteration are termed as GW_0. And the calculations which employ fully self-consistent green function as well as the screened interaction are termed as GW.

2.9.1 Green function

The green function of a system described by Schrodinger equation

$$[i\partial_t - H_0(r)]\Psi_0(\vec{\boldsymbol{r}}, t) = 0 \qquad 2.85$$

is given by

$$[i\partial_t - H_0(\vec{\boldsymbol{r}})]G_0(\vec{\boldsymbol{r}},\vec{\boldsymbol{r}}';t,t') = \delta(\vec{\boldsymbol{r}}-\vec{\boldsymbol{r}}')\delta(t-t') \qquad 2.86$$

The green function defined above is also called a propagator because it propagates the wave function. If the wave function is known at some time then the wave function at later times is given by

$$\Psi_0(\vec{\boldsymbol{r}},t) = \int dr' \int dt' G_0(\vec{\boldsymbol{r}},\vec{\boldsymbol{r}}';t,t')\Psi_0(\vec{\boldsymbol{r}}',t') \qquad 2.87$$

This can be verified by inserting equation (2.87) into the Schrodinger equation(2.85) and using the definition 2.86.

The most important application of the Green function lies in the determination of the green function of the interacting system from the knowledge of the green function of non-interacting system using Dyson equations. Here, we are giving the proof for the time-independent case for the sake of simplicity.

For the derivation we consider the Schrodinger equation

$$[H_0(\vec{\boldsymbol{r}}) + V(\vec{\boldsymbol{r}})]\Psi_E = E\Psi_E \qquad 2.88$$

Where H_0 is the Hamiltonian for the system with non-interacting particles whose eigenstates are known. The term $V(\vec{\boldsymbol{r}})$ describes the change in the system's Hamiltonian when the interactions between the particles are turned on. The green function of the interacting system

$G(\vec{\boldsymbol{r}})$ is determined from the knowledge of the the green function G_0 of the non-interacting system.

$$\big(E - H_0(\vec{\boldsymbol{r}})\big)G_0(\vec{\boldsymbol{r}}, \vec{\boldsymbol{r}}'; E) = \delta(\vec{\boldsymbol{r}} - \vec{\boldsymbol{r}}') \qquad 2.89$$

The above equation can also be written in terms of inverse of $G_0^{-1}(\vec{\boldsymbol{r}}, E)$ which is defined as

$$G_0^{-1}(\vec{\boldsymbol{r}}, E) = E - H_0(\vec{\boldsymbol{r}}) \; or \; G_0^{-1}(\vec{\boldsymbol{r}}, E)G_0(\vec{\boldsymbol{r}}, \vec{\boldsymbol{r}}', E) = \delta(\vec{\boldsymbol{r}} - \vec{\boldsymbol{r}}') \qquad 2.90$$

The solution to the equation 2.88 can be written as an integral equation

$$\Psi_E(\vec{\boldsymbol{r}}) = \Psi_E^0(\vec{\boldsymbol{r}}) + \int d\vec{\boldsymbol{r}}' G_0(\vec{\boldsymbol{r}}, \vec{\boldsymbol{r}}', E)V(\vec{\boldsymbol{r}}')\Psi_E(\vec{\boldsymbol{r}}') \qquad 2.91$$

Or in terms of the full green function

$$\Psi_E(\vec{\boldsymbol{r}}) = \Psi_E^0(\vec{\boldsymbol{r}}) + \int d\vec{\boldsymbol{r}}' G(\vec{\boldsymbol{r}}, \vec{\boldsymbol{r}}', E)V(\vec{\boldsymbol{r}}')\Psi_E^0(\vec{\boldsymbol{r}}') \qquad 2.92$$

This is verified by inserting Ψ_E from 2.81 (2.82) into equation 2.88 and then using 2.90. The integral equation in 2.91 can be solved by iteration and upto first order in V the solution is

$$\Psi_E(\vec{\boldsymbol{r}}) = \Psi_E^0(E) + \int d\vec{\boldsymbol{r}}' G_0(\vec{\boldsymbol{r}}, \vec{\boldsymbol{r}}', E)V(\vec{\boldsymbol{r}}')\Psi_E^0(\vec{\boldsymbol{r}}') + \mathcal{O}(V^2) \qquad 2.93$$

Where Ψ_E^0 is an eigenstate to H_0 with eigenenergy E. By iterating the solution we get

$$\begin{aligned}\Psi &= \Psi^0 + G_0 V\Psi^0 + G_0 V G_0 V\Psi^0 + G_0 V G_0 V G_0 V\Psi^0 + \cdots \\ &= \Psi^0 + (G_0 + G_0 V G_0 + G_0 V G_0 V G_0 + \cdots) V\Psi^0\end{aligned} \quad 2.94$$

In the above equation the integration variable have been suppressed for the sake of simplicity. By comparison with equation (2.92) we see that the full Green's function G is given by

$$\begin{aligned}G &= G_0 + G_0 V G_0 + G_0 V G_0 V G_0 + \cdots \\ &= G_0 + G_0 V(G_0 + G_0 V G_0 + \cdots)\end{aligned} \quad 2.95$$

We arrive at the Dyson equation by noting that the last parenthesis is nothing but G itself

$$G = G_0 + G_0 V G \quad 2.96$$

2.9.2 Screened Coulomb energy

The screened coulomb energy W is given by

$$W(\vec{\boldsymbol{r}}, \vec{\boldsymbol{r}}'; \omega) = \Omega^{-1} \int d^3\vec{\boldsymbol{r}}'' \epsilon^{-1}(\vec{\boldsymbol{r}}, \vec{\boldsymbol{r}}''; \omega) v(\vec{\boldsymbol{r}}'', \vec{\boldsymbol{r}}') \quad 2.97$$

Where Ω is the crystal volume, v is the coulomb energy ($v(\vec{\boldsymbol{r}}'', \vec{\boldsymbol{r}}') = e^2/|\vec{\boldsymbol{r}}'' - \vec{\boldsymbol{r}}'|$), and $\epsilon(\vec{\boldsymbol{r}}, \vec{\boldsymbol{r}}'; \omega)$ is the frequency dependent dielectric function. The dielectric function provides a measure of the screening encountered in a given system. It is calculated from the change in the total potential, δV_{tot}, due to a small variation in the external potential, δV_{ext}.

$$\delta V_{tot} = \epsilon^{-1} \delta V_{ext} \quad 2.98$$

The dielectric function is determined from the independent particle polarizability χ_0, which gives the change in the electron density $\delta\rho$ due to total perturbing potential δV_{tot}

$$\delta\rho(\vec{\boldsymbol{r}}) = \int d\vec{\boldsymbol{r}}'\chi_0(\vec{\boldsymbol{r}},\vec{\boldsymbol{r}}')\delta V_{tot}(\vec{\boldsymbol{r}}') \qquad 2.100$$

In the Random Phase Approximation (RPA) the dielectric function and the independent particle polarizability are related by

$$\epsilon_{RPA} = 1 - v\chi_0 \qquad 2.101$$

Finally the independent particle polarizability χ_0 is calculated from DFT using Adler-Wiser expression. Its value in reciprocal space is given by

$$\chi^{(0)}_{G,G'}(q,\omega) = 2\sum_{n,n',k}\left(f_{n,k} - f_{n',k+q}\right)\frac{\langle\psi^{DFT}_{n',k+q}|e^{-i(q+G)r}|\psi^{DFT}_{n,k}\rangle\langle\psi^{DFT}_{n,k}|e^{(-iq+G')r}|\psi^{DFT}_{n',k+q}\rangle}{\varepsilon^{DFT}_{n,k} - \varepsilon^{DFT}_{n',k+q} - \omega - i\delta} \qquad 2.102$$

Appendix

2A.1 Bra-Ket notation

In the bra-ket notation, a wavefunction is represented using a "ket" $|\dots\rangle$, For example,

ψ_i is written as $|i\rangle$.

The complex conjugate of a wavefunction is written as a "bra" $\langle\dots|$, for example,

ψ_i^* is written as $\langle i|$.

The rule is that if a bra appears on left and a ket appears on the right, integration over $d\tau$ is implied. So

$$\langle j||i\rangle \equiv \int \psi_j^* \psi_i d\tau \qquad \text{A.1}$$

Generally, the middle vertical lines are merged. So we have $\langle j|i\rangle$.

Bra-ket notation is very compact. For example, the normalization and orthogonality condition can be written as

$$\langle i|i\rangle = 1 \text{ and } \langle j|i\rangle = 0 \qquad \text{A.2}$$

A frequently encountered integral in quantum mechanics is $\int \psi_j^* \widehat{H} \psi_i$ which in the bra-ket notation becomes $\langle j|H|i\rangle$

References

[1] R. Landauer, *IBM J. Res. Dev.* **32**, 306 (1988).

[2] J. Cerdá, M. A. Van Hove, P. Sautet, and M. Salmeron, *Phys. Rev. B* **56**, 15885(1997).

[3] P. Sautet and C. Joachim, *Chem. Phys. Lett.* **185**, 23 (1991).

[4] J. Mathon and A. Umerski, *Phys. Rev. B* **63**, 220403 (2001).

[5] J. Mathon, A. Umerski, and M. Villeret, *Phys. Rev. B* **55**, 14378 (1997).

[6] P. Sautet and C. Joachim, *Phys. Rev. B* **38**, 12238 (1988).

[7] F. Aryasetiawan and O. Gunnarsson, *Rep. Prog. Phys.* **61,** 237 (1998).

[8] David J. Griffiths, *Introduction to Quantum Mechanics*, 2nd ed. (Benjamin Cummings, 2004).

[9] M. Büttiker, Y. Imry, R. Landauer, and S. Pinhas, *Phys. Rev. B* **31**, 6207 (1985).

[10] Supriyo Datta, *Quantum Transport: Atom to Transistor*, 2nd ed. (Cambridge University Press, 2005).

[11] H. Schmidt, *Phys. Rev.* **105**, 425 (1957).

[12] J. Cerdá and F. Soria, *Phys. Rev. B* **61**, 7965 (2000).

[13] M. Wolfsberg and L. Helmholz, *J. Chem. Phys.* **20**, 837 (1952).

[14] W. Kohn and L. Sham, *Phys. Rev.* **140**, A1133-A1138 (1965).

[15] P. Hohenberg and W. Kohn, *Phys. Rev.* **136**, B864-B871 (1964).

[16] W. Kohn and L. Sham, *Phys. Rev.* **137**, A1697-A1705 (1965).

[17] J. P. Perdew and K. Schmidt, *AIP Conf. Proc.* **577**, 1 (2001).

[18] R. O. Jones, and O. Gunnarsson, *Rev. Mod, Phys.* **61**, 689 (1989).

[19] S.-K. Ma, and K. A. Brueckner, *Phys. Rev.* **165**, 18 (1968).

[20] D. C. Langreth, and J. P. Perdew, *Phys. Rev, B* **21**, 5469 (1980).

[21] J. P. Perdew, K. Burke, and M. Ernzerhof, *Phys. Rev. Lett.* **77**, 3865 (1996).

[22] J. C. Phillips, *Phys. Rev.* **112,** 685 (1958).

[23] P. E. Blochl, *Phys. Rev. B*, **50**, 17953 (1994).

[24] G. Kresse, D. Joubert *Phys. Rev. B*, **59**,1759 (1999)

[25] H. J. Monkhorst, J.D. Pack, Phys. Rev. B **13**, 5188 (1976).

[26] O. Jepsen, O. K. Andersen, *Solid State Commun.* **9**, 1763 (1971).

[27] G. Lehmann, M. Taut, *Phys. Status Solidi B* **54**, 469 (1972).

[28] P. G. Parr and W. Yang, *Density-Functional Theory of Atoms and Molecules*; Oxford University Press: New York, 1989.

[29] R. M. Dreizler and E. K. U. Gross, *Density Functional Theory*; Springer-Verlag: Berlin, 1990.

[30] A. R. Williams and U. von Barth, Applications of Density Functional Theory to Atoms, Molecules, and Solids. In *Theory of the Inhomogeneous Electron Gas*; Lundqvist, S., March, N. H., Eds.; Plenum Press: London, 1983.

[31] L. Hedin, *Phys. Rev.* **139**, A796 (1965).

CHAPTER 3

Origin of the contrast inversion in the STM image of CO on Cu(111)

3.1 Introduction

Scanning tunneling microscopy (STM) has revolutionized surface science by providing atomic resolution images of surface structures and processes [1]. STM image contrast results from a complex interplay between the adsorbate and the surface electronic structure, as well as from the electronic interaction of the STM tip with the substrate via the adsorbate. It therefore requires calculations, accounting for the electronic structure of the surface, the adsorbate, and the STM tip, to extract the atomic surface structure from an experimental STM image [2]. STM image calculations not only allow linking experimental STM images to surface structures, but also provide a chemical interpretation of the STM contrast. Often, the STM contrast does not correspond to a steric model of the proposed surface structure, and contrast inversion can be observed, where CO adsorption on Cu(111) is a well-known example. Indeed, a low temperature STM study by Bartels et al. [3] shows that CO molecules adsorbed at top sites on Cu(111) appear as dark depressions in STM images for a range of bias voltages. This observation indicates that an adsorbed CO molecule reduces the conductance of the tip–CO–surface tunneling junction. Similar observation has also been made by Lauhon et al. who find that CO appears as a depression on Cu(100) [26].

Using tight-binding simulations, Nieminen et al. [4] have attributed the reduced tunneling current upon CO adsorption on Cu(111) to interference between electron waves passing through the adsorbate states and electron waves passing through space directly from the tip to the surface. Using a quantum nanodynamics theory, Drakova et al. [5] argue that the current

in the vicinity of a CO molecule adsorbed on Cu(111) is reduced by a dynamic relaxation of transient electronic states of the metal surface created by the injection of electrons from the STM tip. Contrary to CO on Cu(111), the STM image of CO on Pt(111) shows a protrusion surrounded by a spherical depression. The protrusion is significantly smaller than the steric height of the CO molecule. Bocquet and Sautet [6] attribute the spherical depression surrounding the CO molecule to a perturbation of the surface electronic structure by adsorbed CO.

A theoretical interpretation of STM images hence requires an accurate description of the surface electronic structure. Cu(111) is characterized by a Shockley-type surface state, the states that arise due to the change in the electron potential associated only with the crystal termination, arising in the L-gap of the bulk Cu reciprocal space [7]. This surface state has been studied experimentally and theoretically [7], [8] and [9]. Angle Resolved Photo Electron Spectroscopy (ARPES) reveals a surface state with a parabolic, free-electron-like dispersion, with a minimum at the Γ-point of the surface Brillouin zone, about 0.4 eV below the Fermi energy of the Cu(111) surface [7] and [10]. A similar parabolic dispersion is found in our calculations (Figure 3.1). The wave functions associated with the surface state are highly delocalized along the surface and confined near the surface by the vacuum potential [8]. Because of these characteristics, the Cu(111) surface state is a two-dimensional surface state and has been modeled as a 2-D jellium and a 2-D electron gas [11].

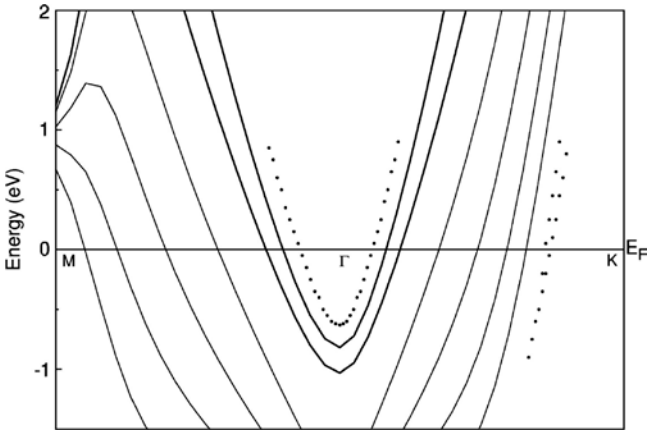

Figure 3.1 DFT-PBE band structure for Cu(111). Bands associated with the surface state for both sides of the slab are indicated in bold. EHMO surface states between −1 eV below and +1 eV above the Fermi energy are indicated by dotted lines.

Using an accurate description of the Cu(111) surface state, its interaction with adsorbed CO and with the STM tip, it is shown that the decrease in the tunneling current upon CO adsorption is due to the strong interaction between the CO 5σ orbital and the Cu $4p_z$ components of the surface state. The 5σ molecular orbital of adsorbed CO couples strongly with the $4p_z$ of Cu surface states, creating bonding and antibonding states, and depleting the $4p_z$ electron density near the Fermi level. For the clean Cu(111) surface, $4p_z$ derived surface states carry most of the tunneling current since they dominate the Density of States (DOS) near the Fermi energy and their spatial orientation facilitates overlap with the tip. Although the tails of the CO-induced states, in particular the 2π* orbital, have some weight at the Fermi level, the electron density associated with them is small compared to the total density near the Fermi energy at clean Cu sites. Finally, a 1-dimensional tight-binding model is presented to illustrate how the STM contrast results from the over-coupling between the surface state and the molecule.

3.2 Computational methods

STM images were calculated using the Elastic Scattering Quantum Chemistry (ESQC) approach [2]. This approach allows calculating the conductance of a defect embedded in an infinite periodic material. For this purpose, the system is modelled as …..AAAABAAAA…., where A represents the periodic part which is repeated infinitely to the left and right and B represents the defect [12]. In the STM image calculations, the bulk of the tip and bulk of the substrate constitute the periodic parts (A), while the apex of the STM tip, the adsorbed molecule, and the surface region represent the defect (B). Each periodic part (A) is described by three layers of Cu(111). The defect (B) is described by six atomic layers of Cu(111), the CO and a tetrahedral tip. Six Cu(111) atomic layers are required to ensure that the surface states are localized in the defect part. The localization of the surface states is verified by orbital decomposition of the surface states. For six atomic layers, the orbital decomposition shows negligible contribution from the atoms at the bottom of the defect to the surface states. A lateral dimension of 10.2 Å (4 Cu–Cu distances) was used to minimize interactions between CO molecules in the neighboring unit cells when lateral cyclic boundary conditions are applied in ESQC. An energy step of 0.1 eV is employed in the calculation of $T(E)$. The tunneling spectrum through the defect, $T(E)$, is calculated from the full scattering matrix of the tip–molecule–surface junction. The tunneling current is then obtained from the Landauer formula [13]:

$$I(V) = \frac{e}{h}\int_{-\infty}^{+\infty} T(E)\left[f_0(E-(E_F-eV/2)\right) - f_0\left(E-(E_F+eV/2)\right)dE \qquad 3.1$$

which, for low bias, simplifies to:

$$I = \frac{2e^2}{h}\, T(E_F)V \qquad 3.2$$

where f_0 is the Fermi function, E_F is the Femi energy, V is the bias voltage, and $T(E)$ the electronic transmission spectrum through the tunneling junction.

The atomic details of the Cu(111) surface and bulk, of the adsorbed CO molecule, and of the STM tip, as well as their electronic interactions, are fully taken into account using a linear combination of Slater type atomic orbitals (LCAO) representation. Bloch states propagating in the semi-infinite periodic part define the incoming and scattered states used to calculate the electronic transmission spectra, $T(E)$, of the STM junction. The extended Hückel molecular orbital (EHMO) model was used to construct the electronic Hamiltonian of the tunnel junction because of the simplicity and chemical insight it offers [14]. To accurately describe the electronic structure of the Cu(111) surface, and in particular its Shockley-type surface state (Shockley-states are the states that appear in the middle of the energy gap when s and p bands cross. These states appear even when no surface potential perturbation is present. This is in contrast to Tamm states that appear only when there is a potential perturbation at the surface), the extended Hückel parameters were re-optimized for surface and subsurface Cu atoms, following a procedure described by Cerdá and Soria [15]. The available Cu EHT parameters are bulk parameter. For sp bonded elements both experiments and ab-initio calculations show that upon creation of surface new states appear close to the Fermi level. These surface states change the IV characteristics of Cu(111) surface dramatically. For example Eigler et al. [9] find that there is a sudden increase in dI/dV value at the location of the surface state. In order to ensure that our theory is able to describe these effects, we reparametrized the EHT.

The re-optimization procedure ensures a better transferability of the parameters for their use in a different chemical environment [15]. In the EHMO Hamiltonian, each Cu atom is described by a basis set of s, p and d orbitals. The on-site energies (E_s, E_p and E_d), the orbital exponents (ζ_1 and ζ_2) and the coefficients for the former (c_1) for each atomic orbital are determined by fitting the EHMO band structure to the energy and momentum resolved projected DOS obtained from Density Functional Theory (DFT) calculations described below. Normalization of the wave function gives the coefficients c_2. The STM tip apex atom orbitals were optimized to recover the exponential decay of the tunneling current with tip height [16] for the clean Cu(111) surface, consistent with a Cu(111) workfunction of 4.94 eV [17]. The EHMO parameters are provided in Table 3.1 of the Supporting Information. In the ESQC calculations, the atoms in the top three layers of the defect are described by the surface, subsurface, and sub subsurface parameters, respectively. The bottom three layers of the defect (B) are described by the bulk parameters. As stated earlier, the bottom three layers in the defect (B) ensure that the surface states are localized in the defect part. Indeed, the Cu(111) surface states are not completely localized on the surface atoms, but decay exponentially into the bulk, as also observed in DFT calculations [10]. Atoms in the periodic part act only as an electron reservoir and are described by bulk 4s orbitals. The interaction responsible for the STM image formation of CO occurs between the CO states and the surface states which are part of the defect region. We, can, therefore choose the nature of the bulk electrons that is computationally less expensive. This simplified description of the periodic part makes the calculation of such a large system possible without changing any of the physics behind the problem.

Surface states for the semi-infinite system were identified as solutions of the Schrödinger equation arising as a combination dominated by atomic orbitals of surface atoms, using the Green function method [18] (scatter points in Figure 3.1). A similar procedure is not

implemented in plane wave DFT calculations; instead surface states were identified from the projected DOS (bold lines in Figure 3.1).

The CO adsorption energy and the Cu(111) band structure were calculated using DFT with the Perdew–Burke–Ernzerhof functional [19] as implemented in the Vienna Ab initio Simulation Package (VASP) [20] and [21]. The calculations were performed using a plane wave basis, a cut-off kinetic energy of 400 eV, and projector-augmented-wave (PAW) pseudopotentials [22] and [23] to describe the inner shell electrons. A Γ-centered Monkhorst-Pack grid with nine subdivisions along each of the surface reciprocal vectors was used. To compute the surface band structure, the high symmetry directions in the hexagonal surface Brillouin zone were sampled. The Cu(111) surface was modeled as a 9-layer fcc slab, separated by a 10 Å vacuum layer, where the top and bottom two layers were relaxed. With this slab thickness, the dispersion relations for the top and bottom surface bands are nearly degenerate, with a splitting due to interaction through the bulk of about 0.2 eV at the Γ point (Figure 3.1). Increasing the slab thickness to 13 layers reduces the splitting to 0.06 eV, but does not affect the overall character of the surface bands. The binding energy for the surface band at the Γ-point, 0.6–0.7 eV below the Fermi energy, is in reasonable agreement with the experimental value, 0.4 eV below the Fermi energy [7]. CO adsorption at top sites was calculated on a 5-layer, p(2 × 2) Cu(111) slab. The top two layers were relaxed, while the bottom layers were constrained at their bulk positions. The optimized Cu–C and C–O distances of 1.84 and 1.16 Å, and the CO binding energy of −0.58 eV, agree well with literature values [24]. Upon adsorption, the C–O bond length is calculated to increase by 0.0165 Å.

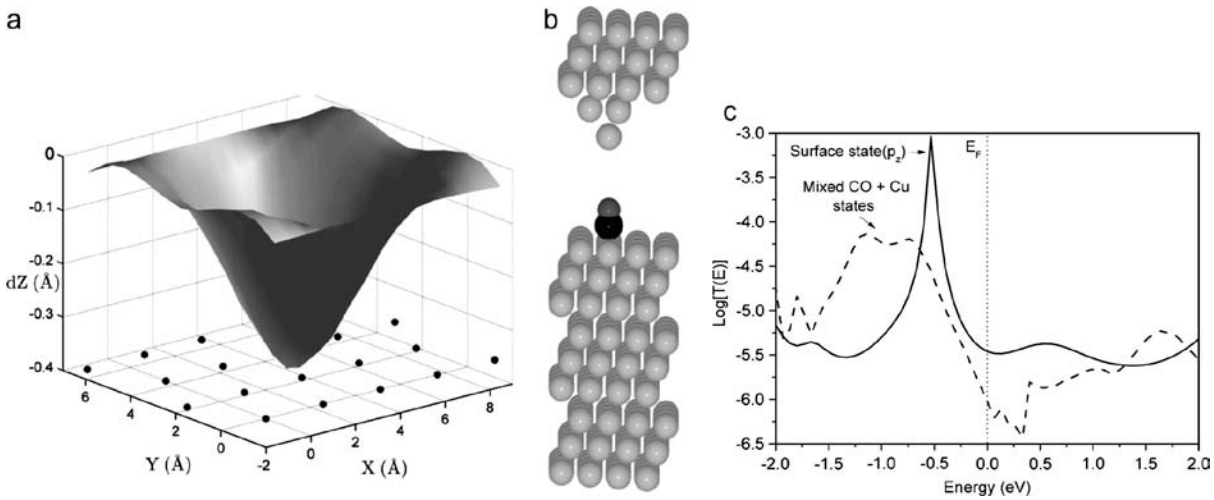

Figure 3.2 (a) Calculated constant current STM image for CO adsorbed at a top on the Cu(111) surface. Bias voltage of 50 mV and a current of 0.1 nA. The surface Cu atoms are indicated (●). (b) STM junction structure used in the calculations. (c) The *T*(*E*) spectra for the clean Cu(111) surface (—) and for the junction with an adsorbed CO (- - -).

3.3 Results and discussion

First, we discuss the band structure of the Cu(111) surface to illustrate the accuracy of the fitted parameters in the EHMO Hamiltonian. Next, the electronic transmission spectrum of the junction, *T*(*E*), is calculated and the constant current STM image showing a clear depression at the CO position is presented. The decrease of the tunneling current by CO adsorption is analyzed in detail, and a simplified tight-binding model is developed to illustrate the decrease of the electronic transmission spectra by over-coupling.

3.3.1 Calculation of the Cu(111) surface band structure

The DFT-PBE band structure of a Cu(111) slab near the Fermi level is shown in Figure (3.1). The surface state bands are indicated by bold lines. The band structure and dispersion are similar to band structures reported in the literature [8]. The binding energy of the surface state

at the Γ-point, about 0.6 eV, is slightly stronger than experimental values [7]. Near the Fermi level, the band structure of Cu(111) is dominated by dispersive 4sp-bands. The Cu 3d-bands are located between 2 and 3 eV below the Fermi level, and are not shown in Figure (3.1). Because the 3d-bands are rather localized, typical of transition metal d-bands, they contribute only modestly to the tunneling current, as verified by decomposing the tunneling current into its orbital contributions. Near the Γ-point, the surface band is dominated by Cu $4p_z$ orbitals. Though the Cu 4s orbitals contribute about 10% to the surface state (Figure 3.3a), they contribute less to the tunneling current because of their reduced extension into the vacuum. Note that the Cu $4p_z$ derived surface states are symmetrically well prepared to interact with the CO 5σ molecular orbital.

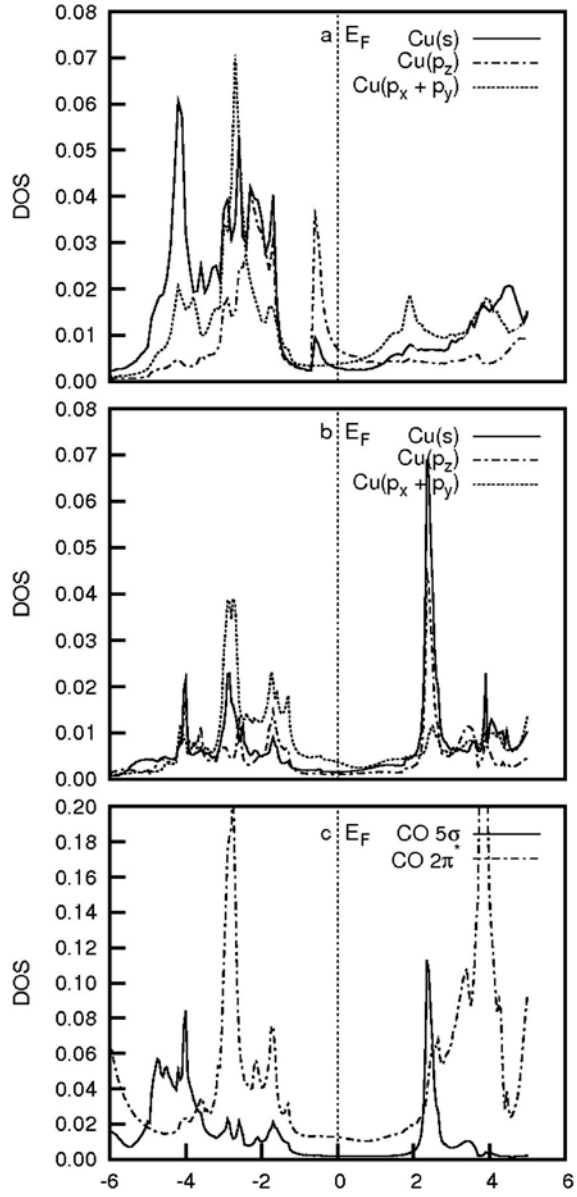

Figure 3.3 (a) Density of states projected on the surface atoms for clean Cu(111). (b) Upon CO adsorption, the Cu states near the Fermi level (mostly $4p_z$) interact with the CO states, depleting the density of states near the Fermi level. (c) CO adsorption also leads to broadening of the CO levels.

Figure 3.1 also shows the k-resolved projection of the surface state calculated within the EHMO framework (dotted lines). The good agreement between the DFT-PBE and the EHMO dispersion for the surface band near the Γ-point provides a validation of the fitted parameters. It is interesting to note that the binding energy of the EHMO surface band at the Γ-point,

0.4 eV below the Fermi energy, is closer to the experimental value than the DFT value. The states found near the K point of the Brillouin zone within the EHMO framework correspond to $4p_x$ and $4p_y$ surface orbitals. They contribute little to the electronic transmission spectrum, $T(E)$, of the junction. The optimized values of the on-site energies (Table 3.1, Supporting Information) indicate a significantly weaker on-site energy for the orbitals of the Cu surface atoms, and correlate well with the coordination number and the local potential environment. Indeed, the orbitals of the bulk atoms are subject to the full lattice crystal potential and hence more tightly bound.

3.3.2. CO adsorption on Cu(111) and corresponding STM image

The calculated $T(E)$ spectra, the constant current STM image, and the geometry used in the STM image calculations are shown in Figure 3.2. In the calculations, CO appears as a 0.4 Å depression with a radius of approximately 4 Å. Outside this radius the effect of CO on the tunnel junction conductance is small. Indeed, the tunneling current increases by an order of magnitude 5 Å from the center of the CO molecule and becomes comparable to the value for the clean Cu(111) surface. Experimental constant current STM images obtained at similar conditions (bias voltage of 40 mV and conductance of 1 nA) show dark, low current intensity spots with a depth of about 0.4 Å [3].

The STM $T(E)$ spectrum for clean Cu(111) is characterized by a peak 0.6 eV below the Fermi level at the location of the surface state. The surface states consist mainly of Cu $4p_z$ orbitals which facilitates overlap with the tip states. This enhanced overlap results in the peak at the location of the surface state. After adsorption of CO the peak disappears. The strong

interaction of the $4p_z$ surface states with the CO 5σ states moves the surface states away from the Fermi energy as is seen in Figure 3.3. The higher $T(E)$ values at around −1 eV below the Fermi level result from the higher density of broadened states of CO and Cu states in this region. It is clear from a comparison between the $T(E)$ and LDOS curves in Figure 3.3 that the $T(E)$ spectrum does not simply follow the LDOS. This confirms the importance of taking into account the full scattering matrix of tip–adsorbate–substrate tunnel junction to described the tunneling process and not only the LDOS.

To further understand the origin of the contrast inversion upon CO adsorption, it is useful to recognize that the tunneling current results from two contributions: the electronic coupling between the tip, the surface and the molecular orbitals of adsorbed CO, and the surface DOS. Introduction of a CO in the tunneling junction opens up an additional path for electron tunneling near the Fermi level and hence enhances the effective electronic coupling between the surface and the STM tip. However, the strong interaction of the CO 5σ orbital with the surface state reduces the surface DOS, thereby decreasing the tunneling current. The depletion of the DOS near the Fermi level by CO adsorption is clearly illustrated by the projected DOS for the Cu(111) surface with and without adsorbed CO (Figure 3.3). For the clean surface, the DOS projected on the surface Cu atoms shows a sharp peak about 0.5 eV below the Fermi level, corresponding to the surface state. The surface state is dominated by Cu $4p_z$ orbitals, with a minor contribution from the 4s orbitals. Near the Fermi level, the DOS projected on the surface atoms consists mainly of the surface state, with small contributions from bulk states. Upon CO adsorption, the DOS projected on the surface Cu atom where CO adsorbs changes dramatically (Figure 3.3b). The interaction between the CO 5σ molecular orbital at 3.2 eV below the Fermi level and the Cu surface state creates bonding and

antibonding states about 4 eV below and 2.5 eV above the Fermi level, as evident from a comparison of the DOS projected on the CO molecular orbitals (Figure 3.3c) and on the Cu surface orbitals (Figure 3.3b). The interaction with the CO 5σ orbital hence quenches electron density associated with the surface state near the Fermi energy. Interestingly, the position of the resonance resulting from the antibonding interaction between the CO 5σ orbital and the surface state about 2.3 eV above the Fermi level has been observed in the experimental d*I*/d*V* STM spectrum [25]. The CO 2π* orbital at 2.8 eV above the Cu(111) Fermi energy also interacts with the surface states, and states resulting from the bonding interaction with the Cu $4p_x$ and $4p_y$ orbitals can be found about 2 eV below the Fermi level. Near the Fermi level, the majority of the DOS can be attributed to the tail of the CO 2π* lowest unoccupied orbital.

To summarize, the interaction between the CO 5σ molecular orbital and the Cu(111) surface state dominated by Cu $4p_z$ orbitals creates bonding and antibonding interactions and pushes the surface states away from the Fermi level. This decreases the tunneling current where CO adsorbs and leads to STM contrast inversion. In the next section, we will further illustrate this over-coupling phenomenon with a tight-binding model.

3.3.3 Simple tight-binding model

The effect of the interaction of the CO 5σ molecular orbital with the Cu(111) surface state on the tunneling current can be further illustrated with a 1-dimensional tight-binding model (Figure 3.4a). In this model, the STM tip and the surface reservoirs are modeled as semi-infinite, one-dimensional chains of energy levels ε, where ε is taken at the binding energy of the bulk 4s orbitals, −10.6 eV. The interaction of the STM tip with the surface state is

described by the tunneling integral γ, and was optimized to reproduce the electronic transmission spectra at the Fermi energy, $\log(T(E_F)) = -2.25$, for a tip to surface distance of 7 Å. A metal–metal coupling η of 1.0 eV was used to ensure a sufficiently broad bulk band. The CO 5σ orbital at −13.25 eV interacts with the surface through the coupling α, and with the STM tip through β. The interaction of the 5σ level with the tip, β, should be weaker than the interaction of the Cu surface orbital with the STM tip, γ, because of the smaller size of the O $2p_z$ orbital and because the CO 5σ orbital is predominantly localized on the C atom. At the Fermi energy, $E = -10.7$ eV, $T(E)$ was calculated using the scattering matrix technique [12]. Figure 3.4b shows the effect of introducing the CO 5σ level on the electronic transmission spectra of the junction as a function of its coupling with the surface state, α.

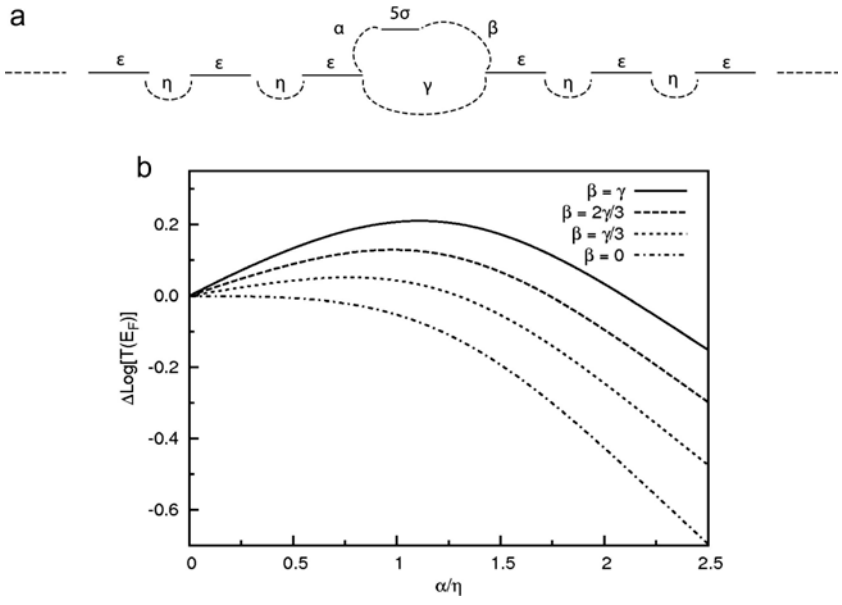

Figure 3.4. (a) Tight-binding model for CO adsorption on Cu(111). (b) Effect of introducing a CO molecule on the electronic transparency of the junction, $\Delta\log[T(E_F)]$, as a function of the coupling between the surface state and the CO 5σ orbital, α and between the CO 5σ orbital and the STM tip, β. The CO 5σ orbital on-site energy = −13.25 eV, the Cu surface state energy $\varepsilon = -10.6$ eV, the Cu metal to metal coupling $\eta = 1.00$ eV, and the through space coupling between the surface and the STM tip $\gamma = 0.019$ eV.

The conductance of the tip–CO–surface tunneling junction, $T(E)$, and hence the tunneling current are determined by the effective coupling between the reservoirs and by the surface DOS [12]. If the 5σ level is coupled weakly to the surface ($\alpha/\eta < 1.5$) and to the tip, then adding CO to the junction increases its electronic transmission. In this case, CO enhances the effective coupling between the two reservoirs. If the CO 5σ level is not coupled to the tip ($\beta = 0$), introducing CO in the junction does not affect the surface to tip coupling. However, the interaction between the 5σ level and the surface state significantly reduces the tunneling probability through the junction by reducing the surface DOS. Indeed, coupling the 5σ level to the surface level ε, shifts the surface level in energy, reduces the surface DOS near the Fermi level, and hence reduces the tunneling current. For intermediate coupling between the CO 5σ level and the tip, adding the 5σ level to the junction can either increase or decrease the electronic transmission. Strong coupling (over-coupling) between the 5σ level and the surface (large α/η) always decreases the electronic transmission. This corresponds to CO adsorption on Cu(111) where the CO 5σ molecular orbital interacts strongly with the $4p_z$ surface states. The surface to orbital coupling required to reduce the electronic transmission depends on the ratio between the tip to molecule coupling β, and the tip to surface coupling γ. Stronger tip–molecule couplings (larger β/γ) require a stronger molecule–surface coupling (α/γ) to reduce the electronic transmission.

The tight-binding model provides a phenomenological description of the decrease in tunneling current observed upon CO adsorption on Cu(111). The strong interaction between the CO 5σ orbital and the surface state depletes electronic density at Fermi level. The increase in effective coupling between the reservoirs by introduction of the extra CO 5σ level

is not able to compensate for the depletion of electron density. Although transmission can still occur through the tails of the broadened states, it is not comparable to the current through the original unperturbed surface state.

3.4 Conclusions

The contrast in STM images results from a complex interplay between the adsorbate and the surface electronic structure, as well as from the electronic interaction of the STM tip with the substrate via the adsorbate. Using electron scattering calculations, the origin of the reduction in the tunneling current upon adsorption of CO on Cu(111) is attributed to the strong interaction of the CO 5σ highest occupied molecular orbital with the Cu(111) surface state dominated by Cu $4p_z$ orbitals. As illustrated with a tight-binding model, such over-coupling reduces the surface density of states near the Fermi level and decreases the tunneling current at the sites where CO is adsorbed. The strong coupling is facilitated by the spatial extent, the symmetry and the energy of the surface band in Cu(111). An accurate description of the surface electronic structure was shown to describe this effect. Thus to study a STM junction involving sp bonded metal as substrate under EHT, it is of utmost importance that they be re-parameterized to reproduce the surface states. As, in sp bonded metals the free electron like surface states which are quite close to the Fermi level appear upon creation of the surface. Because of their proximity to the Fermi level these states are able to influence the IV characteristic in a drastic way.

Additionally the study shows that the STM image does not always reproduces the topology of the system. Hence, quantum mechanical image calculation becomes vital to truly understand the interaction that lead to STM image formation.

The work on this counter-intuitive observation underlines the importance of simulation to understand the IV characteristics for nano-scale devices. First, it shows that during the creation of devices unexpected localized states, i.e. surface states, edge states, might appear. These states might affect the device characteristics in an unexpected way. Additionally, the device components might interact with each other in an unforeseen way leading to further complication in the IV characteristics. Thus to truly understand the nano-scale device characteristics simulations become extremely important.

Table 3.1 Extended Huckel molecular orbital theory parameters used in this study.

	On-site energy	ζ_1	c_1	$\zeta_2{}^a$	$c_2{}^a$
STM tip atom					
4s	-10.56	1.70	0.56	0.85	0.05
Surface Cu					
4s	-10.12	1.70	0.61		
4p	-6.15	1.35	0.64		
3d	-12.44	1.80	0.32	5.13	0.83
Subsurface Cu					
4s	-10.61	1.70	0.61		
4p	-6.90	1.35	0.64		
3d	-12.93	1.80	0.32	5.13	0.83
Sub Subsurface Cu					
4s	-10.61	1.70	0.61		
4p	-6.89	1.35	0.64		
3d	-12.92	1.80	0.32	5.13	0.83
Bulk fcc Cu					
4s	-10.56	1.70	0.61		
4p	-6.78	1.34	0.65		
3d	-12.87	1.85	0.37	6.77	0.84
C					
2s	-21.40	1.63	1.00		
2p	-11.40	1.63	1.00		
O					
2s	-32.30	2.28	1.00		

2p	-14.80	2.28	1.00

[a]For the Cu 4s and 4p orbitals, a very good fit to the DFT DOS can be obtained by fixing ζ_2 to values greater than 20. Such a high orbital exponent leads to a negligible overlap with neighboring atoms and the corresponding orbitals were not explicitly used in the calculations. However, they lead to c_1 values less than unity [15].

References

[1] H.J. Guntherodt and R. Wiesendanger, Editors, *Scanning Tunneling Microscopy I: General Principles and Applications to Clean and Absorbate-Covered Surfaces,* Springer, New York (1992).

[2] P. Sautet and C. Joachim, *Chem. Phys. Lett.* **185,** 23 (1991).

[3] L. Bartels, G. Meyer and K.-H. Rieder, *Appl. Phys. Lett.* **71,** 213 (1997),

[4] J.A. Nieminen, E. Niemi and K.-H. Rieder, *Surf. Sci. Lett.* **552,** L47 (2004).

[5] D. Drakova, M. Nedjalkova and G. Doyen, *Int. J. Quant. Chem.* **106,** 1419 (2006).

[6] M.-L. Bocquet and P. Sautet, *Surf. Sci.* **360,** 128 (1996).

[7] F. Baumberger, T. Greber and J. Osterwalder, *Phys. Rev. B* **64,** 195411 (2001).

[8] G. Hörmandinger, *Phys. Rev. B* **49,** 13897 (1994).

[9] M.F. Crommie, C.P. Lutz and D.M. Eigler, *Nature* **363,** 524 (1993).

[10] F. Baumberger, T. Greber, B. Delley and J. Osterwalder, *Phys. Rev. Lett.* **88,** 237601 (2002).

[11] P. Heimann, H. Neddermeyer and H.F. Roloff, *J. Phys. C* **10,** L17 (1997).

[12] P. Sautet and C. Joachim, *Phys. Rev. B* **38,** 12238 (1988).

[13] R. Landauer, *Phil. Mag.* **21,** 863 (1970).

[14] R. Hoffman, *Rev. Mod. Phys.* **60,** 601 (1998).

[15] J. Cerdá and F. Soria, *Phys. Rev. B* **61,** 7965 (2000).

[16] A. Altibelli, C. Joachim and P. Sautet, *Surf. Sci.* **367,** 209 (1996).

[17] ‘‘Electron Work Function of The Elements”, in: David R. Lide (Ed.), CRC Handbook of Chemistry and Physics, eighty ninth ed. (Internet Version 2009), CRC Press/Taylor and Francis, Boca Raton, FL.

[18] J. Cerda, M.A. Van Hove, P. Sautet and M. Salmeron, *Phys. Rev. B* **56,** 15885 (1997).

[19] J. Perdew, K. Burke and M. Ernzerhof, *Phys. Rev. Lett.* **77,** 3865 (1996).

[20] G. Kresse and J. Furthmüller, *Comput. Mat. Sci.* **6,** 15 (1996).

[21] G. Kresse and J. Furthmüller, *Phys. Rev. B* **54,** 11169 (1996).

[22] P.E. Blochl, *Phys. Rev. B* **50,** 17953 (1994).

[23] G. Kresse and D. Joubert, *Phys. Rev. B* **59,** 1758 (1999).

[24] M. Neef and K. Doll, *Surf. Sci.* **600,** 1085 (2006).

[25] L. Bartels, G. Meyer and K.-H. Rieder, *Chem. Phys. Lett.* **297,** 287 (1998).

[26] L. J. Lauhon and W. Ho *Phys. Rev. B* **60**, R8525 (1999)

CHAPTER 4

Surface reconstruction of MoS_2 to Mo_2S_3

4.1 Introduction

The trend towards smaller and faster electronic devices requires the size of microelectronic circuits to ultimately reach the scale of atoms or molecules [1]. Using the elastic-scattering quantum chemistry technique, we have recently shown that if a surface atomic wire is fabricated by extracting a line of S surface atoms from the surface of lamellar MoS_2 [2], this will create sufficient electronic states in the MoS_2 surface band gap for this atomic wire to have a large conductance [3].

To quantify the stability of the MoS_2 surface which will be supporting the atomic wire fabrication by vertical single atom manipulation, crystalline MoS_2 was flashed to temperatures up to 1300 K. Up to 1200 K, very limited S vacancies were formed and the MoS_2 surface stayed atomically perfect (Figure 4.1). Above 1300 K, a major reconstruction of the MoS_2 surface was observed, creating mesoscale islands (Figure 4.1b). At temperatures above about 950 K, the bulk Mo–S phase diagram [4] indicates that bulk MoS_2 can reconstruct to the Mo_2S_3 phase. To form Mo_2S_3 from MoS_2, 1S atom has to be removed per Mo_2S_4 unit. Since the specific density of Mo_2S_3, 5.8 [5], is higher than the specific density of MoS_2, 5.0 [5], a contraction of the structure is expected. The transport of S atoms from the MoS_2 bulk is likely to be kinetically limited. Indeed, XRD studies of the sample after flashing confirm that the bulk of the sample is still MoS_2.

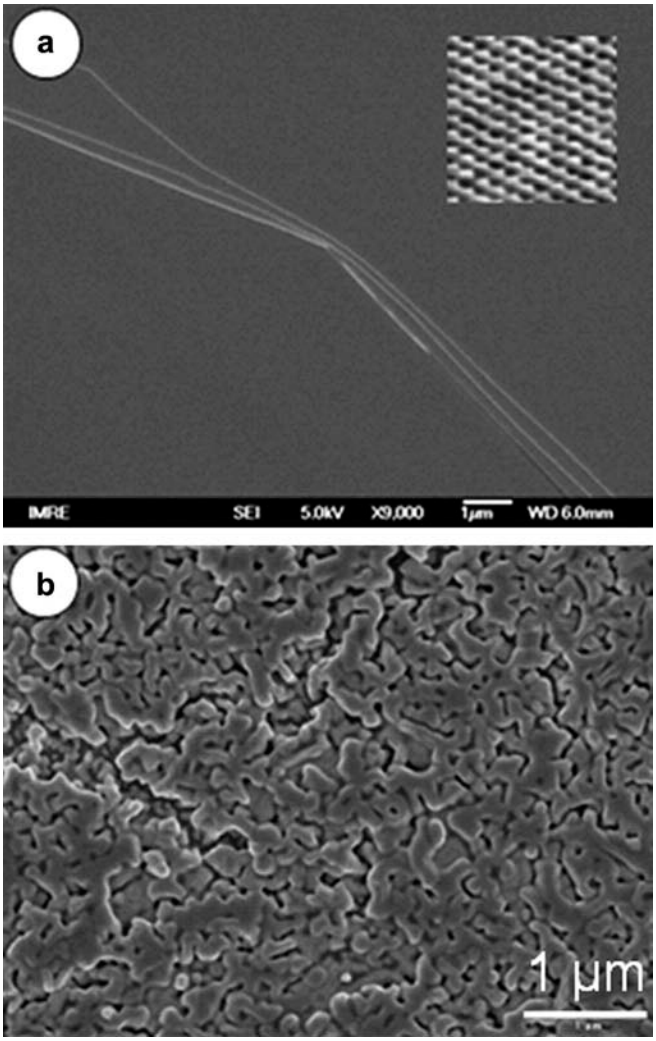

Figure 4.1: (a) SEM image of the MoS_2 surface. Micrometer scale, atomically flat terraces are separated by mono- or multi-steps. The atomic resolution STM image (inset) displays the hexagonal surface structure of MoS_2(0 0 1)-(1 × 1). (b) SEM image of the MoS_2 sample after flashing at 1300 K. Flat, mesoscale islands appear.

Though the bulk structure of Mo_2S_3 has been relatively well studied [6], [7] and [8], to our knowledge, its surface structure has not been reported. In this work, we present a combined theoretical and experimental investigation of the Mo_2S_3 surface structure, obtained after phase transformation of MoS_2 to Mo_2S_3. The experimental work was performed using ultra high vacuum scanning tunneling microscopy (UHV-STM). To elucidate the surface structure, theoretical thermodynamic calculations were used to identify stable surface structures, while

STM images were calculated using the elastic scattering quantum chemistry (ESQC) [9] approach to corroborate the experimental findings.

4.2. Experimental and computational methods

4.2.1. Experimental methods

Experiments were carried out in an Omicron multi-probe UHV-STM system with a base pressure better than 2×10^{-8} Pa. The UHV-STM is equipped with an analysis chamber and a sample preparation chamber, separated by a gate valve. Crystalline MoS_2 wafers cut from natural molybdenite were used as the initial sample. A freshly cleaved sample was first introduced into the UHV chamber. STM imaging confirmed the surface structure of the S-terminated MoS_2(0 0 1) surface, showing an atomic 1 × 1 surface structure (Figure 4.1a inset). After overnight degassing at 358 K, the sample was flashed to temperatures up to 1300 K for 5–12 s. The flashing cycles were repeated three times before SEM and STM images were collected. During flashing, the vacuum in the chamber remains below 6×10^{-6} Pa. Then, a new STM image of the sample was collected (Figure 4.2c and d). Some samples were transferred to a scanning electron microscope (SEM) to have a larger view of the surface corrugation changes after the flashing procedure. The large scale changes in the surface structure are evident in Figures 4.1b and 4.2a.

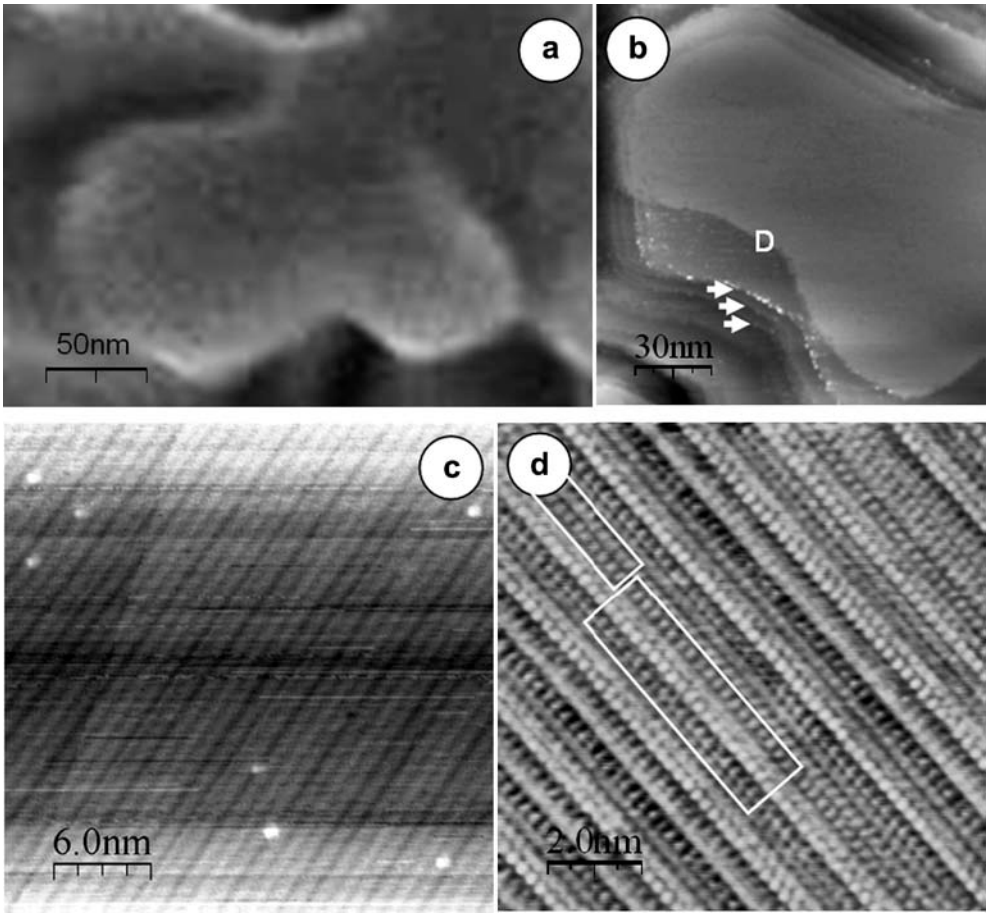

Figure 4.2: (a) SEM image of a single island after flashing to about 1300 k. (b) STM image of a single island. Steps of 1.2 nm height (D) and of 0.6 nm height (arrows) were observed. The island surface is atomically flat. (c) STM image of the surface of the island, illustrating the long range periodicity. The nature of the defects is unknown. (d) Atomic resolution image of the same sample, showing individual atoms. The rectangular boxes indicate the two types of atomic pair rows, zig-zag and rectangular. STM images were recorded at V = −0.4 V and I = 0.2 nA.

4.2.2 Computational methods

To identify thermodynamically stable surface structures for Mo_2S_3, the ab initio thermodynamics procedure was followed [10]. This procedure allows comparing surface energies for two-component crystals such as Mo_2S_3 with many possible surface structures. Ab initio thermodynamics has previously been applied to determine the surface termination of corundum-type metal–oxide structures in equilibrium with an O_2 environment [11] and

[12]. In this method, the surface free energy of a Mo_2S_3 slab, Mo_nS_m, in equilibrium with bulk Mo_2S_3 and an S_2 environment is given by

$$\gamma = \frac{1}{2A}\left[G_{Mo_nS_m} + (3n/4 - m/2)G_{S_2} - \frac{n}{2}G_{Mo_2S_3}\right] \qquad 4.1$$

where $G_{Mo_nS_m}$ is the Gibbs free energy of a slab with surface area A, $G_{Mo_2S_3}$ and G_{S_2} are the Gibbs free energies of bulk Mo_2S_3 and S_2, respectively. Note that the top and bottom surface of the slab need to be identical to obtain a meaningful definition for the surface free energy. This leads to non-stoichiometric slabs, Mo_nS_m (Figure 4.3). Eq. (4.1) can also be viewed as an expression of the free energy of reaction to create a Mo_nS_m slab from bulk Mo_2S_3. S_2 act as a S reservoir and is added or removed to close the mass balance. If the slabs are sufficiently thick, the surface energies of the top and bottom surface are additive. A number of simple checks, using stoichiometric slabs with a different top and bottom surface, confirmed that surface energies calculated following both approaches differ by less than 0.02 J/m^2 when the slab is at least 0.8 nm thick.

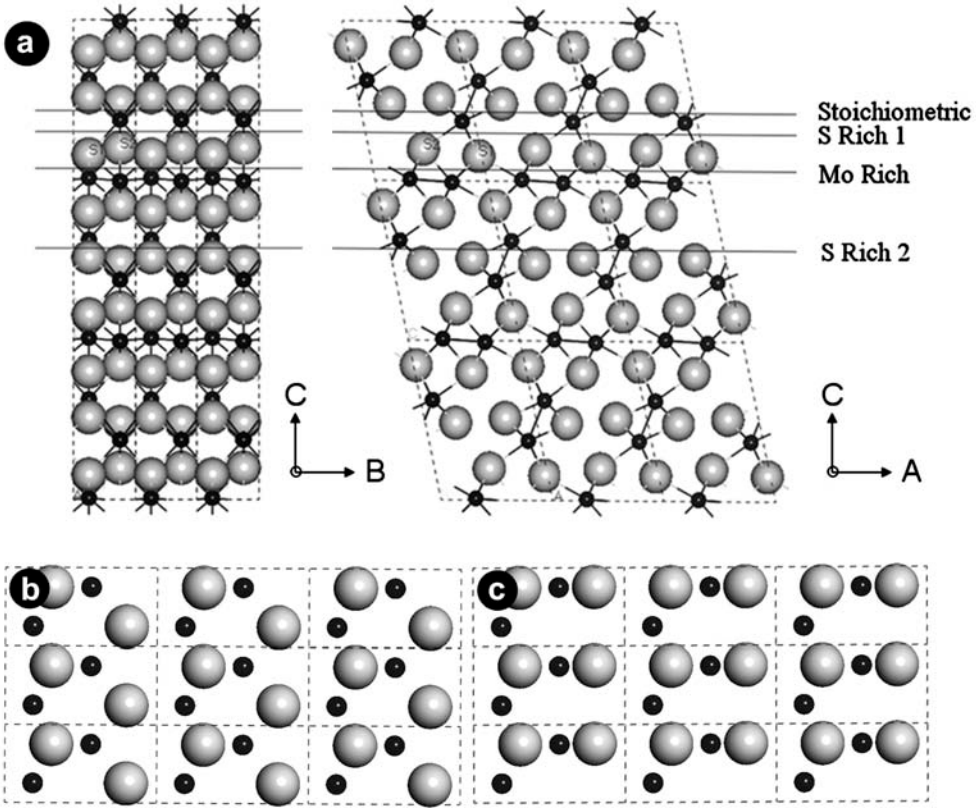

Figure 4.3: (a) Mo_2S_3 bulk crystal structure [22]. Large grey spheres indicate S atoms, while small black spheres indicate Mo. The crystal lattice parameters for the primitive monoclinic cell are: a = 6.09 Å; b = 3.20 Å; c = 8.62 Å and β = 102.4°. Selected (0 0 1) surface structures are illustrated. For the S-Rich1 surface two types of surface S atoms are indicated. (b) Top view for the S-Rich1 surface. (c) Rearrangement of the surface sulfur atoms leading to a rectangular pattern.

The energies in Eq. (1) were obtained from first principles periodic density functional (DFT) calculations. They were performed using the Perdew–Burke–Enzerhoff (PBE) functional [13], plane augmented wave pseudopotentials, and a (6 × 6 × 1) Monkhorst–Pack k-point grid for slabs and a (6 × 6 × 6) k-point grid for the bulk, as implemented in the Vienna ab initio Simulation Package (VASP) [14]. Repeated slabs were separated by a 10–12 Å vacuum layer and all the atomic positions were fully relaxed. The Gibbs free energies of bulk Mo_2S_3 and Mo_nS_m slabs in (1) were replaced by the total electronic energy, neglecting relative entropic and PV contributions. The chemical potential of gas phase S_2 was obtained by combining the

electronic energy with experimental temperature and pressure corrections [15]. To validate these assumptions, the Gibbs free energy of reaction for

$$Mo + S_2 \Leftrightarrow MoS_2 \qquad 4.2$$

And

$$2MoS_2 \Leftrightarrow Mo_2S_3 + \frac{1}{2}\, S_2 \qquad 4.3$$

were calculated at 300 K and 1 atm. The calculated Gibbs free energies of reaction, −296 kJ/mol and +180 kJ/mol for the reactions (4.2) and (4.3), respectively, match the experimental values of −294 kJ/mol and +178 kJ/mol [16] quite well.

There are various ways to cleave bulk Mo_2S_3. With lattice vectors a and b of 6.08 Å and 3.20 Å, only the (0 0 1) surfaces are consistent with the periodicity of the STM images (Figure 4.2). Starting from the bulk crystal structure, 10 possible surface terminations were considered for the Mo_2S_3(0 0 1) surface. Selected surfaces are indicated in Figure 4.3. Additional surface structures, illustrated in Figure 4.3, were considered to explain some details of the STM images.

STM images were calculated using the Elastic Scattering Quantum Chemistry (ESQC) approach. In this approach, the full scattering matrix for the tip-substrate junction is constructed to calculate the transmission amplitude of the junction. The tunneling current is then obtained from the Landauer formula [17]:

$$I(V) = \frac{e}{h}\int_{-\infty}^{+\infty} T(E)\big[f_0(E-(E_F-eV/2)\big) - f_0\big(E-(E_F+eV/2)\big)dE \qquad 4.4$$

which for low bias simplifies to

$$I = \frac{2e^2}{h}\,T(E_F)V \qquad 4.5$$

where f_0 is the Fermi function, E_F is the Fermi energy and V is the bias voltage.

The atomic details of the Mo_2S_3 surface and of the tip, as well as their electronic interactions are fully taken into account using a minimal linear combination of atomic orbitals representation. Our approach follows the procedure outlined by Altibelli et al. [18] for MoS_2. Within the calculations, the virtual STM is modeled as two semi-infinite W metal pads, while a 12 Å thick Mo_2S_3 slab and a four atom W tip constitute the junction. Each part of the system, i.e. the W bulk, the Mo_2S_3 slab and the STM tip, is described atom by atom. The distance between the Mo_2S_3 slab and the semi-infinite W metal pad is 2.2 Å. Bloch states propagating in the semi-infinite W contacts define the incoming and scattered states used to calculate the electronic transparency $T(E_F)$ of the junction. Though the calculated current intensity depends on the details of the model, for a constant current scan, the corrugation does not depend on the details of the W metal pad–Mo_2S_3 slab–STM tip–W metal pad junction for typical tip-surface distances of 4–6 Å. Because of the size of the system, ab initio constant current STM image calculations become impractical and the extended Hückel molecular orbital (EHMO) [19] model was used to construct the electronic Hamiltonian of the corresponding tunnel junction. Standard Hückel parameters [20] were used in the calculations. To help elucidate the contrast in the simulated STM images, the density of states (DOS) of Mo_2S_3 was calculated using Bicon–Cedit [21]. For the DOS calculation, we used a

5X5X5 k-point grid. Standard EHMO parameters were also used in these calculations, preserving consistency with the ESQC results. The band structure and DOS were also calculated using periodic DFT to validate the EHMO results.

4.3 Experimental STM images of the MoS_2(0 0 1) and Mo_2S_3 surfaces

SEM images of a freshly cleaved MoS_2 surface show atomically flat terraces of over 100 μm diameter, separated by multi- and mono-layer steps (Figure 4.1a). Atomic resolution STM images of the higher and lower terraces (inset in Figure 4.1a) show the hexagonal MoS_2(0 0 1)-(1 × 1) structure without lattice distortions. The atomic resolution image of the MoS_2 surface has been studied before and our image is consistent with those data. A theoretical study by Altibelli et al. [15] showed that the image can be explained by a competition between through bond and through space electronic coupling between the tip apex end atom and the S and Mo orbitals contributions.

Both the large scale surface morphology of the flat terraces and the atomic hexagonal surface structure on those terraces are preserved when the sample is annealed at temperatures up to 1100 K. The Mo–S phase diagram reported by Brewer and Lamoreaux [4] indicates that bulk Mo_2S_3 becomes thermodynamically favorable over the MoS_2 phase above about 950 K. For a phase transformation to occur, one S atom has to be removed for every two MoS_2 units. The transport of S atoms is likely to be kinetically limited, especially from the MoS_2 bulk, and higher temperatures are required in this case. When flashing the MoS_2 sample to about 1300 K, both the overall surface morphology and its local surface atomic structure change dramatically (Figure 4.1b).

SEM images of the sample flashed to 1300 K show islands of about 150 nm diameter (Figures. 4.1b and 4.2a). Figure 4.2b presents a STM image of one of those islands indicating that a given island has atomically flat terraces. The STM scan recorded at the surface of those islands (Figure 4.2c) shows rows with a periodicity of about 0.6 nm, as well as atomic defects. Atomic resolution STM images (Figure 4.2d) indicate that the rows correspond to atomic pairs with a periodicity of 0.32 nm along the rows. Two types of rows of atomic pairs are observed with an average periodicity of about 0.62 nm. The observed periodicity matches fairly well with the lattice vectors of the Mo_2S_3(0 0 1) surface structure, with a = 0.61 nm, b = 0.32 nm and the angle $\alpha = 90°$ [22]. X-ray diffraction (XRD) [6] and transmission electron microscope (TEM) [7] studies indicate that the Mo_2S_3 crystal structure is monoclinic with 10 atoms per unit cell (Figure 4.3). The Mo atoms are arranged in two inequivalent zig-zag chains along the b-axis. One Mo atom covalently binds six S atoms and another Mo atom.

We propose that the observed surface termination after a high temperature treatment in the UHV is indeed the (0 0 1) facet of a Mo_2S_3(0 0 1) crystal surface. First principles calculations discussed below confirm that the (0 0 1) surface energy is indeed lower than the surface energy for other low Miller index surfaces of this material. A closer look at the STM images allows distinguishing two types of atomic pair rows, a dominant type with a zig-zag organization along the rows and a type with a rectangular pattern. Both are indicated in Figure 4.2d.

4.4. Theoretical study of the Mo_2S_3 surface structure

4.4.1. Surface energy

Experimentally, the atomic surface structure of the MoS_2 terraces is preserved up to 1100 K. Above 1300 K, both the overall surface morphology and the local surface atomic structure change dramatically. The limited number of S vacancies observed on the MoS_2 terraces up to 1100 K is consistent with the high reaction energy to create S vacancies on MoS_2, with a calculated ΔG_r^0 of +240 kJ/mol S vacancies. In comparison, the standard reaction Gibbs free energy to transform MoS_2 to Mo_2S_3, Eq. (4.3), is +180 kJ/mol.

To elucidate the atomic composition of the surface structure observed in the STM images, surface free energies were calculated for a range of possible Mo_2S_3 surface chemical compositions. Since some of the possible surface terminations are non-stoichiometric, i.e. S-rich or Mo-rich, the surface energy depends on the S chemical potential (Eq. (4.1)), and the relative stability changes with the temperature and the S_2 partial pressure in the UHV chamber. Because the periodicity of the STM images indicate that the surface structure is related to the (0 0 1) facet, our calculations focused on all possible (0 0 1)-1 × 1 surface structure derived from the Mo_2S_3 bulk positions. Surface energies for selected surfaces are shown in Figure. 4.4, and illustrated in Figure. 4.3.

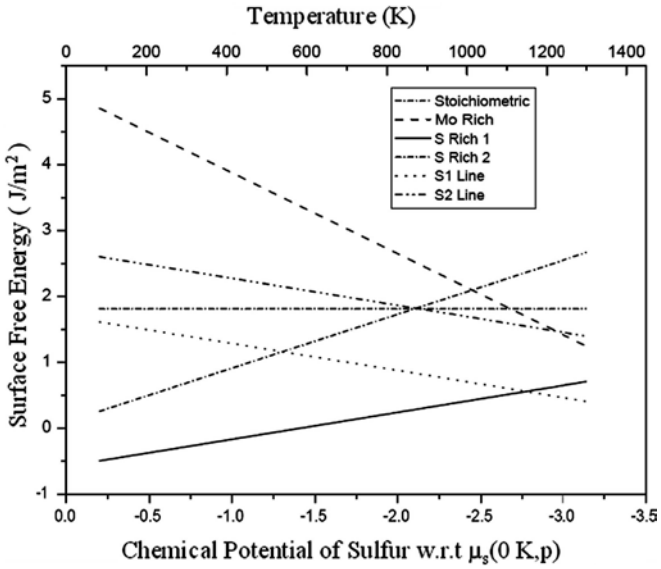

Figure 4.4: Surface free energy for selected Mo_2S_3(0 0 1) surface terminations (Figure 4.3 and Figure 4.5) as a function of the S chemical potential, μ_s(T, p). The corresponding temperature for $p_{S_2} = 3 \times 10^{-7}\ Pa$ is indicated. The chemical potential μ_s(T, p) is relative to the total electronic energy of an isolated S_2 molecule,$\mu_s(0\ K, p) = 1/2E_{S_2}^{total}$.

The calculations indicate that the S-rich1 surface, presented in Figure. 4.3 and Figure 4.5, has the lowest surface energy for S relative chemical potentials, where zero of the chemical potential has been taken to be the total electronic energy of an isolated S_2 molecule, up to −2.55 eV, or temperatures below 1100 K under UHV conditions, i.e. a S_2 partial pressure below 3×10^{-7} Pa. The S-rich surfaces become less stable as the S chemical potential decreases or, equivalently, as the temperature increases. Indeed, the effect of entropy of the gas phase S_2 increases with temperature, and the equilibrium reflected in (4.1) shifts towards the Mo-rich slabs. The slope of the surface energy vs. temperature relationship is determined by the stoichiometric coefficient of S_2 in Eq. (1) and the surface energy of stoichiometric slabs is independent of the S chemical potential. At temperatures above about 1500 K and under UHV conditions, the calculations indicate that a Mo-rich surface becomes thermodynamically favorable. However, at the experimental temperatures of around 1300 K,

the S-rich1 surface remains the most stable surface formed by cleaving Mo_2S_3. The relative stability of this surface originates from the rather low energy cost required to create it, and can be explained by the low number of bonds broken to create the S-rich1 surface from the Mo_2S_3 bulk. Indeed, only three Mo–S bonds are broken per unit cell to create this surface, as compared to six Mo–S bonds to create the Mo-rich surface (Figure 4.3). At high S chemical potentials and low temperatures, the surface energy for the S-rich1 surface even becomes negative, indicating that it is thermodynamically favorable to create this surface from the Mo_2S_3 bulk when the S chemical potential is high. Negative surface energies have been reported and discussed before for two-component systems and are not unexpected [23].

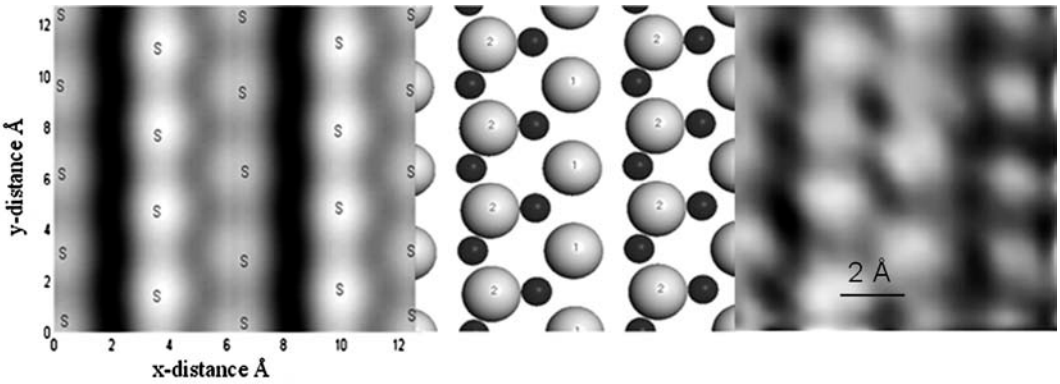

Figure 4.5: Simulated low voltage STM image for the S-rich1 surface (a) corresponding surface structure (b) and experimental STM image recorded at V = −0.4 V and I = 0.2 nA. (c) Two types of surface S atoms can be distinguished. In the ESQC simulations, the average tip height above the surface is approximately 4 Å and the Fermi energy for the S-rich1 surface is −9.9 eV.

The surface geometry of the S-rich1 surface is shown in Figure 4.5. The surface S atoms are consistent with the double row zig-zag pattern observed above in the experimental STM images. The spacing between the S atoms match the experimental spacing of 6.2 Å and 3.1 Å along two orthogonal directions. Note that the two S atoms, S1 and S2 in Figure 4.3 and Figure 4.5, are not equivalent and have a slightly different height. They are hence expected to

appear different in STM images. STM image calculations reported below indeed indicate that the S atoms are observed as protrusions for low voltages and for filled state STM images.

Near the experimental temperature of 1300 K, the stability of the S-rich1 surface and of the Mo-rich surface becomes fairly similar. Two additional surface structures, created by removing a row of S1 and a row of S2 atoms from the S-rich1 surface, were also considered (Figure 4.4). The surface energy calculations indicate that a surface formed by removing the S1 row will be formed at high temperatures. Rectangular arrangements of the surface S atoms can be considered as well (Figure 4.3c). However, the structure in Figure 4.3c does not correspond with the bulk location of the S atoms and is less stable than the structure in Figure 4.3b, probably because of repulsion between neighboring S atoms. Larger unit cells, considering combinations of zig-zag, missing S rows and rectangular patterns are needed to gain a full understanding of the possible surface structures, but are beyond the scope of the current work.

4.4.2. STM image calculations

ESQC was used to calculate constant current STM images for the S-rich1 surface (Figure 4.5). At low voltages and an average tip-surface distance of around 4 Å the distance between the tip atom and the topmost sulfur atom, the surface S atoms appear as protrusions and lead to a zig-zag pattern, separated by a dark grove. Note that both surface sulfur atoms have a different height in the image, with S2 appearing brighter than S1. The S2 atoms sit slightly higher on the surface than the S1 atoms, giving rise to a better overlap between the surface and the tip states. The difference in height between S1 and S2 is 0.35 Å while the STM tip

moves slightly at 0.14 Å, indicating that the STM image results from both geometric and electronic effects. The corrugation along and orthogonal to the rows agrees fairly well with the experimental corrugation. The STM image results from the variation of the interaction between the electronic tip states and the electronic surface states near the surface Fermi level. To elucidate those surface electronic states, the total density of states (DOS) and the DOS projected on the Mo and S orbitals was calculated for Mo_2S_3 (Figure 4.6).

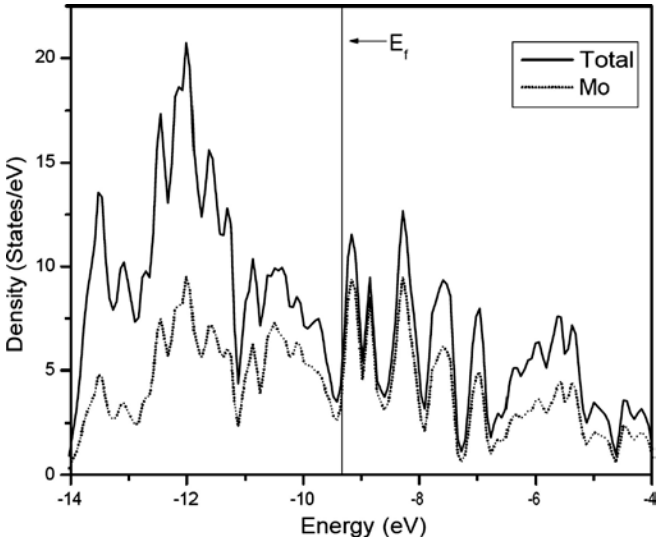

Figure 4.6: Total and projected density of states for bulk Mo_2S_3. The bulk Fermi level, −9.2 eV, is indicated. Note that the bulk Fermi level differs from the surface Fermi level.

The calculated DOS confirms the metallic nature of Mo_2S_3. The many peaks in the DOS plot results from the finite k-point sampling. It can be attributed to metal–metal binding between Mo atoms in Mo_2S_3. Indeed, the Mo–Mo distances of 2.80 Å and 2.81 Å are comparable to the distance in bcc Mo, 2.73 Å, and the states near the Fermi level are mainly attributed to Mo–Mo interactions. Following the procedure suggested by Hoffman [24], a DOS plot for the Mo sublattice of Mo_2S_3 indeed confirmed significant interactions between the Mo atoms. A similar procedure for MoS_2 does not show significant Mo–Mo interaction, as expected. The S atoms are involved in Mo–S bonds and the DOS is mainly localized below and well

above the Fermi level. The position of the bonding S states is somewhat similar to MoS_2 [3]. Since the states near the Fermi level are dominated by Mo d-orbitals of the Mo atoms, calculations based on the surface Fermi level states would predict the Mo atoms to appear bright. However, since the Mo d-orbitals have a shorter range than the S p-orbitals [25], the better overlap of the S orbitals with the STM tip states for typical tip-surface distances makes the S atoms appear bright. This overlap depends quite critical on the tip-surface distance, and an inversion of the calculated contrast can be observed for tip-surface distances below 2 Å. A similar observation was reported for the MoS_2 surface [18].

4.5. Conclusion

Under ultra high vacuum condition and at temperatures above 1300 K, a partial transformation of MoS_2 to Mo_2S_3 is observed and this reconstruction can be imaged using scanning tunneling microscopy (STM). A combination of first principles surface free energy calculations and STM image simulations indicates that the dominant surface structure of Mo_2S_3 is sulfur rich up to temperatures of 1400–1500 K, despite the low sulfur chemical potential at these conditions. The S atoms form extended double zig-zag rows separated by a dark grove, which are clearly observed with the STM. The STM images result from competition between the higher density of Mo states near the Fermi level, and the larger range and hence better overlap with the STM tip states for the p-orbitals of the surface S atoms.

References

[1] C. Joachim, J.K. Gimzewski and A. Aviram, *Nature* **408**, 541 (2000).

[2] S. Hosoki, S. Hosaka and T. Hasegawa, *Appl. Surf. Sci.* **60/61**, 643 (1992).

[3] K.S. Yong, D.M. Otalvaro, I. Duchemin, M. Saeys and C. Joachim, *Phys. Rev. B* 77, 205429 (2008).

[4] L. Brewer, R.H. Lamoreaux, *Atomic Energy Rev.*, Special issue No. 8, IAEA, Vienna, 1980.

[5] R.W.G. Wyckoff, *Crystal Structures*, Krieger Publishing Company (1984).

[6] F. Jellinek, *Nature* **192**, 1065 (1961).

[7] R.C. Che, M. Bai and L.M. Peng, *Appl. Phys. Lett.* **83**, 3561 (2003).

[8] R.L. Fagerquist and R.D. Kirby, *Phys. Rev. B* **38,** 3973 (1998).

[9] P. Sautet and C. Joachim, *Phys. Rev. B* **38**, 12238 (1988).

[10] K. Reuter and M. Scheffler, *Phys. Rev. B* **65,** 035406 (2001).

[11] X.G. Wang, W. Weiss, S.K. Shaikhutdinov, M. Ritter, M. Petersen, F. Wagner, R. Schlogl and M. Scheffler, *Phys. Rev. Lett.* **81,** 1038 (1998).

[12] X.G. Wang, A. Chaka and M. Scheffler, *Phys. Rev. Lett.* **84,** 3650 (2000).

[13] J.P. Perdew, K. Burke and M. Ernzerhof, *Phys. Rev. Lett.* **77**, 3865 (1996).

[14] G. Kresse and J. Hafner, Phys. Rev. B **47**, 558 (1993).

[15] D.R. Stull and H. Prophet, *JANAF Thermochemical Tables (second ed.)*, US National Bureau of Standards, Washington, DC (1971).

[16] D.R. Burgess, Thermochemical data, in: P.J. Linstrom, W.G. Mallard (Eds.), NIST Chemistry WebBook, NIST Standard Reference Database Number 69, National Institute of Standards and Technology, Gaithersburg, MD, 2005. Available from: <http://webbook.nist.gov.libproxy1.nus.edu.sg>.

[17] R. Landauer, *Philos. Mag.* **21**, 863 (1970).

[18] A. Altibelli, C. Joachim and P. Sautet, *Surf. Sci.* **367**, 209 (1996).

[19] R. Hoffmann, *J. Chem. Phys.* **39,** 1397 (1963).

[20] R.H. Summerville and R. Hoffmann, *J. Am. Chem. Soc.* **98**, 7240 (1976).

[21] M.H. Whangbo, M. Evain, T. Hughbanks, M. Kertesz, S. Wijeyesekera, C. Wilker, C. Zheng, R. Hoffmann, QCPE #571, Extended-Hückel Molecular, Crystal and Properties Package, QCPE, 1989.

[22] W.J. Schutte, Structures of Modulated Crystals, Ph.D. Thesis, University of Groningen, 1990.

[23] R.D. Meade and D. Vanderbilt, *Phys. Rev. Lett.* **63,** 1404 (1989).

[24] R. Hoffman, Solids and Surfaces: *A Chemist's View of Bonding in Extended Structures* vol. 61, VCH Publishers, NY (1998).

CHAPTER 5

Calculation of the spin dependent tunnelling current in Fe|MgO|Fe tunnel junctions

5.1 Introduction

In the previous chapters, current flow through STM tunnel junctions was studied. In this chapter, we extend the methodologies further to treat spin-dependent ballistic electron transport as encountered in Magnetic Tunnel Junctions (MTJs). MTJs not only provide a convenient route to enhance our understanding of the spin-dependent transport at nanoscale but also form a basic building block in many technological important devices such as random-access-memory (MRAM), magnetic sensors and novel programmable logic devices [1–3].

Earlier experimental studies of MTJs employed amorphous Al_2O_3 films as the barrier material due to the ease of fabrication. Amorphous barriers, as their name suggests, do not provide any spin filtering mechanism. In other words, electrons of either spin encounter similar resistance traversing it. This means we can understand the observed Tunneling Magneto-Resistance (TMR) ratios for such systems from the spin polarization of the electrons at interface, as proposed by Julliere [4]. The success of the Julliere model in qualitatively predicting the TMR values of MTJs with amorphous barriers, indeed, confirms the absence of spin filtering in amorphous barriers.

Recent advances in the epitaxial growth of the films make it possible to grow crystalline barrier materials. Various studies with crystalline barriers have clearly demonstrated that spin filtering properties of the barrier materials play a very important role in determining the TMR ratio [5]. In fact, Yang et al. reported that the sign of the TMR of a CoFe|MgO|CoFe MTJ can be inverted by introducing a thin layer of NiO in-between contact and the barrier material [6]. To understand the observed TMR ratio for such systems, it becomes vital to incorporate the spin filtering property of the barrier materials in the model. Fortunately, the crystalline nature of the barrier material makes rigorous transport calculation for the whole system possible as the transverse momentum($\vec{k}_{||}$) is conserved during the transport. Indeed, the prediction of very high TMR ratios for Fe|MgO|Fe trilayer structures from transport calculation [7,8] and its subsequent experimental verification [9,10] underline the importance of such transport calculations.

In this chapter, we benchmark our methodologies for the well-studied Fe|MgO|Fe system for which a wealth of theoretical as well as experimental data is available. In the next chapter we employ the methodologies developed here to study the effect of strain on the TMR ratio of a MTJ. In our study, we employ the semi-empirical extended Hückel theory (EHT) for the description of the Hamiltonian matrix, coupled with the non-equilibrium Green function formalism for the transport calculations, as implemented in the GREEN package [11]. For the construction of the Hamiltonian matrix our choice remains the EHT due to its numerous advantages as described in the previous chapters. As noted earlier, it combines the advantages of tight binding theory, i.e., its computationally efficiency, with the flexibility to optimize the parameters to provide a very accurate description of the electronic structure of the system. The non-orthogonality of the basis set, on the other hand, captures the bonding chemistry very well

and also ensures the transferability of the parameters across different environments and structures [12].

For the transport calculation, however, we have used the Green's function formalism as implemented in GREEN [11] instead of ESQC [13,14]. Both GREEN and ESQC model the system as a periodic system with an embedded defect. The main difference between the two methods is the way scattering matrix is calculated. In ESQC, the scattering matrix is calculated via the transfer matrix technique, which typically requires identical electrodes on both sides of the defect. In GREEN, the scattering matrix is obtained via the use of the Green's function that lifts the requirement of identical electrodes on both sides of the defect. Also in ESQC the real-space matrices are directly used while in GREEN they are back transformed into reciprocal space before the calculation [15].

Due to the lateral symmetry of the MTJs, reciprocal space calculations lead to faster convergence. Moreover, the IV curve is more easily interpreted in terms of the lateral momentum of the tunneling electrons. As the momentum of an electron is directly related to its reciprocal space wave-vector, reciprocal space calculations directly provide the information for the interpretations of the IV characteristics of the system.

Due to the difference in the way the matrix elements are calculated, the convergence criteria also become different. In the real space calculations, it is important to check the convergence of the

result with respect to the lateral dimension of the system. For the reciprocal space calculations this requirement changes to the convergence with respect to the k-point number used to sample the $\vec{k}_{||}$ Brillouin zone. In many transport calculations the presence of the sharp peaks in the transmission coefficient $\widetilde{\mathrm{T}}(\vec{\mathrm{k}}_{||})$ requires a fine k-point mesh in order not to miss contributions due to such peaks.

Another important factor that needs careful attention is the value of the imaginary part of the energy in the calculation of the Green function. The Green function, $G(E)$, of a system is given by

$$\mathrm{G(E)F(E)} = \mathrm{I}$$

Where I is an identity matrix and $\mathrm{F(E)}$ is the usual secular matrix

$$F(E) = ES - H$$

In the above equation, H and S are the Hamiltonian and the overlap matrix. In order to avoid divergence for certain energies, the value of E is taken to be complex by adding a small imaginary δ to the actual value of the real energy $\mathrm{E_r}$.

$$\mathrm{E} = \mathrm{E_r} + \mathrm{i}\delta$$

The presence of an imaginary energy, however, introduces damping of the Bloch waves [11]. In order to minimize energy losses due to damping, a very small value of the imaginary energy (typically 10^{-6} meV) is taken for the calculation of the Green function.

5.2 Methods

5.2.1 Model Geometry

Previous studies of Fe(001) deposited over the MgO(001) films suggest that Fe(001) grows epitaxially over the MgO(001) surface. Kanaji et al. [16] find that Fe(001) atoms are located on top of the O atoms of the MgO film. Using Low Energy Electron Diffraction (LEED) they estimate the Fe-O distance to be ~2 Å. Their finding is supported by full potential linearized augmented planewave (FLAPW) DFT studies by Li et al. [15]. They, too, find that Fe atoms are located directly above the O atoms of MgO. Their calculated Fe-O distance of 2.3 Å, however, is slightly longer than the experimental data. There is another theoretical study that models a MTJ structure exactly by considering MgO(001) layer sandwiched between two Fe(001) layers [7]. This study, too, finds that the Fe atoms are located directly above the O atoms. In this study, the authors find a Fe-O distance of 2.16 Å, intermediate between the previous values.

Based on the above studies, we modeled our system to be epitaxial with an in-plane lattice constant of the experimental Fe(001) value of 2.886 Å (Figure 5.1). In order to place the O atoms of MgO directly above the Fe atoms, the MgO(001) slab was rotated by 45 degrees with respect to the Fe lattice. An Fe-O distance of 2.16 Å was used as in ref [8].

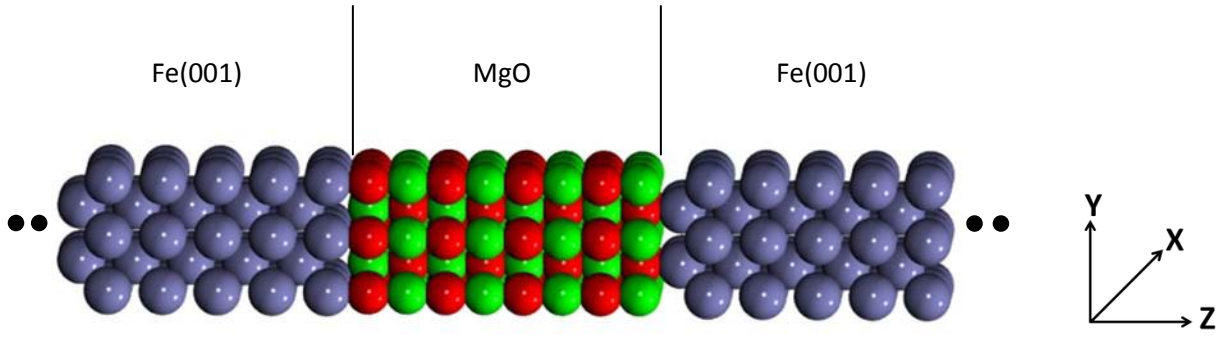

Figure 5.1: Arrangement of the atoms in a magnetic tunnel junction, consisting of Fe|MgO|Fe. The blue, red, and green balls represent Fe, O, and Mg atoms respectively. In the NEGF calculations, the Fe atoms extend to infinity at the both ends and the whole system is periodic in the direction parallel to the interface (xy).

5.2.2 Description of the theory

In the transport calculations, we used the EHT [18] for the description of the device Hamiltonian and the non-equilibrium Green function [19] to determine the transmission probability, as implemented in the GREEN program [11,20]. The elements of the EHT Hamiltonian matrices are determined by the following prescription. The diagonal elements $(H_d(ii))$ of the matrix are given by the ionization energies of the corresponding orbitals. The off-diagonal elements $(H_d(ij))$ are given by

$$\mathrm{H_d(ij)} = \frac{1}{2}\mathrm{KS_d[H_d(ii) + H_d(jj)]}$$

where $\mathrm{S_d(ij)}$ is the overlap integral given by $\langle \mathrm{i}|\mathrm{j}\rangle$ and K is a scaling constant. The device is considered to be perfectly periodic perpendicular to the transport direction. As a result, we can write the various matrice elements in reciprocal space from their real space counterparts as follows $(\mathrm{A} \equiv \mathrm{H_d}, \mathrm{S_d})$

$$A(\vec{k}_{||}) = \sum_{n} A_{mn} e^{i\vec{k}.(\vec{r}_m - \vec{r}_n)}$$

In the above equation, m represents the unit cell located at origin and n represents the neighboring unit cells in the transverse directions.

From the knowledge of Hamiltonian matrix $H_d(\vec{k}_{||})$ and overlap matrix $S_d(\vec{k}_{||})$ the Green function $G(E, \vec{k}_{||})$ at a given energy (E) and and transverse momentum $(\vec{k}_{||})$ is easily calculated from

$$G(E, \vec{k}_{||}) = [(E + i0^+)S_d(\vec{k}_{||}) - H_d(\vec{k}_{||}) - \Sigma_1(E, \vec{k}_{||}) - \Sigma_2(E, \vec{k}_{||})]$$

Where Σ_1 and Σ_2 are the self energies of the contact that describe the effect of the left and the right contact on the central device. The transmission coefficient $\tilde{T}(E, \vec{k}_{||})$ at a given energy E for a given transverse momentum $(\vec{k}_{||})$ is then calculated from the knowledge of the Green function as follows

$$\tilde{T}(E, \vec{k}_{||}) = tr(\Gamma_1 G \Gamma_2 G^{\dagger})$$

In the above equation Γ_1 and Γ_2 are the broadening functions, which are the non-hermitian part of the self-energy and are given by $\Gamma_{1,2} = i(\Sigma_{1,2} - \Sigma_{1,2}^{\dagger})$. The total transmission per unit area, T(E), is then calculated by integrating $\tilde{T}(E, \vec{k}_{||})$ over $\vec{k}_{||}$

$$T(E) = \frac{1}{4\pi^2} \int \tilde{T}(E, \vec{k}_{||}) d\vec{k}_{||}$$

This integral is calculated numerically by discretizing $\vec{k}_{||}$ as

$$T(E) \approx \frac{1}{A} \sum_{\vec{k}_{||}} \tilde{T}(E, \vec{k}_{||})$$

Once $T(E)$ is known, the current $J_{P,AP}$ for the parallel and the anti-parallel configuration can be calculated from the Landauer formula [21]

$$J_{P,AP} = \frac{e}{h} \int T_{P,AP}(E)[f_1(E - \mu_1) - f_2(E - \mu_2)]$$

Where f_1 and f_2 are the Fermi-Dirac distribution of the left and the right contact and μ_1 and μ_2 are their respective chemical potential.

5.2.3 Determination of the Extended Hückel parameters

The electronic structure of the tunneling junction is described by a Extended Hückel Molecular Orbital (EHMO) Hamiltonian, using literature values for the Fe *spd* parameters [12]. As the MgO parameters are not available in the literature, we optimized them by fitting the EHT bands to accurate bandstructures derived from DFT calculations. The fitting is carried out by minimizing the error function (χ) which is the difference between the EHT derived bands and the DFT derived bands.

$$\chi = \sum_{m,k,\sigma} \left(E^m(\vec{k}_{||}, \sigma) - E^m_{dft}(\vec{k}_{||}, \sigma) \right)^2$$

In the above expression $E^m(\vec{k}_{||}, \sigma)$ represents the energy of m^{th} band, with k-vector $\vec{k}_{||}$ and spin configuration σ. For the minimization of χ, we employed a Levenberg-Marquadt algorithm (LM), as implemented in GREEN [11,20].

Since DFT-GGA underestimates MgO bandgap, we first correct it by shifting the valence band as has been done in previous calculations [22]. The fitted parameters and the bandgap are given in Table 5.1. To confirm the accuracy of the fitted parameters, the EHT bandstructure is compared with the corrected DFT-PBE bandstructure in Figure 5.2. In the figure, the solid line represents the EHT bandstructure while the points represent the DFT bandstructure. In the plot, the bands have been shifted so that the top of the valence band coincides with the 0 of the energy scale. The match is quite good in the region of 0-10 eV that encompasses the region between valence and the conduction band where the Fermi level lies. The close agreement between the two bandstructures in the region of interest illustrates the accuracy of the fitted parameters.

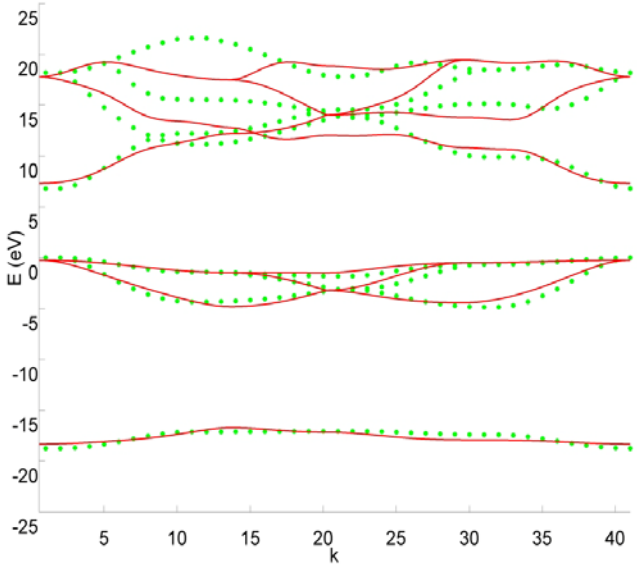

Figure 5.2: Calculated MgO bandstructure using EHT (red solid line) and DFT-PBE after correction (green dotted line). Note that the original DFT-PBE valence bands have been shifted up by 3.3 eV to match the experimental band gap, 7.8 eV [23].

5.2.4 Fermi level alignment

DFT-PBE calculations for a 4-layer MgO slab placed on a 6-layer Fe(001) slab show that the top of the MgO valence band edge is located about 3.5 eV below the Fermi level of the system. Therefore, a similar offset is used in our EHMO-based transport calculations. This value is consistent with the FLAPW-DFT study of 2 ML of Fe adsorbed on a 6 ML MgO slab, Li et al. where the authors find that the top of the MgO valence band lies ~3.5 eV below the Fermi level [24]. This finding is also supported by experimental study of MgO(1-6ML)/Fe multilayer where Wulfhekel et al. find the difference between the MgO valence band and Fe Fermi level to be 3.6 eV from ultraviolet photoemission spectra [25].

5.3 Results and the discussions

In Figure 5.3(a), the barrier thickness dependence of the TMR ratio is presented. The TMR ratio in the Figure corresponds with the so-called pessimistic TMR ratio, defined as:

$$TMR = \frac{I_P - I_{AP}}{I_P}$$

Where $I_p(I_{AP})$ denotes current in the parallel (anti-parallel) configuration.

From the figure it is clear that the TMR ratio increases with the thickness of the barrier film. This increase is more pronounced for thinner layers. For example, the TMR ratio for a 2 ML MgO thick barrier is 0.88 and increases quickly to 0.95 for a 4 ML barrier. With further increase in the barrier thickness, the rate of increase diminishes and for a 20 ML thick barrier the TMR ratio saturates to 0.98.

The increase in the TMR ratio can be understood from the individual conductances, as plotted in Figure 5.3(b). In the Figure the variation of the conductance is plotted on a logarithmic scale against the thickness of the MgO barrier. The plot shows that the conductance of the majority electrons is always higher than for the minority electrons for all the considered thickness. This behavior confirms the experimentally observed positive spin polarization of a MTJ consisting of Fe electrodes with an amorphous Al_2O_3 barrier [26]. Also from the plot, the exponential decay of all the conductances for thicker barrier is quite clear. The rate of decay, even in the asymptotic regime is, however, different for all the three conductances. The majority conductance decays (decay constant 0.40 $Å^{-1}$) slower compared to the minority conductance (decay constant 0.50 $Å^{-1}$) as well as anti-parallel conductance (decay constant 0.46 $Å^{-1}$). Indeed, the slower decay rate of the majority electrons give rise to the increasing TMR ratio with thickness. The difference in the decay rate for the three conductances alludes to the different mechanism of the transport which becomes evident when we look at the $\vec{k}_{||}$-resolved transmission coefficients in Figure 5.4.

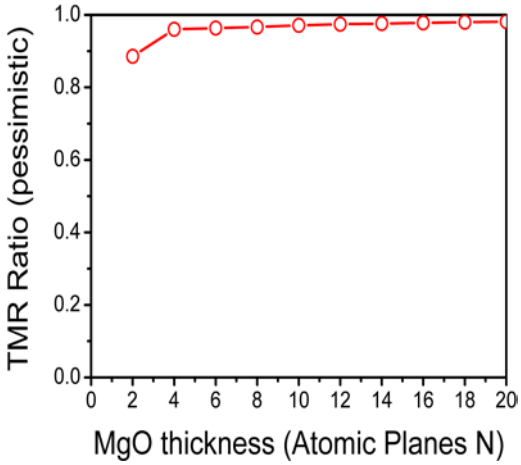

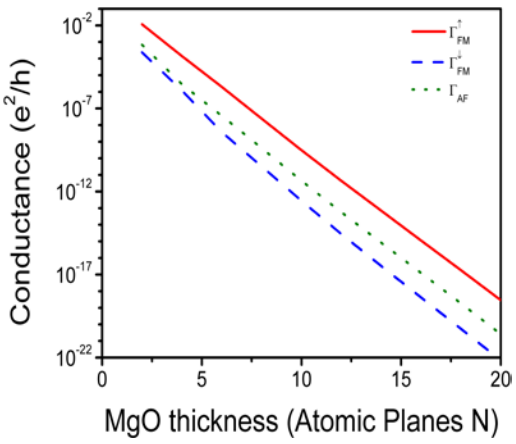

Figure 5.3: (a) Dependence of the pessimistic TMR ratio R_{TMR} of an Fe|MgO|Fe(001) junction on the MgO thickness. (b) Dependence of the individual conductances $\Gamma_{FM}^{\uparrow}$, $\Gamma_{FM}^{\downarrow}$ and Γ_{AF} on the MgO barrier thickness.

In Figure 5.4.1 $T(E, \vec{k}_{||})$ for a 4 ML MgO barrier is shown, while Figure 5.4.2 corresponds to a 8 ML MgO barrier. The selected thicknesses of the MgO barrier represent typical conductances in the pre-asymptotic and asymptotic tunneling region, respectively. In the pre-asymptotic region, the majority-to-majority conductance is dominated by a small circular region around the Gamma point. The minority-to-minority conductance, however, is dominated by four rectangular shaped regions lying at the edges of the Brillouin zone along $k_x = 0$ and $k_y = 0$ lines. There are also two rectangular ring-shaped regions with their centers at Gamma point where the conductances are comparatively higher but not as high as in the edge regions. These two rings are rotated 45° with respect to each other and the corner of the inner ring joins the center of the edge of the outer ring. Finally, in the anti-parallel alignment, the dominant region for the conductance appears to be a convolution of the high conductance region of the majority-to-majority and minority-to-minority conductance. It has a high conductance rectangular ring around the Gamma point which is reminiscent of the minority-to-minority conductance whereas large thickness of the ring and comparatively higher value of $T(E)$ points to its similarity with the majority-to-majority transport.

For the 8 ML MgO barrier (Figure 5.4), the regions of high conductance for all the three cases move closer to the Gamma point. For the majority-to-majority transport, the radius of the circular region with high conductance becomes smaller. For the minority-to-minority transport, the inner rectangular ring region and the lobe joining it to the outer rectangular region become very

prominent. On the other hand, the regions far from the Gamma point become less important. In fact, the rectangular region near the edges of the Brillouin zone and the outer rectangular ring region contribute less than 0.1% for this thickness. Finally, the conductance map for the anti-parallel alignment follows the same trend. In this case, the outer and inner radii of the ring shrink and the high conductance region moves towards the Gamma point. It is interesting to note that both for the thicker as well as thinner barrier there is a hole in the conductivity map of minority-to-minority as well as anti-parallel alignment at the centre of the Brillouin zone. The wave function matching method of McLaren et al. [8] demonstrates that the hole originates from the symmetry mismatch of the tunneling electrons for the anti-parallel alignment.

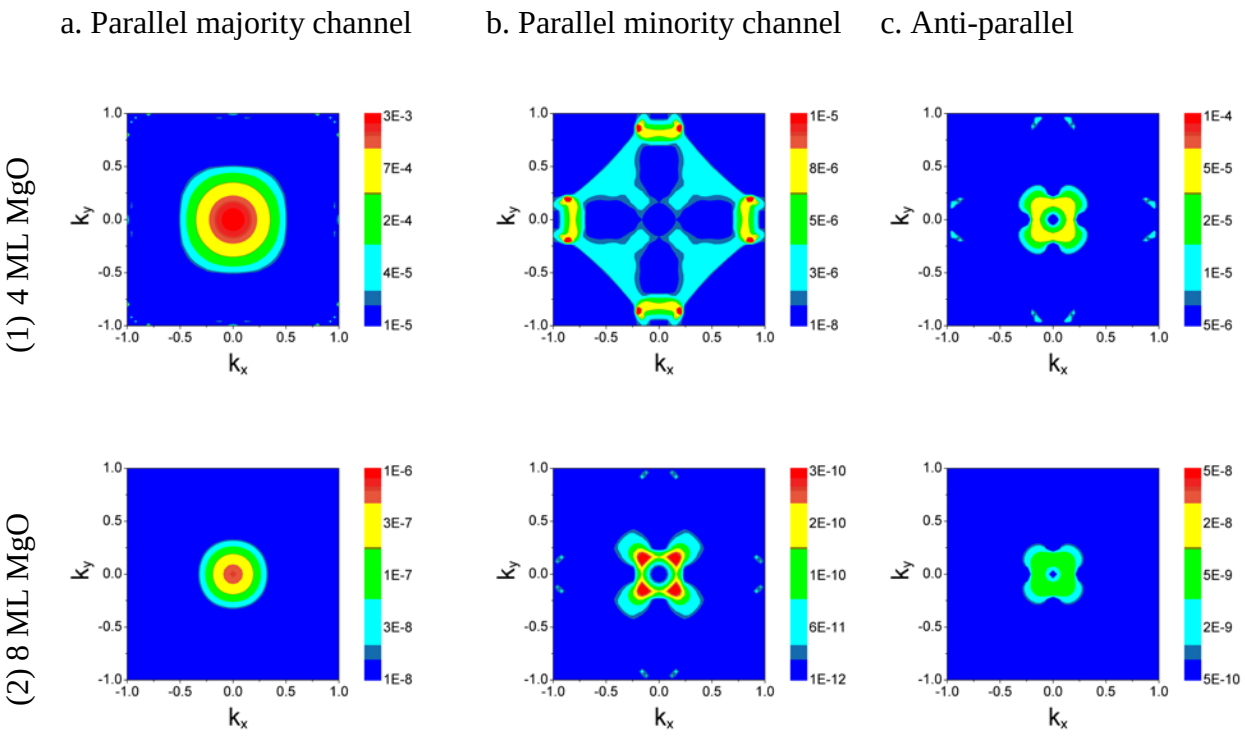

Figure 5.4. $\vec{k}_{||}$ resolved transmission probabilitities for a Fe|MgO|Fe(001) junction with 1).four atomic planes of MgO and 2) eight atomic planes of MgO: (a) Majority-to-majority, $\tilde{T}^{\uparrow}_{FM}(\vec{k}_{||})$, (b) Minority-to-Minority, $\tilde{T}^{\downarrow}_{FM}(\vec{k}_{||})$ and (c) Anti-parallel, $\tilde{T}_{AF}(\vec{k}_{||})$

The conductance behavior can be understood qualitatively from the surface spectral density of the Fe(001) surface and from the complex Fermi surface of the MgO barrier. The surface spectral density of the Fe(001) illustrates availability of tunneling electrons in the electrodes while the complex Fermi surface illustrates how these states decay inside the MgO barrier. The surface spectral density in Figure 5.5 shows that the majority states are distributed quite uniformly throughout the Brillouin zone. Their concentration is higher along two perpendicular strips passing through the center of the Brillouine zone and parallel to the k_x and k_y axis. The minority electrons, however, are distributed along the thin ring shaped area with its center at the Gamma point. There are also more sharply localized thin strips of high density along the four corners.

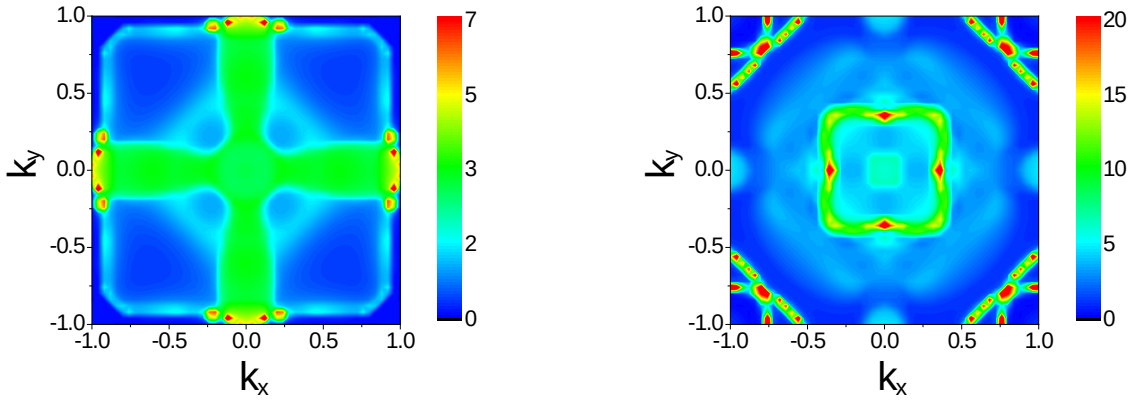

Figure 5.5: Spectral density for the Fe[001] surface at Fermi level (1) majority electrons (2) minority electrons.

The complex Fermi surface of MgO shows that the region of the smallest decay lie in the circular area with its center at Gamma point [7]. As a result, perpendicular tunneling ($\vec{k}_{||} = 0$) inside

MgO barrier is favored. There are also four subsidiary minima along ($k_x = k_y$) lines which are responsible for the lobes found in the minority-to-minority conductance map.

Qualitatively, the surface spectral density of Fe(001) and complex Fermi surface of MgO are able to explain the observed conductance behavior shown in the Figure 5.4. For small thicknesses, Figure 5.4.1, electrons everywhere in the Brillouin zone are able to overcome thin MgO barrier. Thus for small thicknesses, the conductivity map closely mirrors the spectral density of the Fe electrodes. For majority-to-majority transport that means the region of higher conductance lie in and around the center of the Brillouin zone where there is a higher concentration of the majority electrons. The low decay constant inside MgO barrier near the center of the Brillouin zone further enhances the conductivity of the electron in that region compared to other regions. For minority-to-minority transport, the regions of the high conductance lie away from the center of the Brillouin zone as minority electrons have no states in and around the center of the Brillouin zone. Also the location of the high conductance region roughly matches with the Fe(001) minority surface spectral density. For the anti-parallel alignment, as expected, the conductivity map appears to be the superposition of the majority-to-majority and minority-to-minority conductance map. For thicker layer (Figure 5.4.2) the decay of the states inside the barrier becomes more important. Consequently, for all the three cases, the region of the high conductance move closer to the center of the Brillouin zone where the decay constant is quite low.

5.4 Summary

The spin-dependent transport through a Fe|MgO|Fe multilayer was studied using the non-equilibrium green function formalism coupled with extended Huckel theory. The study is able to replicate the quantitatively increasing TMR ratio with the increasing thickness of the barrier material [7,8]. This study is also able to illustrate major features of the conductivity map for both thicker as well as thinner barriers. More importantly, despite the sensitivity of the results on the EHT parameters , this study finds the decay rate inside the MgO barrier to be 0.40 $Å^{-1}$ and 0.50 $Å^{-1}$ for the majority and minority electrons, respectively which is very close to the earlier reported value of 0.44 $Å^{-1}$ and 0.49 $Å^{-1}$ [22]. Thus, this work demonstrates that NEGF coupled with EHT theory provides an ideal framework to study spin-dependent transport in MTJs. Next, this theory is used to study the effect of the biaxial strain in MgO magnetic tunnel junction which is described in the next chapter.

Table 5.1. EHT parameters for MgO used in the calculation. The parameters are obtained by minimizing the error between the corrected DFT-PBE bandstructure and the EHT bandstructure. The values under E_{ii} (2^{nd} column) are the Coulomb energies of the orbitals shown in the leftmost column. Values under ζ_1 (3^{rd} column) and ζ_2 (5^{th} column) are the orbitals exponents and the values under c_1 (4^{th} column) and c_2 (6^{th} column) are their corresponding coefficients.

Mg	**E_{ii} (eV)**	**ζ_1**	**c_1**	**ζ_2**	**c_2**
3 s	-7.66153	0.81483	0.57383	11.52503	0.81471
3p	-6.74562	0.93823	0.77203	12.97422	0.62945
O					

2 s	-30.21043	2.57873	0.0001	2.94646	0.9999
2 p	-15.35389	1.3255	0.40594	3.97295	0.73713

References

[1] J. S. Moodera and P. LeClair, *Nat. Mater.* **2**, 707 (2003).

[2] A. Ney, C. Pampuch, R. Koch, and K. H. Ploog, *Nature* **425**, 485 (2003).

[3] S. A. Wolf, D. D. Awschalom, R. A. Buhrman, J. M. Daughton, S. von Molnár, M. L. Roukes, A. Y. Chtchelkanova, and D. M. Treger, *Science* **294**, 1488 (2001).

[4] M. Julliere, *Phys. Lett. A* **54**, 225 (1975).

[5] E. Y. Tsymbal, O. N. Mryasov, and P. R. LeClair, *J. Phys. Condens. Matter* **15**, R109 (2003).

[6] H. Yang, S.-H. Yang, D.-C. Qi, A. Rusydi, H. Kawai, M. Saeys, T. Leo, D. Smith, and S. Parkin, *Phys. Rev. Lett.* **106**, 167201 (2011).

[7] J. Mathon and A. Umerski, *Phys. Rev. B* **63**, 220403 (2001).

[8] W. Butler, X.-G. Zhang, T. Schulthess, and J. MacLaren, *Phys. Rev. B* **63**, 054416 (2001).

[9] S. S. P. Parkin, C. Kaiser, A. Panchula, P. M. Rice, B. Hughes, M. Samant, and S.-H. Yang, *Nat. Mater.* **3**, 862 (2004).

[10] S. Yuasa, T. Nagahama, A. Fukushima, Y. Suzuki, and K. Ando, *Nat. Mater.* **3**, 868 (2004).

[11] J. Cerdá, M. A. V. Hove, P. Sautet, and M. Salmeron, *Phys. Rev. B* **56**, 15885 (1997).

[12] J. Cerdá and F. Soria, *Phys. Rev. B* **61**, 7965 (2000).

[13] P. Sautet and C. Joachim, *Phys. Rev. B* **38**, 12238 (1988).

[14] P. Sautet and C. Joachim, *Chem. Phys. Lett.* **185**, 23 (1991).

[15] S. Corbel and J. Cerda, *Phys. Rev. B* **60**, (1999).

[16] T. Kanaji, T. Kagotani, and S. Nagata, *Thin Solid Films* **32**, 217 (1976).

[17] C. Li and A. Freeman, *Phys. Rev. B* **43**, 780–787 (1991).

[18] R. Hoffmann, *J. Chem. Phys.* **39**, 1397 (1963).

[19] M. C. Munoz, V. R. Velasco, and F. Garcia-Moliner, *Prog. Surf. Sci.* **26**, 117 (1987).

[20] J. Cerdá, A. Yoon, M. Van Hove, P. Sautet, M. Salmeron, and G. Somorjai, *Phys. Rev. B* **56**, 15900 (1997).

[21] R. Landauer, *IBM J. Res. Dev.* **32**, 306 (1988).

[22] T. Z. Raza, J. I. Cerdá, and H. Raza, *J. Appl. Phys.* **109**, 023705 (2011).

[23] U. Schönberger , F. Aryasetiawan, *Phys. Rev. B* **52**, 8788 (1995).

[24] C. Li, *Phys. Rev. B* **43**, 780 (1991).

[25] W. Wulfhekel, M. Klaua, D. Ullmann, F. Zavaliche, J. Kirschner, R. Urban, T. Monchesky, and B. Heinrich, *Appl. Phys. Lett.* **78**, 509 (2001).

[26] J. S. Moodera, L. R. Kinder, T. M. Wong, and R. Meservey, *Phys. Rev. Lett.* **74**, 3273 (1995).

CHAPTER 6

Biaxial strain effect of spin dependent tunneling in MgO magnetic tunnel junctions

6.1 Introduction

The material and interface engineering of magnetic tunnel junctions (MTJ) is the key for the future of spin transfer torque based random access memories (STT-RAM). A value of tunneling magnetoresistance (TMR) exceeding 1000% has been predicted [1,2] and recently achieved in MTJs with single crystalline or textured MgO(001) tunnel barriers [3–5] through which the Δ_1 Bloch states tunnel coherently. In this case, the crystalline property of the structure, especially that of the ferromagnet/MgO interface plays a very critical role in the device performance [6,7] and the presence of strain in the structure can change the properties of the device significantly. Strain has been used to improve the performance of semiconductor devices such as the metal oxide semiconductor field effect transistors (MOSFETs) without failure at low cost over the last decade [8]. Recently, a new line stressor based on diamond like carbon (DLC) films has been proposed with very high intrinsic stress (few GPa) and high sp^3 content [9,10].

For the case of MgO based MTJs, the role of epitaxial strain has been discussed previously [11]. Yeo et al. studied the interface states of a strained MgO/Fe(001) system and showed the position of the minority spin peak state near the Fermi energy shifts upwards in energy with respect to the Fermi energy for tensile strain, while it moves downwards for compressive strain [12]. A few experimental reports have been also studied the effect of lattice mismatch on the transport properties in Fe/MgO/Fe(001) and related systems [13–15].

In this work, we study the effect of a DLC film on the tunneling behavior of MgO based MTJs. With the deposition of DLC film over tunnel junctions, the TMR as well as the junction resistance is suppressed showing the effect of external mechanical strain on the transport properties. Though the TMR is reduced, it is interesting to understand the physics behind it and the strain induced reduction of the junction resistance is encouraging for industries utilizing MTJs as read sensors in hard disk drives. To corroborate the experimental results, the effect of biaxial strain is evaluated using Non-equilibrium Green's function (NEGF) quantum transport calculations. The minority and the anti-parallel transmission both increase more than the majority transmission, and biaxial compressive strain is calculated to decrease the TMR ratio, in agreement with the experiments.

6.2 Experimental method and result

MTJs have been grown using magnetron sputtering in an ultra-high vacuum chamber with the structure of 100 Ta/300 $Ir_{22}Mn_{78}$/6 $Co_{40}Fe_{40}B_{20}$/30 $Co_{70}Fe_{30}$/8 Ru/27 $Co_{70}Fe_{30}$/8 Mg/14 MgO/20 $Co_{40}Fe_{40}B_{20}$/50 Ta/50 Ru (all thickness in Å). The MgO barrier is formed by the reactive sputter deposition of Mg in Ar-O_2 plasma (~2% oxygen). Samples are annealed at 300 ˚C for 30 minutes under 1 T magnetic field, and then MTJs are fabricated in a current perpendicular-to-plane (CPP) configuration using a combination of Ar ion-milling and photolithography processes. A number of devices of different junction areas are measured after fabrication and a 40 nm DLC film is then deposited over the junction. Figure 6.1(a) shows a schematic diagram of the device with the DLC layer on top, exerting a compressive biaxial strain on the tunnel junction along x and z axes [9], while Figure 6.1(b) shows a scanning electron microscope (SEM) image with a DLC

film over a tunnel junction. DLC films are grown byfilter ed cathodic vacuum arc and a method used by Ehsan et al. has been adopted that provides good adhesion along with high sp^3 content for enough strain [16]. Ion energy of about 100 eV is selected as it provides the highest fraction of sp^3 bonds with the maximum density and hardness.

Figure 6.1(c) shows the X-ray photoelectron spectroscopy (XPS) spectra of the C_{1s} core level for the DLC film, which indicates a very high sp^3 proportion (65%) of the film as has been used for MOSFETs with compressive stress as high as 7.5 GPa [9]. A higher sp^3 fraction in the DLC film is important to induce enough strain. The atomic fraction of each component (C-C sp^1, C-C sp^2, C-C sp^3, C=O, and C-O) is obtained by integrating the associated Gaussian curves deconvoluted from the C_{1s} spectra after Shirley background subtraction [16].

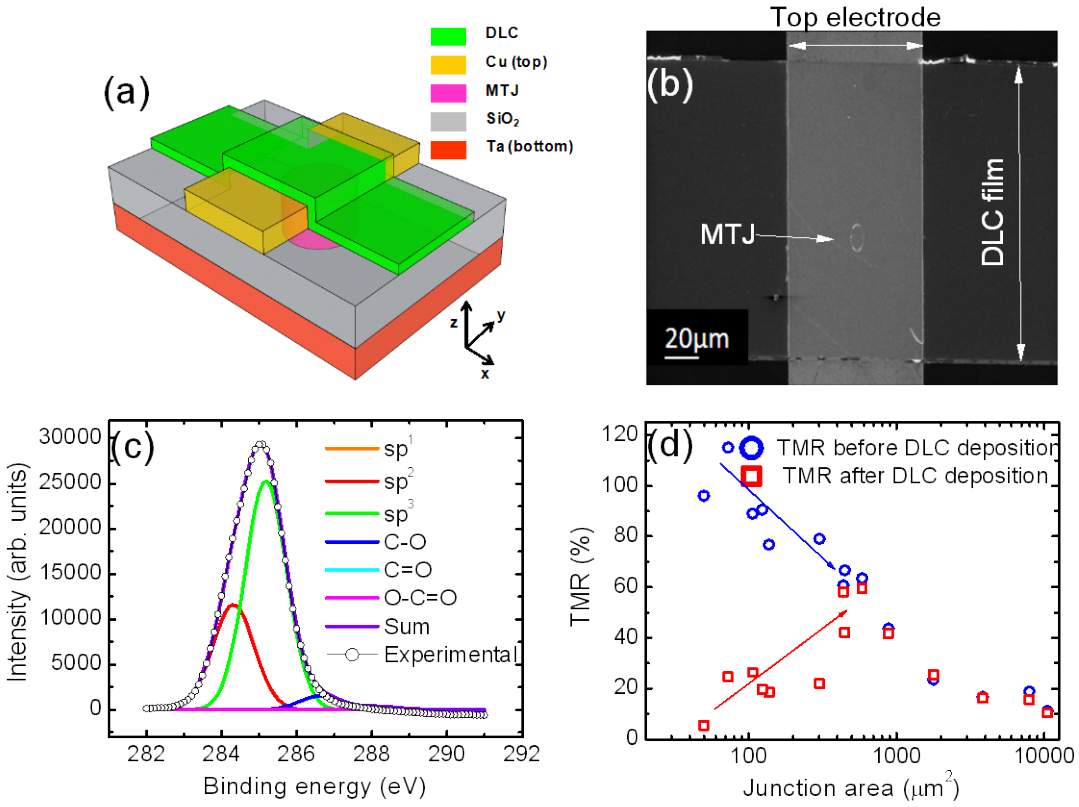

Figure 6.1: (a) Schematic of the device with a DLC layer over the junction. (b) An SEM image with a DLC film. The top electrode width is 80 μm while the DLC strip has a width of 150 μm. (c) XPS spectra of the C_{1s} core level for the DLC film. (d) A plot of TMR versus junction area.

Figure 6.1(d) shows a plot of the TMR versus the junction area before and after the deposition of DLC film at room temperature. The TMR ratio is defined by $(R_{AP}-R_P)/R_P$, where R_P and R_{AP} are the junction resistance in the parallel (P) and anti-parallel (AP) alignment of the ferromagnetic electrodes, respectively. Before the deposition of the DLC film, it is observed that the TMR gradually reduces as the junction area increases. The DLC film is then deposited over tunnel junctions of areas ranging from 50 to 10^4 μm^2. It is clearly observed that there is a suppression of TMR for junction areas below 500 μm^2, and that the TMR after the DLC deposition gradually reduces as the junction area decreases. The change due to the DLC layer is bigger in the devices with smaller junction areas due to higher effective strain in a smaller junction. The free layer loop of the device before and after the DLC deposition has no difference, therefore we rule out any possibility of pinholes in our samples due to strain, otherwise a shift in the free layer loop at lower temperatures is expected [17]. We have also done transport of ions in matter calculations for the energy of C ions used in this study. The maximum penetration depth of C in the Cu top electrode (100 nm thick) is only 5 nm with a peak at ~ 1 nm, which also support that the junction damage due to the DLC deposition is negligible.

The voltage dependence of the TMR and junction resistance show a tunneling feature before the DLC deposition as shown in Figure 6.2(a), such that the TMR decreases with increasing bias voltage and R_P is independent of bias voltage, as typically observed in MgO based MTJs [18]. Figure 6.2(b) shows suppression in the voltage dependence of TMR after the deposition of the DLC film over the device. For the unstrained device, the relative reduction in TMR at 0.4 V is

43% with respect to the value at zero bias, while for the strained device the relative reduction is only 14%. We have also carried out temperature dependent studies. For the unstrained device, R_P has little temperature dependence, while R_{AP} increases as the temperature reduces shown in Figure 6.2(c). On the other hand, when the same device is strained using the DLC film, in addition to reduction in the magnitude of TMR and R_{AP}, their temperature dependence is also suppressed as shown in Figure 6.2(d). These observations can be related to the changes in the tunneling probabilities as shown by our calculations later.

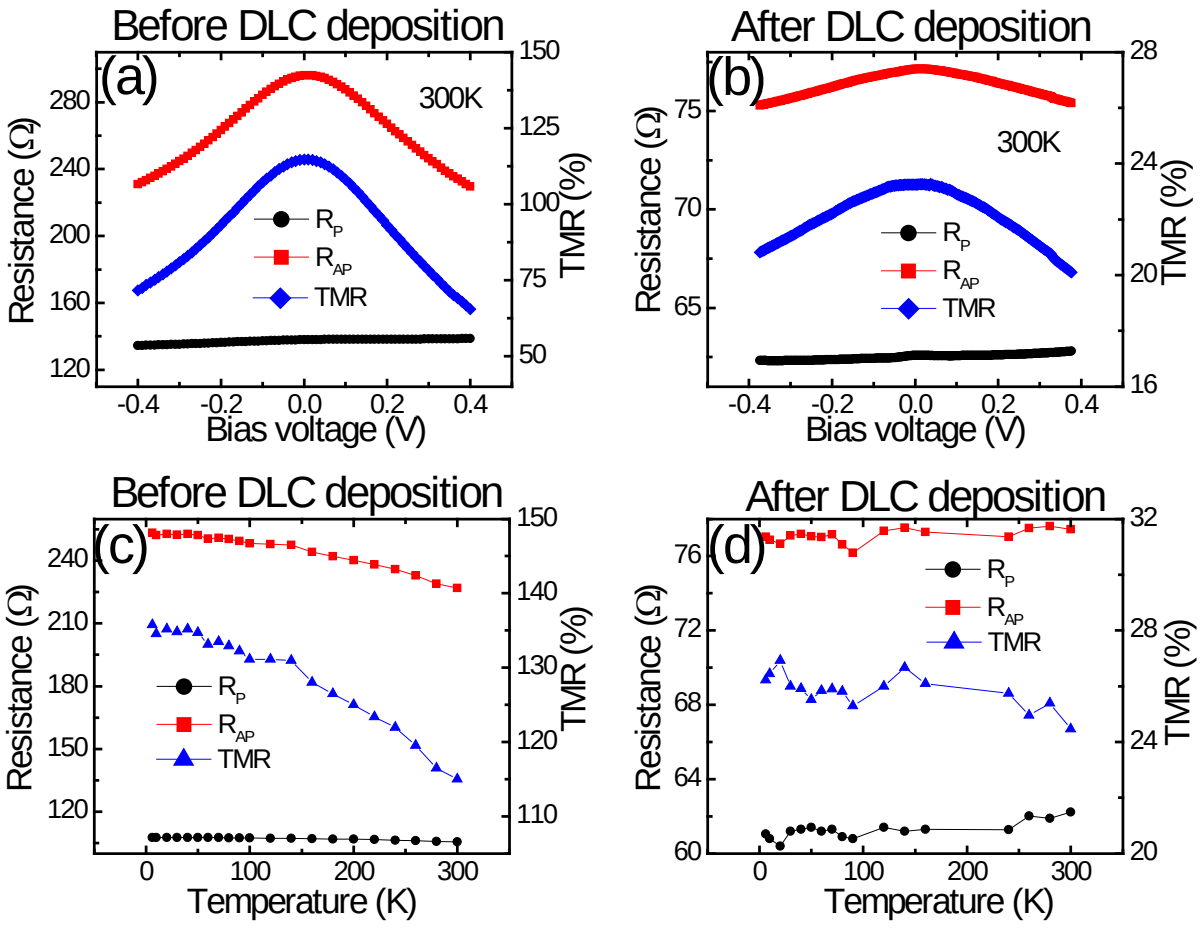

Figure 6.2: Bias voltage dependence of R_P, R_{AP}, and TMR for MTJ before (a) and after (b) the DLC deposition at 300 K. Temperature dependence of R_P, R_{AP}, and TMR before (c) and after (d) the DLC deposition, for a device with the junction area of 73 μm^2.

6.3 Computational method and result

Coherent tunneling transport in a Fe/MgO/Fe tunneling junction [Figure 6.3(c)] is described by the NEGF formalism [19] as implemented in the Green program [20,21]. The electronic structure of the tunneling junction is described by an Extended Hückel Molecular Orbital (EHMO) Hamiltonian [22], using literature values for the Fe spd, Mg spd, and O sp parameters [23]. With those parameters, a bulk MgO band gap of 7.8 eV and a bulk Fe magnetic moment of 2.0 μB are calculated, in good agreement with experimental data of 7.77 eV and 2.2 μB, respectively [24,25], and with hybrid density functional theory calculations using the HSE03 functional (DFT-HSE03) [26–28]. Detailed DFT-HSE03 calculations for a 4-layer MgO slab on a 6-layer Fe(100) slab show that the top of the MgO valence band edge is located about 4.0 eV below the Fermi level of the system. Therefore, a similar offset is used in our EHMO-based transport calculations. Note that the EHMO band gap for a 6-layer MgO slab, 7.2 eV, is significantly larger than the DFT-HSE03 value of 3.7 eV. The effect of biaxial strain on the MgO band gap is, however, accurately described by EHMO, as discussed below.

Transport calculations are performed for MgO barriers of 4, 6, 8, 10, and 12 layers. For the unstrained transport calculations, the experimental Fe lattice constant of 2.87 Å is used for the Fe(100) contacts. MgO(001) slab, rotated 45 degrees with respect to the Fe lattice, is then placed 2.16 Å over Fe (100) contacts so that O atoms sit directly above Fe atoms. Assuming a biaxial stress in the range of 5 to 10 GPa leads to a compression of about 2.5 to 5%. Therefore, the effects of compression on the conductance and the TMR ratio are evaluated for a compression of 5% along the x and z direction [as defined in Figure 6.3(c)], and an expansion of 2.3% in the y direction using the MgO Poisson ratio of 0.187 [29,30]. In reality, the compression is likely

somewhat smaller than 5%. To confirm that our results remain valid for different amounts of strain, transport calculations are also performed for a 6-layer MgO junction with 2.5%, 3.5% and 10% compressive strain.

The effect of 5% biaxial xz-strain on the junction conductance is calculated as shown in Figure 6.3(a) for different MgO barrier thicknesses. For the unstrained junction, both the P and AP conductance decrease exponentially with the number of MgO layers, as expected for tunneling transport. The conductance is quite sensitive to the details of the calculations. The conductance is quite sensitive to the details of the calculations. For example, the sensitivity of the TMR results to the EHT parameters of MgO has been examined by Raza et al. [23] where two sets of EHT parameters were used for MgO. One set reproduces the experimental band gap of 7.8 eV while the other set reproduces LDA-DFT band gap of 5.2 eV. The authors find that the current and the TMR ratio trend with the increasing thickness remains the same in both the cases, their actual values, however, differ. For example, EHT parameters that reproduces the experimental band gap of 7.8 eV give a %TMR ratio of 1200% for 4 layers of MgO which changes to 2500% when the parameters corresponding to LDA-DFT bandgap are used. Also due to its technological significance, many authors have studied Fe|MgO|Fe system. All the authors find similar trend of current and the TMR ratio with increasing thickness of MgO layers. However the actual values differ quite significantly. This shows utility of the theoretical calculations in establishing trends while pointing towards its inability to get quantitative values. Considering the sensitivity of the results to the parameters our decay rate of 0.40 $Å^{-1}$ for the P configuration and 0.50 $Å^{-1}$ for the AP configuration appear to agree well with published values of 0.44 and 0.49 $Å^{-1}$, respectively [23]. The different decay rate can be understood from the $\vec{k}_{||}$resolved transmission

spectra in Figure 6.4. While majority-to-majority transport is dominated by states near the gamma point, no such states are available for minority-to-minority transport in agreement with earlier calculations [2]. This can be understood from the Fe(100) surface spectral density at the Fermi energy [Figure 6.5] and from the complex band structure of MgO [2]. The complex MgO band structure shows that the decay rate is minimum in a small region around the gamma point and increases away from the gamma point [2]. Therefore, the decay rate in the MgO junction is higher for the minority states.

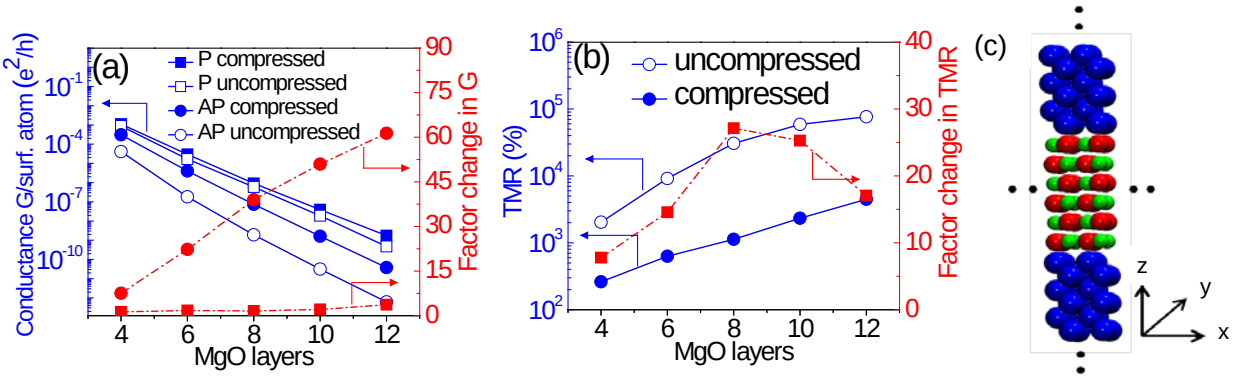

Figure 6.3: (a) Calculated conductance for a Fe(100)/MgO/Fe(100) tunneling junction as a function of the number of MgO layers. The conductance is shown for the P and the AP configurations for both the unstrained and for 5% biaxial *xz*-strain cases. The relative increase in the conductance after applying strain is also shown to facilitate comparison with the experimental data in Figure 6.2. For 6 MgO layers, the P conductance increases by a factor 1.74 from 0.65 to 1.14 nS, while the AP conductance increases by a factor 22.32 from 7 to 157 pS. (b) Optimistic TMR ratio [$(G_P-G_{AP})/G_{AP}$, where G_P and G_{AP} is the conductance of the P and the AP state, respectively] for the unstrained and the strained tunneling junction. The relative change in the TMR ratio is also shown and ranges from a factor 7 to 27. (c) Central structure used to model the junction for 6 layers of MgO. The blue, green, and red circles correspond to Fe, Mg, and O atoms, respectively. In the calculations, both Fe(100) contacts extend to infinity.

The application of 5% biaxial xz-strain increases the conductance for both the P and AP configuration [Figure 6.3(a)]. However, the increase is more pronounced for the AP configuration, and hence the TMR ratio decreases by a factor 10 to 30 [Figure 6.3(b)]. Biaxial strain decreases the decay constants to 0.37 and 0.45 $Å^{-1}$ for the P and the AP configuration,

respectively. In addition, the contact conductance, a measure of the number of active transport channels in the Fe(100) contacts and their coupling at the Fe(100)/MgO interface [31], increases 10-fold for the minority channels, whereas only 2-fold for the majority channels. The increase in the conductance by a factor 1.3 to 3.7 and the decrease in decay rate for the P configuration can be attributed to a decrease in the MgO band gap. Indeed, the EHMO band gap for a 6-layer MgO slab decreases from 7.29 eV to 7.02 eV, comparable to the 0.11 eV decrease calculated by DFT-HSE03. The conductance for the AP configuration is more sensitive to biaxial strain, and increases by a factor 7 for a 4-layer MgO barrier and 5% strain, and by a factor 61 for a 12-layer MgO barrier.

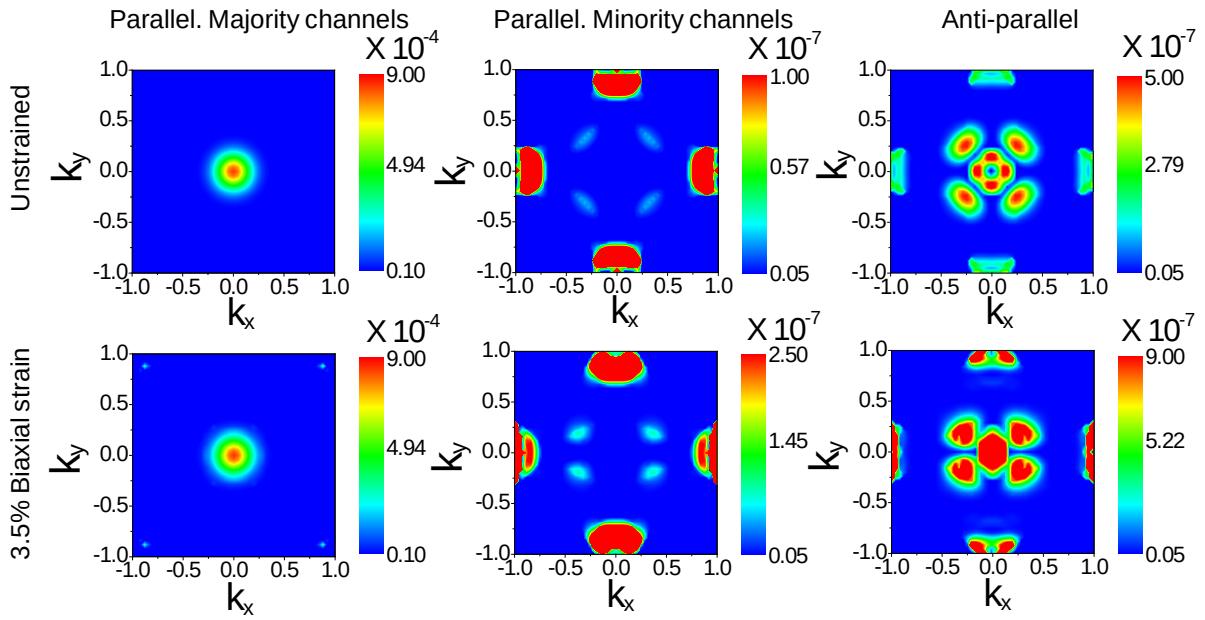

Figure 6.4: $\vec{k}_{||}$ -resolved transmission spectra for the various transport modes for a Fe(100)/MgO(6 layers)/Fe(100) junction. Biaxial strain decreases the lattice in the *x* and *z* direction by 3.5%, and expands the lattice in *y* direction by 1.6%. Note the different scales for the various transmission spectra.

To compare the calculated changes in the TMR ratio and in the conductance with the experimental values, we have included the relative changes in Figure 6.3. The 22-fold increase in

the AP conductance for 5% strain and for a 6-layer (13 Å) MgO barrier is significantly larger than the experimental increase of 2.9 for a 20 Å MgO barrier. Also the 15-fold decrease in the calculated TMR ratio for a 6-layer MgO barrier is larger than the experimental value of 4.8 for a 20 Å MgO barrier. However, when the biaxial strain is reduced to 3.5% for the 6-layer MgO junction, the agreement with the experiments improves. The calculated increases in the P and in the AP conductance by factors 1.1 and 3.0, respectively, can be compared with the experimentally measured increases by factors 1.7 and 2.9, respectively [Figure 6.2]. Also the 2.7-fold decrease in the calculated TMR ratio matches the experimental value of 4.8 quite well. The qualitative implications are preserved even for smaller levels of biaxial strain in the MgO layer.

The more pronounced increase in the conductance for the minority channels and for the AP configuration can be understood from the $\vec{k}_{||}$-resolved transmission spectra, shown in Figure 6.4 for a 6-layer MgO junction in the case of unstrained and a 3.5% biaxial strain. For the unstrained junction, majority transport is dominated by states at the gamma point. The $\vec{k}_{||}$-resolved spectra for the majority states are relatively unaffected by strain, except for a small broadening of the peak and an increase in the peak maximum from 0.846×10^{-3} to 0.853×10^{-3}. Minority transport, however, is dominated by a circle of states around the gamma point and by states near the Brillouin zone edge. Biaxial xz-strain breaks the 4-fold symmetry in the xy plane, and transmission hot-spots move closer to the $k_y = 0$ axis. The change in the location of minority states at the Fermi energy is also illustrated by the Fe(100) spectral density in Figure 6.5. The minority states are concentrated in a narrow square region around the gamma point, with few states at the gamma point. In this region the decay constant for MgO is quite high. Biaxial strain increases the orbital overlap in the x direction and hence broadens the d-band. As can be seen in Figure 6.5, this moves minority states closer to the gamma point along the k_x axis. The effect is

even more pronounced in the transmission spectrum [Figure 6.4] and new hot-spots appear near the k_y=0 axis. The change in the minority states is also reflected in a decrease in the Fe magnetic moment. For a 6-layer Fe(100) slab, the EHMO magnetic moment per Fe decreases from 1.96 to 1.86 μB, again in good agreement with the 0.14 μB decrease calculated by DFT-HSE03.

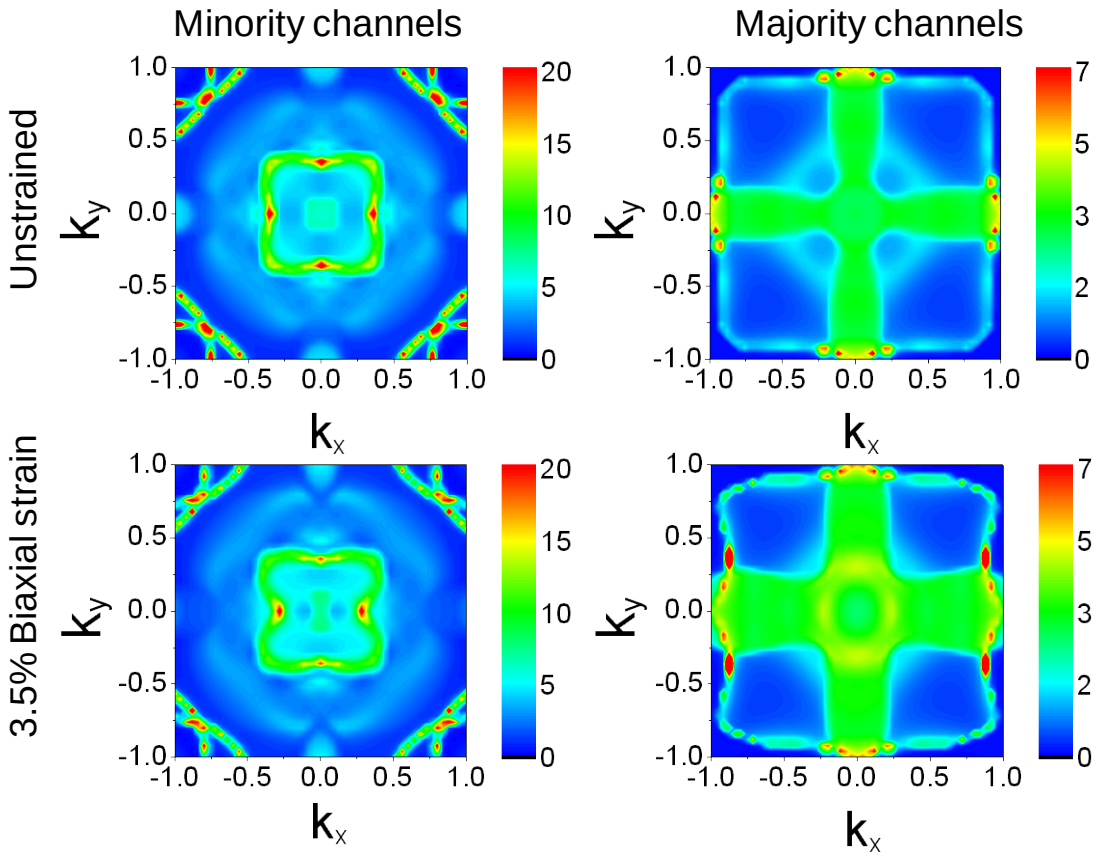

Figure 6.5: Effect of 3.5% biaxial *xz*-strain on the Fe(100) surface spectral density (number of states/eV/Å^2) at the Fermi energy for the minority and the majority states. While changes for the majority states are relatively minor, the minority states at (k_x, k_y)=(±0.4, 0.0) clearly move closer to the gamma point. This is consistent with a broadening of the minority band and a decrease in the spin polarization.

The above results also help to explain the experimental voltage and temperature dependence of the TMR. It was reported that the transmission for the minority spin channel is sensitive at low biases, however once the minority states moves closer to the gamma point, the bias dependent

transmission is significantly suppressed at higher biases [32]. From our calculations we conclude that the biaxial strain moves the minority states closer to the gamma point. This in turn weakens the sensitivity of the minority states to the voltage and temperature, resulting in a diminished voltage and temperature dependence of R_{AP} and TMR.

6.4 Summary

We have demonstrated the effect of mechanical stress on the tunnelling properties of MgO tunnel junctions. The deposition of a DLC film with a very high intrinsic stress over the junction reduces the TMR ratio as well as the junction resistance. The NEGF calculations reproduce both the increase in the conductances and the decrease in the TMR ratio, when biaxial xz-strain is applied. The increase in the conductance for the parallel configuration can be attributed to a decrease in the MgO band gap by about 0.3 eV and the barrier thickness by 5%. The conductance for the anti-parallel configuration is significantly more sensitive to strain, which is attributed to changes in the location of the Fe(100) minority states at the Femi level. When strain is applied, the d-band broadens and the minority states at the Fermi energy move closer to the center of the 2D Brillouin zone where transmission through the MgO barrier is higher. As a result, hot-spots appear in the $\vec{k}_{||}$-resolved transmission spectrum and the conductance for both the minority channel and for the anti-parallel configuration increase rapidly. This study demonstrates the important effect of strain on the anti-parallel conductance, and suggests that strain can reduce the resistance-area product for MgO based read sensors with a sufficiently high TMR value.

References

[1] W. Butler, X.-G. Zhang, T. Schulthess, and J. MacLaren, *Phys. Rev. B* **63**, 054416 (2001).

[2] J. Mathon and A. Umerski, *Phys. Rev. B* **63**, 220403 (2001).

[3] S. S. P. Parkin, C. Kaiser, A. Panchula, P. M. Rice, B. Hughes, M. Samant, and S.-H. Yang, *Nat. Mater.* **3**, 862 (2004).

[4] S. Yuasa, T. Nagahama, A. Fukushima, Y. Suzuki, and K. Ando, *Nat. Mater.* **3**, 868 (2004).

[5] S. Ikeda, J. Hayakawa, Y. Ashizawa, Y. M. Lee, K. Miura, H. Hasegawa, M. Tsunoda, F. Matsukura, and H. Ohno, *Appl. Phys. Lett.* **93**, 082508 (2008).

[6] H. Yang, S.-H. Yang, D.-C. Qi, A. Rusydi, H. Kawai, M. Saeys, T. Leo, D. Smith, and S. Parkin, *Phys. Rev. Lett.* **106**, 167201 (2011).

[7] H. Yang, S.-H. Yang, and S. Parkin, *AIP Adv.* **2**, 012150 (2012).

[8] M. Chu, Y. Sun, U. Aghoram, and S. E. Thompson, *Ann. Rev. Mater. Sci.* **39**, 203 (2009).

[9] K. M. Tan, M. Zhu, W. W. Fang, M. Yang, T. Y. Liow, R. T. P. Lee, K. H. Hoe, C. H. Tung, N. Balasubramanian, G. S. Samudra, and Y. C. Yeo, *IEEE Electron Device Lett.*, **29**, 192 (2008).

[10] X. Liu, B. Liu, E. K. F. Low, W. Liu, M. Yang, L.-S. Tan, K. L. Teo, and Y.-C. Yeo, *Appl. Phys. Lett.* **98**, 183502 (2011).

[11] J. Park and B. Yu, *Phys. Rev. B* **83**, (2011).

[12] J. N. Yeo, G. M. Jee, B. D. Yue, and B. C. Choi, *J. Korean Phys.Soc.* 1938 (2008).

[13] G. X. Miao, J. Y. Chang, M. J. van Veenhuizen, K. Thiel, M. Seibt, G. Eilers, M. Munzenberg, and J. S. Moodera, *Appl. Phys. Lett.* **93**, 142511 (2008).

[14] F. Bonell, S. Andrieu, C. Tiusan, F. Montaigne, E. Snoeck, B. Belhadji, L. Calmels, F. Bertran, P. Le Fèvre, and A. Taleb-Ibrahimi, *Phys. Rev. B* **82**, 092405 (2010).

[15] D. Herranz, F. Bonell, A. Gomez-Ibarlucea, S. Andrieu, F. Montaigne, R. Villar, C. Tiusan, and F. G. Aliev, *Appl. Phys. Lett.* **96**, 202501 (2010).

[16] E. Rismani, S. K. Sinha, S. Tripathy, H. Yang, and C. S. Bhatia, *J. Phys. D: Appl. Phys.* **44**, 115502 (2011).

[17] P. W. T. Pong, C. L. Dennis, A. Castillo, A. Chen, and W. F. Egelhoff, *J. Appl. Phys.* **103**, 07A902 (2008).

[18] A. Khan, J. Schmalhorst, G. Reiss, G. Eilers, M. Münzenberg, H. Schuhmann, and M. Seibt, *Phys. Rev. B* **82**, (2010).

[19] M. C. Munoz, V. R. Valasco, and F. Garcia-Moliner, *Prog. Surf. Sci*. **26**, 117 (1987).

[20] J. Cerdá, M. Van Hove, P. Sautet, and M. Salmeron, *Phys. Rev. B* **56**, 15885 (1997).

[21] J. Cerdá, A. Yoon, M. Van Hove, P. Sautet, M. Salmeron, and G. Somorjai, *Phys. Rev. B* **56**, 15900 (1997).

[22] R. Hoffmann, *J. Chem. Phys.* **39**, 1397 (1963).

[23] T. Z. Raza, J. I. Cerdá, and H. Raza, *J. Appl. Phys.* **109**, 023705 (2011).

[24] D. Roessler and W. Walker, *Phys. Rev.* **159**, 733 (1967).

[25] M. Acet, H. Zähres, E. Wassermann, and W. Pepperhoff, *Phys. Rev. B* **49**, 6012 (1994).

[26] G. Kresse, *Phys. Rev. B* **54**, 11169 (1996).

[27] G. Kresse and J. Furthmüller, *Comput. Mater. Sci.* **6**, 15 (1996).

[28] J. Heyd, G. E. Scuseria, and M. Ernzerhof, *J. Chem. Phys.* **118**, 8207 (2003).

[29] M. S. O. Madelung, U. Rössler, and M. Schulz, *SpringerMaterials - The Londolt-Börnstein Database* Vol.41B (1999).

[30] C. S. Zha, H. Mao, and R. J. Hemley, *Proc. Natl. Acad. Sci. U.S.A.* **97**, 13494 (2000).

[31] K. Yong, D. Otalvaro, I. Duchemin, M. Saeys, and C. Joachim, *Phys. Rev. B* **77**, 205429 (2008).

[32] C. Zhang, X.-G. Zhang, P. Krstić, H. Cheng, W. Butler, and J. MacLaren, *Phys. Rev. B* **69**, 134406 (2004).

CHAPTER 7

Origin of the reduced band gap in ultrathin MgO films

7.1 Introduction

Oxide thin films find important applications in technologically important devices such as Magnetic Tunnel Junctions (MTJ) and Field Effect Transistors (FET) [1,2]. A high Tunnel Magneto Resistance (TMR) ratio, i.e., the relative change in the resistance when the magnetization orientation of the electrodes is switched from parallel to anti-parallel, of MTJs is key to developing magnetoresistive random-access-memory, magnetic sensors and novel programmable logic devices [3–5]. The use of crystalline 1.2 to 3.2 nm thick MgO films (6 to 15 layers of MgO(001)) as the tunnel barrier materials in MTJs has resulted in a large improvements in the TMR ratio [6,7]. The high TMR ratio results from the spin-dependent coherent electron transport in crystalline MgO thin films and underlines the importance of the electronic structure of the barrier material [8,9]. Recent work by Yang et al. [10] shows that the TMR ratio can even be inverted by the introduction of an ultrathin 1 to 2 ML NiO film between the MgO barrier and one of the electrodes, and further illustrates the sensitivity of TMR ratio to the electronic structure of the barrier material and its interfaces.

Also for FETs, new oxide barrier materials are desired. The relentless downscaling of transistors has reduced the thickness of the SiO_2 barrier to a few atomic layers. For such thickness, the tunneling leakage current becomes considerable, and leads to a degradation in the device performance. Recently, it was proposed to replace the SiO_2 barrier with MgO [11] because of the larger MgO bulk band gap of 7.8 eV and the higher bulk dielectric constant of 9.8, as compared to SiO_2.

One of the material properties that determine the tunneling current is the band gap of the barrier material, more precisely the difference between the Fermi energy of the electrodes and the conduction band edge of the barrier film. Interestingly, the measured barrier height of MTJs, 0.39 eV, [6] is considerably lower than the barrier of about 3.7 eV estimated from the bulk MgO band gap, 7.8 eV. This difference has been attributed to the presence of oxygen vacancy defects in the MgO thin films [6]. Oxygen vacancies can be formed during the growth of the MgO film on the Fe electrode substrate, and are attributed to strain induced by the lattice mismatch. Oxygen vacancies introduce gap states about 1.2 eV below the bulk conduction band edge [12], and could therefore reduce the measured tunneling barrier height. Using reflection high-energy electron diffraction and low-energy electron diffraction patterns and scanning tunneling microscopy images, Klaua et al. however demonstrated that for very thin MgO(001) films grown on high-quality Fe(001) single crystals, the thickness of the film also affects the measured barrier height [13]. For very thin and vacancy-free films, the barrier height measured by scanning tunneling spectroscopy is much smaller than expected from the MgO bulk band gap. Moreover, the barrier height is a strong function of the film thickness and increases from 2.5 to 3.6 eV when the MgO thickness increases from 2 to 6 layers. Scanning tunneling spectroscopy studies by Schintke et al. [14] also showed that the band gap of thin MgO(001) films grown on Ag(001) increases with film thickness and converges for about 3 MgO layers. A similar trend was reported by Noguera [15] using Hartree-Fock theory calculations. The unique electronic properties of ultrathin oxide films were also observed in DFT calculations [16]. For example, the significant reduction in

the band gap of a two-layer Al_2O_3 film was attributed to a reduced Madelung potential at the undercoordinated surface sites.

This behavior is very different from the *increase* in the band gap of semiconductor nanostructures with decreasing dimensions. DFT calculations for example illustrates that the band gap decreases with the number of Si layers in a Si/SiO_2 multilayer [17]. An increase in the band gap was also calculated and measured for various semiconductor nanoparticles and nanowires as the size decreases [18]. In both cases, the increased band gap at the nanoscale was attributed to quantum confinement.

In this work, we studied the effect of the thickness on the electronic properties of ultrathin MgO(001) films. To obtain an accurate description of the band gap, ab initio HSE03-G_0W_0 calculations were used. This approach is known to provide an accurate description of the electronic structure of oxides [19]. The calculations show that the band gap of the MgO thin film decreases significantly as the thickness decreases below 1 nm or 5 ML. To understand this effect, a qualitative model was developed which includes variations in the Madelung potential and in the charge transfer between Mg and O.

Our work on the thickness dependent bandgap started from our unexpected observation of increasing bandgap with increase in thickness during the simulation. We decided to study this effect in more detail and found an experimental paper that reported similar trends and claimed that theoretical modeling is needed to understand this size dependent phenomenon. That is when we started a systematic study using state-of-the-art ab-initio HSE03-G_0W_0 calculations. Additionally, we built a

qualitative model that explains the observed trend from the change in the Madelung potential and the Bader charges as the thickness of the slab increases. It is only during the later part of our work, we came across the work in references [15] and [16]. Those two works also show the same trend even though they have used a lower level of theory (Hartree Fock and DFT).

The Madelung potential is the potential felt by an ion in a crystal due to the presence of all other ions. It is calculated from the Madelung constant, C_M, which is given by

$$C_M = \sum_{m,n,p}{}' \frac{(-1)^{m+n+p}}{\sqrt{m^2+n^2+p^2}}$$

The above expression sums the $1/r$ terms in the Coulomb potential. The $(-1)^{m+n+p}$ term accounts for the presence of alternating positive and negative charges. The prime over the summation sign indicates that the term corresponding to the zero vector $(m,n,p) = (0,0,0)$ should be avoided as an ion does not feel any potential due to itself.

To determine the charges on atoms, we have used Bader charges [28]. The Bader charge of an atom in a molecule is a charge inside a volume containing the atom that is demarcated from the rest of the molecule by a zero-charge-flux –surface, i.e. surface where the gradient of the electron density becomes zero. This method gives charges on atoms that are independent of the basis-set employed. Additionally, this method does not require the assignment of basis functions to an specific atom which is particularly important for our case as we have used plane wave basis-set.

7.2 Computational Methods

MgO(001) films with a thickness ranging from 1 to 5 layers were studied using periodic Density Functional Theory [20] with the Perdew-Burke-Enzerhoff functional (DFT-PBE) [21] as implemented in the Vienna Ab Initio Simulation (VASP) package [22,23]. The calculations were performed with a plane-wave basis set with a cutoff kinetic energy of 450 eV and the electron-ion interactions were described by the projector-augmented wave (PAW) method [24]. The MgO film was modeled with a (1x1) unit cell, and the atoms were kept frozen at their lattice positions. The experimental MgO lattice constant of 4.21 Å was used. The atoms moved by less than 1% upon geometry optimization as found in previous study [25]. The Brillouin zone was sampled with a 10x10x1 Monkhorst-Pack grid [26], and a Hermite-Gaussian smearing with a width of 0.2 eV was used. Repeated slabs were separated by a vacuum of 10 Å.

Since DFT-PBE underestimates the bulk MgO band gap by 3.2 eV, the variation of the band gap was also studied with the ab initio GW method [19]. We used the HSE03-G_0W_0 approach [27], which is reported to provide an excellent balance between accuracy and speed [27]. 256 frequency points and 160 electronic bands were used to determine the electronic structure. The vacuum layer was increased to 15 Å to converge the calculated band gap within 0.1 eV. With these setting, a bulk MgO band gap of 7.7 eV was calculated, in good agreement with experimental values.

For the calculation of the charge transfer, we have used Bader's partitioning method [28,29].

7.3 Results and Discussion

The DFT-PBE band structure for bulk MgO is shown in Figure 7.1. The calculated bulk band gap of 4.57 eV is in good agreement with the 4.65 eV DFT-LDA band gap reported by Schonberger et al. [30], but much lower than the experimental band gap of 7.8 eV [31]. The underestimation of the band gap in oxides by DFT-GGA is well-known and attributed to self-interaction errors [29]. Using the HSE03-G_0W_0 method, a bulk band gap of 7.7 eV is obtained, in good agreement with the experimental value. We will therefore use the HSE03-G_0W_0 method to evaluate the effect of film thickness on MgO film band gap. The band structure in Figure 7.1 also illustrates that the conduction band edge consists mainly of Mg 3s orbitals, while the valence band edge consists of O 2p orbitals. Note that the conduction band shows a larger dispersion than the valence band, suggesting that the overlap between Mg 3s orbitals is larger.

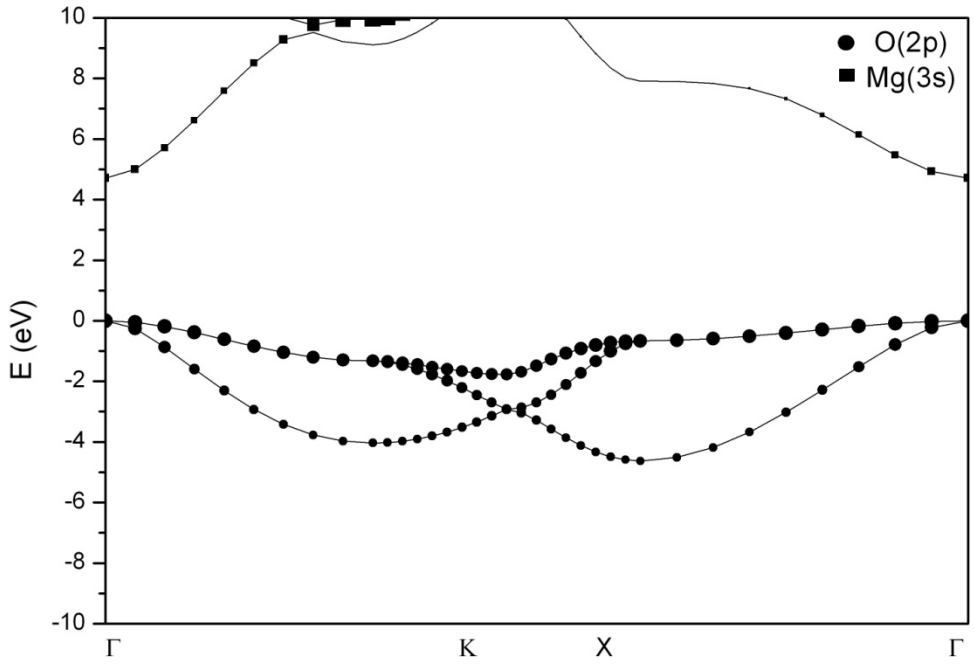

Figure 7.1: DFT-PBE band structure of bulk MgO. The nature of the bands is determined by projection on to the atomic orbitals. The figure illustrates that the conduction band is mainly derived from Mg(3s) orbitals while the valence band is derived from O(2p) orbitals

The effect of the thickness of the MgO(001) film on the band gap is shown in Figure 7.2. For a single-layer MgO film (1 ML), the HSE03-G_0W_0 band gap is 4.52 eV; 3.19 eV smaller than the bulk band gap. For comparison, the DFT-PBE band gap is also shown. DFT-PBE again underestimates the band gap, but the difference with the bulk band gap, 2.7 eV, is rather close to the HSE03-G_0W_0 difference. Adding a second layer of MgO increases the HSE03-G_0W_0 band gap by 0.69 eV. A similar increase, 0.44 eV, is predicted by DFT-PBE. Increasing the film thickness to 3, 4, and 5 layers increases the HSE03-G_0W_0 band gap by 0.32, 0.11, 0.05 eV, respectively. Increasing the film thickness beyond 5 layers has a limited effect on the calculated band gap, and the band gap of thicker MgO(001) films saturates around 5.7 eV. This value is lower than the bulk band gap and the smaller band gap can be attributed to lower Madelung potential at the surface, as explained later. The 1.2 eV increase in the band gap when the film thickness increases from 1 to 5 layers can be compared with the 1.1 eV increase in the tunneling barrier height measured by Klaua et al. [10] when the film thickness was increased from 2 to 6 ML.

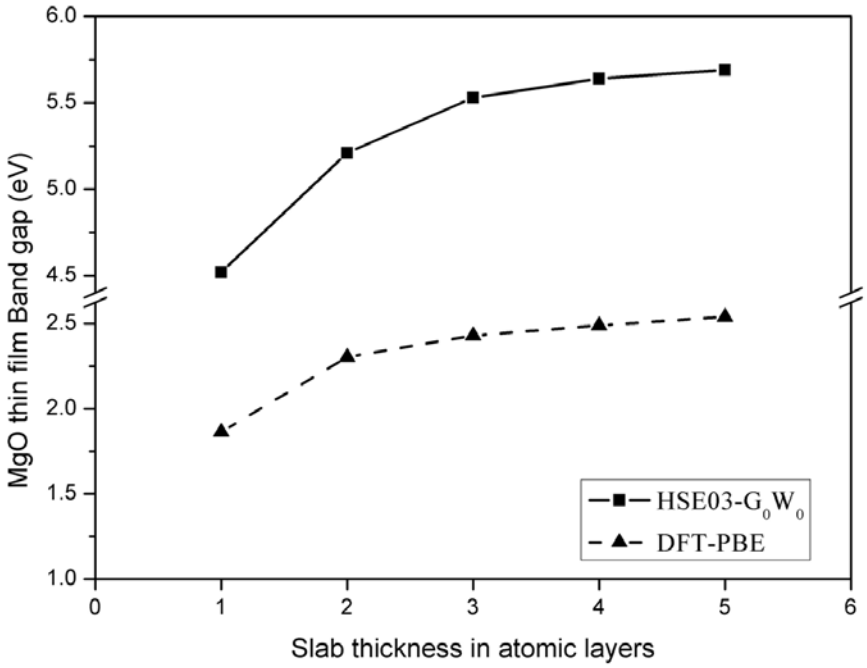

Figure 7.2: Thickness-dependent bandgap for MgO thin films. Both the DFT-PBE and the more accurate HSE03-G_0W_0 band gap are shown.

To understand the decrease of the band gap in ultrathin MgO(001) films, we first illustrate how the valence and conduction band are formed (Figure 7.3). To start the discussion, we consider the two-step band formation process in covalent semiconductor materials [33] (Figure 7.3(a)). First, the central atom coordinates covalently to its nearest neighbor in the unit cell. This splits the valence orbitals into bonding and the anti-bonding levels, according to the hybridization induced by the environment. When this structure is next placed in a periodic unit cell, the bonding levels form the valence band while the anti-bonding levels form the conduction band. The center of the valence and the conduction band is therefore related to the position of the bonding and the anti-bonding states, respectively. With increasing dimensionality, the bands broaden and hence the band gap decreases. For ionic materials such as MgO on the other hand, the valence and conduction band originate

from *different* atomic orbitals. This is illustrated in Figure 7.1 and 7.3b, where the valence band results from the O(2p) states and the conduction band from the Mg(3s) states. To construct the bands, we first consider the MgO unit. Charge transfer from Mg to O shifts the atomic levels compared to their atomic values. As Mg^{2+} becomes positively charged, the electrons bind more tightly and the energy level shift down, while the O^{2-} energy levels shift up due to increased electron-electron repulsion. Next, the MgO unit is placed in an array of point charges such that the electrostatic potential at the Mg and O positions is the similar to the potential in the MgO crystal. using point charges allows separating the influence from the potential and the effect of orbital overlap. The point charges create a Madelung potential that move the Mg(3s) level up and the O(2p) level down. Indeed, since the Mg^{2+} ions are surrounded by O^{2-} ions, the Madelung potential at the Mg^{2+} site is negative. Finally, orbital overlap with neighboring MgO units leads to the formation of the valence and conduction band. The center of the valence and the conduction band are therefore determined by the relative position of the Mg^{2+}(3s) and O^{2-}(2p) levels in the presence of a Madelung potential, and are affected by charge transfer.

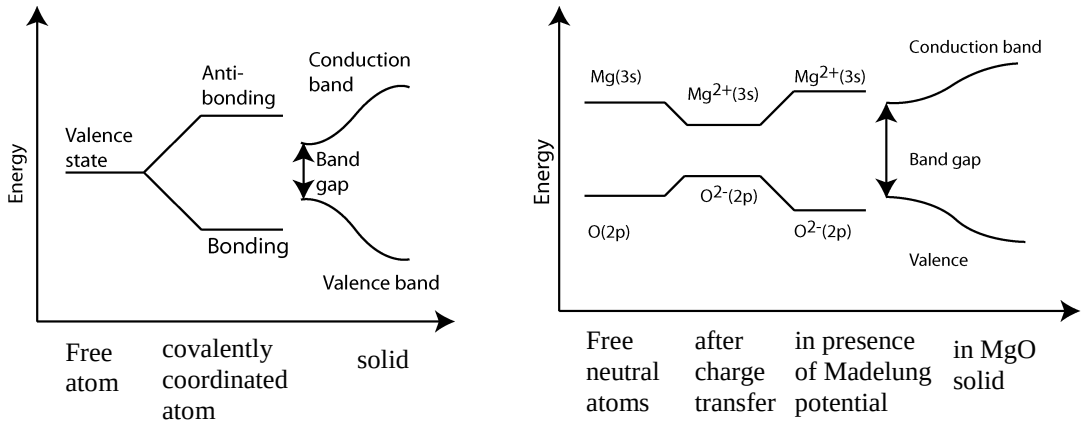

Figure 7.3: Diagram illustrating the origin of the band gap in covalent solids (a) and in ionic solids (b). In covalent solids, the location of bonding and anti-bonding orbitals determines the band gap. In ionic solids, the valence and conduction band result from different atomic orbitals and their relative position is determined by charge transfer and by the local Madelung potential.

To analyze the variation in the band gap with the film thickness, we calculated the local Madelung potential and the Bader charges on the different ions in the thin film (Figure 7.4). The shifts in the energy levels due to the Madelung potential and due to charge transfer are given by $Qe^2C_M/R(Mg-O)$ and by $Qe^2\langle 1/r\rangle$, respectively, where Q refers to the Bader charge on the atoms, e is the elementary charge, C_M is the Madelung constant, $R(Mg-O)$ the Mg-O bond distance, and $< r >$ the average radius of the orbital from (to) which the charge is removed (added) [34].

As shown in Figure 7.4(a). the Mg charge increases slightly from 1.737 to 1.744 e when the film thickness increases from one to two layers. The surface charges change little beyond two layers, but the change transfer in the subsurface layer is slightly larger than for the surface. For a 5-layer film, the charge transfer in the central layer, 1.748 e, has essentially converged to the bulk MgO value, 1.75 e As illustrated in Figure 7.3b, the increase in the charge transfer with the number of MgO layers decreases the band gap and the smaller charge transfer at the surface corresponds with a larger surface band gap. Using the above formula, the decrease in the band gap due to charge transfer can be estimated. The 0.0065 e increase in the charge transfer when going from one to two layers shifts the Mg level down by 0.07 eV and the O level up by 0.05 eV. Increased charge transfer hence decreases the band gap by 0.12 eV, to be compared to the increase found in the HSE03-G_0W_0 calculations, 0.69 eV.

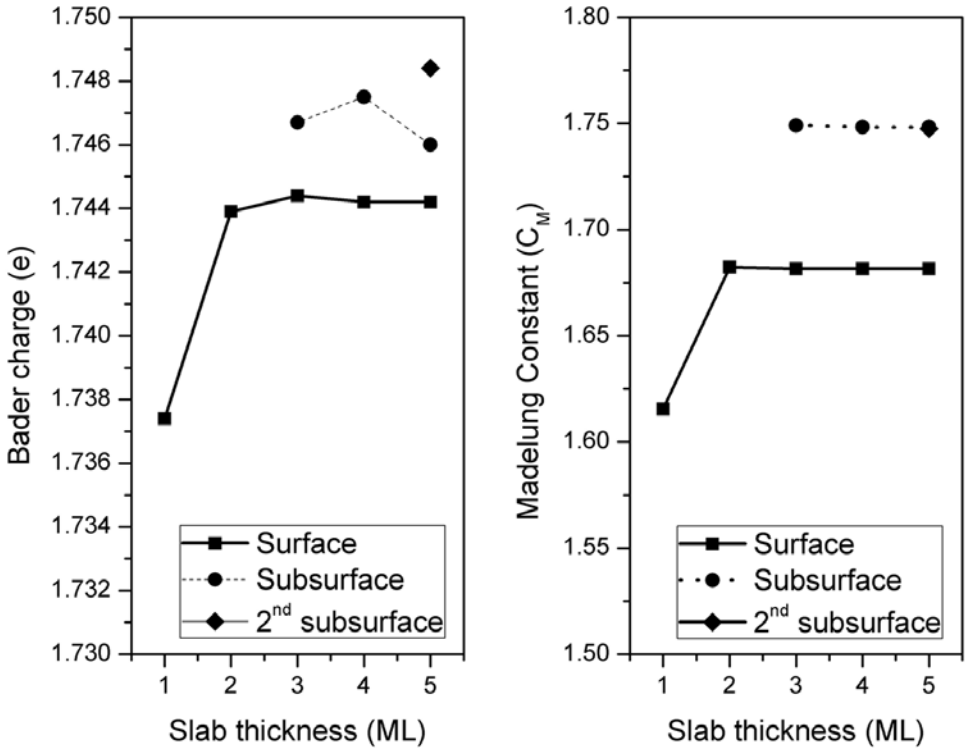

Figure 7.4: (a) Site-dependent Bader charges on Mg atoms as a function of the MgO film thickness. (b) Site-dependent Madelung constant (C_M) as a function of the MgO film thickness.

The second factor, the change in the local Madelung potentials with film thickness, (Figure 7.4b) has a much stronger influence on the band gap. The Madelung constant C_M was calculated by a direct summation, $C_M = \sum_j' \frac{(\pm)}{p_{ij}}$, where p_{ij} is an integer such that the inter-atomic distances r_{ij} are given by $r_{ij} = p_{ij} R$, with R the $Mg - O$ distance. Fast convergence was obtained using neutral cubic boxes in the summation [31].

The surface Madelung constant increases from 1.61 to 1.68 when the MgO film thickness increases from 1 to 2 layers, and then stays nearly constant. The Madelung constant for the central layer of a 3-layer slab, 1.74, essentially reaches the bulk value, 1.75. The Madelung constant hence converges rapidly and is determined by the

number of nearest neighbors. The 0.07 increase in the Madelung constant from one to two layers moves the Mg level up by 0.86 eV and the O level down by the same amount. The change in Madelung potential hence increases the MgO band gap by 1.72 eV and far outweighs the decrease in the band gap due to increased charge transfer. The change in the band gap obtained from this qualitative electrostatic model is larger than the actual increase. Indeed, a number of factors such as the broadening of the levels due to orbital overlap, the polarization of the wavefunction, and further charge redistribution are neglected in this qualitative model. The further increase in the band gap for 3 and 4 MgO layers therefore can be understood from the larger Madelung potential, $C_M = 1.75$, at subsurface sites. Indeed, the wavefunction is not localized on the MgO surface, but feels the effect of the higher Madelung potential (and hence the larger energy difference between the Mg^{2+} and O^{2-} energy levels) from the subsurface layers. Beyond 4 layers, this effect however becomes small and the calculated band gap converges. Finally, the smaller band gap for the thicker films, about 5.7 eV, as compared to the bulk band gap hence results from the lower Madelung potential at the surface, C_M=1.68. The 0.08 lower Madelung constant indeed translates to a 2.0 eV difference in the band gap. When the vacuum gap in the slab calculation is gradually reduced from 15Å, the band gap indeed gradually increases, following the increase in the Madelung constant.

7.4 Summary

The thickness-dependent band gap of MgO(001) thin films is calculated using the ab initio HSE03-G_0W_0 method. Different from covalent semiconductors where the band gap increases at the nanoscale due to quantum confinement, the band gap of oxide

thin films is significantly reduced at the nano-scale. For MgO, gradually increases with thickness from 4.5 eV for a monolayer of MgO to 5.7 eV for more than 5 layers. This increase matches the 1.1 eV change in the tunneling barrier measured by STS. A simple electrostatic model accounting for charge transfer and for changes in the local Madelung potential qualitatively describes the band gap variation and shows that the change in the Madelung potential is the dominant factor, and is hence general prototype of oxide thin films. The thickness dependent band gap of oxide films is expected to have an important effect as tunneling barriers and gate oxides approach this nanoscale.

References

[1] S. Ramanathan, *Thin Film Metal-Oxides Fundamentals and Applications in Electronics and Energy* (Springer, 2009).

[2] E. Y. Tsymbal, O. N. Mryasov, and P. R. LeClair, J. Phy.: Condens. Matter **15**, R109 (2003).

[3] J. S. Moodera and P. LeClair, Nat. Mater. **2**, 707 (2003).

[4] A. Ney, C. Pampuch, R. Koch, and K. H. Ploog, Nature **425**, 485 (2003).

[5] S. A. Wolf, D. D. Awschalom, R. A. Buhrman, J. M. Daughton, S. von Molnár, M. L. Roukes, A. Y. Chtchelkanova, and D. M. Treger, Science **294**, 1488 (2001).

[6] S. Yuasa, T. Nagahama, A. Fukushima, Y. Suzuki, and K. Ando, Nat. Mater. **3**, 868 (2004).

[7] S. S. P. Parkin, C. Kaiser, A. Panchula, P. M. Rice, B. Hughes, M. Samant, and S.-H. Yang, Nat. Mater. **3**, 862 (2004).

[8] W. Butler, X.-G. Zhang, T. Schulthess, and J. MacLaren, Phys. Rev. B **63**, 054416 (2001).

[9] J. Mathon and A. Umerski, Phys. Rev. B **63**, 220403 (2001).

[10] H. Yang, S.-H. Yang, D.-C. Qi, A. Rusydi, H. Kawai, M. Saeys, T. Leo, D. Smith, and S. Parkin, Phys. Rev. Lett. **106**, 167201 (2011).

[11] L. Yan, C. M. Lopez, R. P. Shrestha, E. A. Irene, A. A. Suvorova, and M. Saunders, Appl. Phys. Lett. **88**, 142901 (2006).

[12] A. Gibson, R. Haydock, and J. P. Lapemina, Phys. Rev. B **50**, 2582 (1994).

[13] M. Klaua, D. Ullmann, J. Barthel, W. Wulfhekel, J. Kirschner, R. Urban, T. Monchesky, A. Enders, J. Cochran, and B. Heinrich, Phys. Rev. B **64**, 134411 (2001).

[14] S. Schintke, S. Messerli, M. Pivetta, F. Patthey, L. Libioulle, M. Stengel, A. De Vita, and W.-D. Schneider, Phys. Rev. Lett. **87**, 276801-1 (2001).

[15] C. Noguera, Surf. Rev. Lett. **8**, 121 (2001).

[16] C. Freysoldt, P. Rinke, and M. Scheffler, Phys. Rev. Lett. **99**, 086101–1 (2007).

[17] K. Seino, J.-M. Wagner, and F. Bechstedt, Appl. Phys. Lett. **90**, 253109 (2007).

[18] M. Li and J. C. Li, Mater. Lett. **60**, 2526 (2006).

[19] F. Aryasetiawan and O. Gunnarsson, Rep. Prog. Phys. **61**, 237 (1998).

[20] W. Kohn and L. J. Sham, Phys. Rev. **140**, A1133 (1965).

[21] J. P. Perdew, K. Burke, and M. Ernzerhof, Phys. Rev. Lett. **77**, 3865 (1996).

[22] G. Kresse and J. Furthmüller, Comput. Mater. Sci. **6**, 15 (1996).

[23] G. Kresse and J. Furthmüller, Phys. Rev. B **54**, 11169 (1996).

[24] P. E. Blöchl, Phys. Rev. B **50**, 17953 (1994).

[25] U. Birkenheuer, J. C. Boettger, and N. Rösch, J. Chem. Phys. **100**, 6826 (1994).

[26] H. J. Monkhorst and J. D. Pack, Phys. Rev. B **13**, 5188 (1976).

[27] F. Fuchs, J. Furthmüller, F. Bechstedt, M. Shishkin, and G. Kresse, Phys. Rev. B **76**, 115109 (2007).

[28] R. F. W. Bader, *Atoms in Molecules: A Quantum Theory (International Series of Monographs on Chemistry)* (Oxford University Press, 1990).

[29] W. Tang, E. Sanville, and G. Henkelman, J. Phys.: Condens. Matter **21**, 084204 (2009).

[30] U. Schönberger and F. Aryasetiawan, Phys. Rev. B **52**, 8788 (1995).

[31] R. C. Whited, C. J. Flaten, and W. C. Walker, Solid State Commun. **13**, 1903 (1973).

[32] J. S. J. Hargreaves and S. D. Jackson, *Metal Oxide Catalysis, Volume 2* (Wiley-VCH, 2009).

[33] W. Harrison, Phys. Rev. B **8**, 4487 (1973).

[34] P. Bagus, G. Pacchioni, C. Sousa, T. Minerva and F. Parmigiani, Chem. Phys. Lett. **196**, 641 (1992).

[35] A. D. Baker and M. D. Baker, Am. J. Phys **78**, 102 (2010).

CHAPTER 8

Conclusion and outlook

8.1 Conclusion

This thesis aims at gaining a deeper insight into current flow at the nanoscale, which is vital to design nanoscale devices. Current flow at the nanoscale was studied for two systems: a Scanning Tunnelling Microscope (STM) junction which is an ideal test case due to its well-defined tunnelling junction structure, and a Magnetic Tunnel Junction (MTJ). For the calculation of current through the STM junction, the Elastic Scattering Quantum Chemistry (ESQC) method was used, while the Non-Equilibrium Green Function (NEGF) method was used to describe the MTJ. In both cases, the extended Hückel theory is employed to describe the system Hamiltonian. The theoretical calculations for the above systems led to a deeper insight into the current flow mechanism at the nanoscale.

For example, the study of the STM image of CO on a Cu(111) surface [1] shows that the reduction in the tunnelling current upon adsorption of CO on Cu(111) results from the strong interaction of the CO 5σ highest occupied molecular orbital with the Cu(111) surface state, dominated by Cu $4p_z$ orbitals. Such over-coupling reduces the surface density of states near the Fermi level and decreases the tunnelling current at the sites where CO is adsorbed. The strong coupling is facilitated by the spatial extent, the symmetry and the energy of the surface state of the Cu(111) surface.

A combination of STM image calculations and thermodynamic stability calculations was used to investigate the surface structure obtained during the experimental thermal stability study of the MoS_2 surface, which can be used as a platform for constructing surface dangling bond wires [2]. The simulation shows that the MoS_2 surface transforms to a S-rich Mo_2S_3 surface above 1300 K [3]. The calculations also confirm that the bright spots in the experimental STM image of the reconstructed surface originate from surface S atoms. The proximity of the S atoms to the STM tip outweighs the higher density of states of underlying Mo resulting in the bright appearance of S atoms. This behaviour is in sharp contrast with CO on Cu(111), where CO molecules appear as a dark depressions despite being closer to the STM tip. An STM image hence is not a simple topological image of the surface, or of the electron density at the Fermi level.

The study of the Fe|MgO|Fe MTJ shows that the application of *xz* biaxial strain increases the conductance and decreases the TMR ratio [4], elucidating the experimental findings in the laboratory of our collaborator. The increase in the conductance occurs because the MgO bandgap decreases by about 0.3 eV and because the barrier thickness decreases by 5%. The conductance for the anti-parallel configuration is significantly more sensitive to *xz* strain, which is due to the movement of the Fe(100) minority states at the Femi level towards the centre of the Brillouin zone where the decay rate inside MgO barrier is smaller. This drastically increases minority to majority transmission for the anti-parallel alignment, and results in a decrease of the TMR ratio with the application of biaxial xz-strain.

Finally, the variation of band gap of MgO(001) thin films observed during barrier-thickness-dependent tunneling current measurements is investigated in more detail because of the industrial importance of Fe|MgO|Fe MTJs. Our DFT calculations reveal that the MgO(001) band gap decreases with thickness below 5 ML, consistent with experimental observations [5]. The decrease in band gap with decreasing film thickness arises from a decrease in the Madelung potential. This is somewhat compensated by a decrease in the charge transfer from the Mg to O ions, which slightly increases the band gap. A simple electrostatic model, which accounts for both charge transfer and changes in the local Madelung potential, is able to reproduce the trend observed in the DFT calculation.

In conclusion, the nanoscale tunneling current calculations provided valuable insights into the various transport mechanisms. Understanding the electronic origin of current flow through different systems, as illustrated in this work, would be very useful to begin to design atomic-scale devices.

8.2 Outlook

The relentless downscaling of electronic devices will soon result in their sizes reaching atomic scales where quantum mechanical effects need to be included to understand their design. In fact, recent work by Simmons and co-workers [6] has laid the groundwork for such futuristic nanoscale quantum computers. They fabricated a transistor atom by atom using a combination of STM and hydrogen-resist lithography, Figure 8.1. Their transistor consists of a single phosphorus atom positioned between source and the drain contacts and two gate electrodes all made up of phosphorous atoms on a silicon wafer. Similar to traditional transistors, the gate voltage is used to control the current flow between the source and the drain.

These nanoscale transistors would be orders of magnitude smaller and faster than the present-day silicon-based transistors.

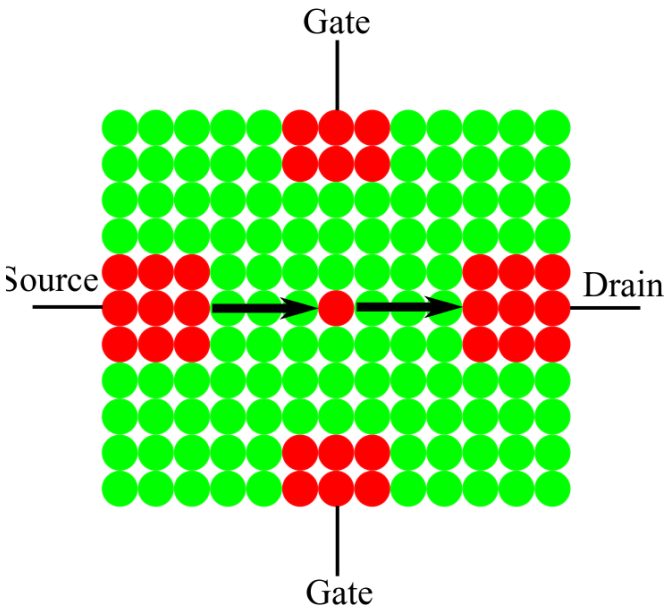

Figure 8.1: Schematic of the single-atom transistor fabricated by Simmons and co-workers [1]. A single phosphorus atom (red sphere) is placed with atomic precision on the surface of a silicon crystal (green spheres) between the metallic source and drain electrodes, which are formed by phosphorus wires that are multiple atoms wide. Electric charge flows (thick black arrows) from the source to the drain through the phosphorus atom when an appropriate voltage is applied across the gate electrodes. This schematic is not to scale: there are several tens of rows of silicon atoms between the phosphorus atom and the source and drain electrodes, and more than 100 rows of silicon atoms between the phosphorus atom and the gate electrodes.

8.3 Future Work

8.3.1 Simulation of atomic-scale logic gates

In this thesis, we studied the IV characteristics of CO adsorbed on a Cu(111) surface. Our simulations provided deeper insight into the electronic origin of the reduction in the tunnelling current when CO is placed between the Cu(111) surface and the tip. In particular, the role played

by the CO frontier molecular orbitals and their interaction with the substrate electronic states was elucidated.

Building on that work, the IV characteristics of an array of atoms and molecules arranged with atomic precision on a surface could be studied. Preliminary studies have shown that such atomic scale structures show potential as nano-scale logic gates. For example, a study by Ample et al. [7] showed that a three-terminal logic OR gate can be constructed using a single molecule or using with a surface circuit fabricated from surface dangling bonds created by H desorption from a Si(100)H surface. A more systematic study of how the electronic structure of the substrate atoms, of adsorbed atom or molecule frontier orbitals, their arrangements, and their adsorption site influence the IV characteristic of the nano-system.

As shown in our study, the IV characteristics of even a single CO molecule on a Cu(111) substrate do not follow intuition. It is therefore important to perform detailed simulations to evaluate the function of atomic-scale devices, before fabrication and testing of the device.

8.3.2. Effect of strain on the behaviour of MTJs

In a second part of this thesis, we studied the effect of biaxial strain on performance of a technologically important MTJ. Can we use strain engineering to improve the performance of these devices? Our study showed the application of *xz* biaxial strain increases the tunnelling current (a desired effect) because of the decreased barrier height and barrier thickness.

Unfortunately, *xz* strain also reduces the TMR ratio (a undesired effect) because minority states move closer to the centre of the Brillouin zone, which increases their conductivity faster than the conductivity of the majority electrons. However, other types of strain can be envisioned, which would increase both the tunnelling current and the TMR ratio. For example, the effect of the axial, transverse, longitudinal and transverse strain on the conductance should be studied.

This study can be further expanded and include different combinations of electrode and barrier materials, opening a field of MTJ strain engineering. In such a study we would first investigate the effect of strain on the electronic states of the electrode and the on the electronic properties of the barrier material. This knowledge could be subsequently combined to arrive at combinations that increase both the TMR ratio and the tunnelling current.

The scope of such a study can be further extended by the examining effect of the strain source. Indeed, strain might originate from mechanical, magnetic, and electrical sources. Since strain introduced by magnetic fields only operates on magnetorestrictive materials could be exploited to evaluate what happens when strain is applied only to the electrode material. The effect of strain introduced by electric fields also needs closer examination, e.g., when ferroelectric materials are used as a barrier material. Indeed, it has been shown that, under an applied voltage, the piezoelectricity of a ferroelectric barrier produces a strain that changes the tunnelling transport characteristics of the barrier [9].

References

[1] R. K. Tiwari, D. M. Otálvaro, C. Joachim, and M. Saeys, *Surf. Sci.* **603**, 3286 (2009).

[2] K. Yong, D. Otalvaro, I. Duchemin, M. Saeys, and C. Joachim, *Phys. Rev. B* **77**, 205429 (2008).

[3] R. K. Tiwari, J. Yang, M. Saeys, and C. Joachim, *Surf. Sci.* **602**, 2628 (2008).

[4] A. M. Sahadevan, R. K. Tiwari, G. Kalon, C. S. Bhatia, M. Saeys, and H. Yang, *Appl. Phys. Lett.* **101**, 042407 (2012).

[5] M. Klaua, D. Ullmann, J. Barthel, W. Wulfhekel, J. Kirschner, R. Urban, T. Monchesky, A. Enders, J. Cochran, and B. Heinrich, *Phys. Rev. B* **64**, 134411 (2001).

[6] M. Fuechsle, J. A. Miwa, S. Mahapatra, H. Ryu, S. Lee, O. Warschkow, L. C. L. Hollenberg, G. Klimeck, and M. Y. Simmons, *Nat. Nanotechnol.* **7**, 242 (2012).

[8] F. Ample, I. Duchemin, M. Hliwa and C. Joachim, *J. Phys.: Condens. Matter* **23** 125303 (2011)

[9] H. Kohlstedt, N. A. Pertsev, J. Rodríguez Contreras, and R. Waser *Phys. Rev. B* **72**, 125341 (2005).